Author:
Taylor, Victoria C A

Title:
Ultrafast Spectroscopy of Photoactive Nanomaterials

Ultrafast Spectroscopy of Photoactive Nanomaterials

Victoria Carmen Artemesia Taylor

A dissertation submitted to the University of Bristol in accordance with the requirements for award of the degree of

Doctor of Philosophy

in the School of Chemistry, Faculty of Science

May 2020

Word count ~33,000

Abstract

Time-resolved spectroscopy is a versatile tool to investigate ultrafast dynamics. The photoinduced dynamics of photoactive nanomaterials occur over a range of timescales and can be initiated by femtosecond processes. Understanding these dynamics is paramount to inform rational design of new materials. In this thesis I detail ultrafast spectroscopic measurements of several photoactive nanomaterials.

Ultrafast transient absorption (TA) was used to investigate the dynamics of localised surface plasmon polaritons on hollow gold nanoshells (HGNs) coupled with excitons in J-aggregates. I determined for the first time, a power dependence to the phonon breathing mode period of HGNs, and investigated the transient response of a novel sample of HGNs, with J-aggregates inside as well as on the outer surface, with TA. Through my pump dependent TA measurements, I was able to isolate the transient signatures associated with J-aggregate HGN hybrid system and I propose that the picosecond response is primarily due to hot electrons rather than plexcitons as has been reported for similar systems.

I used two-dimensional infrared spectroscopy to directly measure 470 ± 50 fs and 2.8 ± 0.5 ps time constants associated with the reorientation of formamidinium cations in formamidinium lead iodide perovskite thin films. Molecular dynamics simulations facilitated association of these time constants with the cation agitating about an equilibrium position, with NH_2 groups pointing at opposite faces of the inorganic lattice cube, and the cation undergoing 90° flips, respectively. These timescales preclude the existence of stable (anti)ferroelectric domains in formamidinium lead iodide perovskite films which had been theorised to be the source of the unusually high power conversion efficiencies observed in this material. In addition, time-resolved infrared measurements revealed a prominent vibrational transient feature arising from a vibrational Stark shift.

In the final results chapter of my thesis, I describe the ultrafast transient absorption microscopy experiment that I constructed, discuss functionality tests on the apparatus, and consider the associated design principles.

Acknowledgements

I have many people to thank for teaching and supporting me throughout my PhD and for making the last few years in Bristol such an enjoyable and rewarding experience.

First and foremost, I would like to thank my supervisor, Dr Tom Oliver, for his steadfast support, continued patience (particularly with unicorn questions), and for providing enthusiasm for science whenever mine was running short. Your tireless efforts to provide the best opportunities for your students are greatly appreciated. No doubt I am the first of many Oliver group students to write-up, but I do hope in future, Tom, you will not have to deal with providing feedback on PhD theses while convalescing from a global-pandemic causing virus.

Thanks to the Oliver group and the wider laser group (members past and present, too many to list here) for comradery, tea breaks, and the all-important Friday pub trip. Especially thank you to those of you who have been through the highs and lows of a PhD with me. Your friendship has been a mainstay of my PhD.

I am also grateful for all the advice and support provided by my secondary supervisor, Henkjan Gersen and the nano-optics group. Thanks are also sent to my BCFN colleagues and friends for helping get my time in Bristol off to a good start and for continued support since then, particularly to Dr Annela Seddon.

I would like to thank my collaborators (Dr Sara Núñez Sánchez, Dr Devendra Tiwari, Dr Tracey Clarke, and many scientists at RAL) for enabling the science in this thesis.

Thank you to the many staff in the school of chemistry and the university who have provided services that I have relied on, including staff working in the mechanical workshop, electronics workshop, and stores, as well as the cleaners and maintenance people.

Thanks to my friends from Bristol and further afar for supporting me throughout my PhD, but especially during this writing up period, when they have stuck by me even when that meant putting up with radio silence (particular thanks to Nome for this). A special and sincere thanks is given to my friends in Bristol, particularly former and current housemates, for making the last few years such fun; Extra thanks to Dani for being queen of fun and for trading cups of tea for better pasta than I could ever hope to cook.

I'd like to thank my family. Thanks to my older sister, Amybel, and younger brother, Leonard, for being my life-long best friends and amazing people who I can always rely on. Finally, I'd like to express my distinct gratitude to my parents for unwavering support, dedication, and love. You are the best teachers I've ever had.

Author's Declaration

I declare that the work in this dissertation was carried out in accordance with the requirements of the University's *Regulations and Code of Practice for Research Degree Programmes* and that it has not been submitted for any other academic award. Except where indicated by specific reference in the text, the work is the candidate's own work. Work done in collaboration with, or with the assistance of, others, is indicated as such. Any views expressed in the dissertation are those of the author.

SIGNED: ..... DATE:.....

Table of Contents

Chapter 1. Introduction

1.1. Introduction

Over the past few decades the development of new analysis and fabrication tools has allowed thousands of nanomaterials to be developed and studied. Subsequently the field of nanoscience has flourished. As a vague term, requiring only relevance to an entire length-scale, nanoscience spans multiple disciplines and encompasses many research topics. Definitions of 'nanomaterial' vary,[1,2] but for the purposes of my thesis it will be used as a generic term to encompasses any condensed-phase sample that has components or structure with dimensions greater than 1 nm and less than 1 μm.

The nanoscale bridges the divide between large molecules and extensive complex structures. Therefore, materials as varied as carbon nanotubes, DNA, proteins, mitochondria, Photosystem II, thin films, graphene, nanostructured conductive polymers, and even semiconductors etched with nanoscale designs can all be classified as nanomaterials. At this intersection between individual molecules and material structures a plethora of interesting and functional phenomena can occur. Forces that may be negligible at the macroscale can be powerful at the nanoscale, producing effects such as changes in melting point[3] and greater chemical reactivity,[4] or entirely new phenomena can manifest such as quantum confinement[5] and quantum tunnelling effects. [6] The many advantages and intrigues of the nanoscale are certainly too numerous to review here, however, there are many useful textbooks that give overviews of these diverse range of effects. [7-9] Thanks to these phenomena the potential applications of nanomaterials are as diverse as medicine, [10] computing, [11] materials engineering and catalysis, [12] to name but a few.[5] In order to harness the full potential of this rich length-scale it is vital to understand the interactions and dynamics that govern the properties of these materials.

My thesis focuses on the use of ultrafast time-resolved spectroscopy to study a selection of photoactive nanomaterial samples and explore the events that occur on femtosecond to nanosecond timescales which often determine the functionality of these materials. Many types of ultrafast time-resolved spectroscopy techniques exist; but all are based around the principle of photo-initiation of a process with a pump pulse of light, which defines a 'time zero', and then examing the system at a later time with a probe pulse. By varying the time delay between the pump and probe pulses, the dynamics of the sample following excitation can be monitored. Different time-resolved spectroscopy techniques

can monitor dynamics over a multitude of timescales and probe electronic and/or nuclear degrees of freedom. The term 'ultrafast' specifically refers to techniques that have femtosecond resolution and thus facilitate monitoring dynamics that occur on femtosecond or longer timescales.

Excitation of photoactive materials can be used to drive the system out of equilibrium and initiate functionality, for example, charge generation in photovoltaics materials, [13] photochemical reactions, [14] or the photochemical processes that occur in plant photosystems during photosynthesis. [15] The ensuing dynamics return the system to an equilibrium, which may or may not be the same as the initial state of the system, *e.g.* photoproduct *vs.* original ground state molecules. These dynamics can occur over a multitude of timescales. For instance, following excitation of a photovoltaic material, charges or charge carriers can survive for microseconds and undergo a myriad of dynamic processes in the intervening period, such as cooling, scattering, localisation, charge migration, or recombination.[16] The timescale of each of these processes, and most importantly which processes occur, can all be dictated by the excitation conditions and the material properties. Therefore, understanding these processes, and the interactions that dictate them, can inform material design. For example, understanding what limits charge transfer efficiency in pertinent organic materials, has important implications in photovoltaic materials design.[17]

Ultrafast spectroscopy is an effective tool to study ultrafast photoactive material dynamics, and nanomaterials offer a compelling new range of materials that hold much potential. In this thesis I will describe three ultrafast studies of nanomaterial samples. However, before discussing these experiments, in the rest of this chapter I will discuss some of the fundamental aspects of time-resolved spectroscopies and the practical aspects of implementing them.

1.2. Fundamentals of Ultrafast Time-resolved Spectroscopy

1.2.1. Light-matter interactions

Under the classical dipole oscillator model, light-matter interactions can be modelled by treating materials as a collection of electronic dipoles, be that dipoles from an electron orbiting a nucleus, or a dipole from a molecular bond.[18] As dictated by simple harmonic motion, the dipoles will exhibit specific resonant frequencies (ω_0) determined by the

strength (or spring constant) of the dipole (K) and its reduced mass (μ) as defined in equation 1.1:

$$\omega_0 = \sqrt{\frac{K}{\mu}} \tag{1.1}$$

These dipoles can interact with the oscillating electromagnetic field of light incident upon the material. The time-dependent oscillating electric field ($\varepsilon(t)$) of a monochromatic, continuous light wave with angular frequency ω_γ can be given as a function of time (t) by:

$$\begin{aligned} \varepsilon(t) &= A\cos\left(\omega_\gamma t + \phi\right) \\ &= \Re\left\{A\, e^{-i(\omega_\gamma t + \phi)}\right\} \end{aligned} \tag{1.2}$$

Where ϕ is the phase of the wave, A is the amplitude, and $\Re$ indicates the real component of the equation. For simplicity only the electric field of the electromagnetic wave will be considered in the following discussion. If the frequency of the incident electric field matches the resonant frequency of the dipole ($\omega_\gamma = \omega_0$), the light will induce large amplitude oscillations in the dipole at this frequency. The oscillating dipole can be considered to emit an electric field 180° out of phase with the incident field such that they destructively interfere. This results in the energy of the incident field being transferred to the dipole and the incident field is destroyed, in other words, the light is absorbed by the material. In the instance that the frequency of the incident field is not resonant with the dipole, the dipoles will only briefly undergo small amplitude forced oscillations and can be considered to instantaneously re-emit the electric field energy, such that it is transmitted through the material.

Excited, oscillating dipoles can also undergo the reverse process to absorption such that the matter loses energy by emitting light at the resonance frequency. This emission process can either occur without external stimulus, in which case it is called spontaneous emission, or it can be triggered by incident light at the resonance frequency, in which case it is called stimulated emission and the emitted light will be colinear to and coherent with the incident light. These three processes; absorption, stimulated emission, and spontaneous emission, dictate the rates of absorption and emission for a simple two-level system, as denoted by the Einstein coefficients of a material.

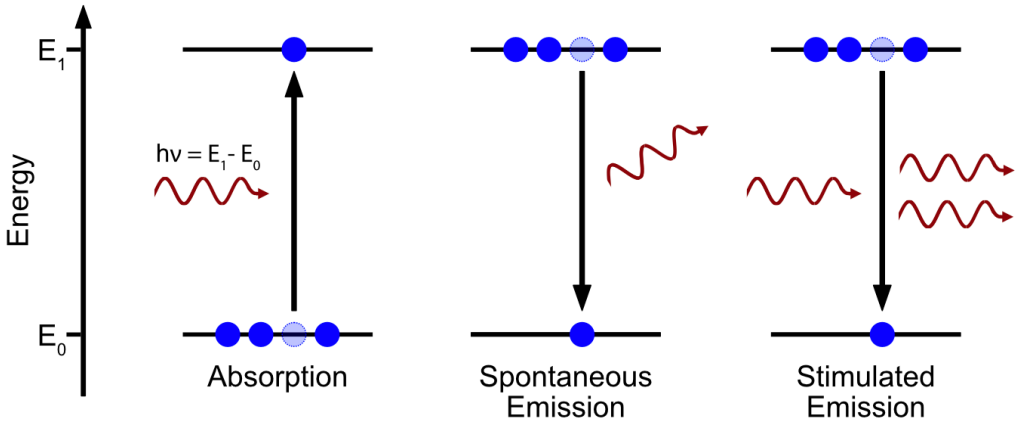

Figure 1.1: Schematic energy level diagram illustrating absorption, spontaneous emission and stimulated emission for a model two-level system with ground state E_0 and excited state E_1.

Alternatively, from a quantum mechanical perspective, the resonance frequencies of a dipole correspond to discrete energy states that can be occupied, the energies of these states are referred to as the energy levels of the system. The absorption of an incident photon imparts energy to the system such that the system is excited to a higher energy state if, and only if, the energy of the photon is exactly equal to the difference in energy between the initial and final states (see Figure 1.1). This concept can be extended and generalised for a system consisting of multiple dipoles with different energy levels (or frequencies), such as a molecule.

In quantum mechanics the state of a system is described by its wavefunction, Ψ, which is frequently expressed as a function of the constituent particles' positions ($\boldsymbol{r}$) and time (t), $\Psi(\boldsymbol{r}, t)$, although other basis sets (or coordinate systems) are equally valid. The time independent Schrodinger equation states that at the total energy of the system (E, as extracted with the Hamiltonian operator, $\hat{\mathrm{H}}$) is equal to the sum of the kinetic and potential energy of the system (operators $\hat{\mathrm{T}}$ and $\hat{\mathrm{V}}$, respectively):

$$\hat{\mathrm{H}}\Psi(\boldsymbol{r}) = \hat{\mathrm{T}}\Psi(\boldsymbol{r}) + \hat{\mathrm{V}}\Psi(\boldsymbol{r}) = \mathrm{E}\Psi(\boldsymbol{r}) \tag{1.3}$$

For a molecular system, consisting of electrons and nuclei this can be expanded into contributions from the kinetic energy of the electrons and nuclei (denoted by subscripts e and N respectively) and the Coulombic potential of the whole system is given as:

$$\hat{\mathrm{H}}\Psi(\boldsymbol{r}_e, \boldsymbol{R}) = [\hat{\mathrm{T}}_e + \hat{\mathrm{T}}_N + \hat{\mathrm{V}}]\Psi(\boldsymbol{r}_e, \boldsymbol{R}) \tag{1.4}$$

Where $\boldsymbol{R}$ denotes the nuclear co-ordinates and $\boldsymbol{r}_e$ is the equivalent for the electrons. Generally, this cannot be solved explicitly for anything other than hydrogen or hydrogen-like 1 electron atoms or molecules. Fortunately, the problem can be simplified greatly by use of the Born-Oppenheimer (BO) approximation. [19]

The BO approximation (also known as the adiabatic approximation) uses the disparity in mass between electrons and nuclei (an electron has ~1/1836 the mass of a proton) to reason that electrons move orders of magnitude faster than nuclei, and so are much quicker to react to changes in the electrostatic potential of their environment. This approximation permits the separation of the electrons and nuclei motion, creating two separate systems, with wavefunctions Ψ_e and Ψ_N:

$$\Psi = \Psi_e \Psi_N \tag{1.5}$$

The BO approximation treats electrons as if they respond instantaneously to any change in nuclear arrangement. This, therefore, allows one to express the electron distribution as a function of nuclear coordinates (treating the nuclei as stationary), such that the Hamiltonian for the electronic component reduces to:

$$\hat{\mathrm{H}}_e \Psi_e(\boldsymbol{r}, \boldsymbol{R}) = [\hat{\mathrm{T}}_e + \hat{\mathrm{V}}]\Psi_e(\boldsymbol{r}, \boldsymbol{R}) \tag{1.6}$$

This equation can be solved to find the electronic distribution as a function of nuclear position:

$$\hat{\mathrm{H}}_e \Psi_{e,i}(\boldsymbol{r}, \boldsymbol{R}) = U_i(\boldsymbol{R})\Psi_{e,i}(\boldsymbol{r}, \boldsymbol{R}) \tag{1.7}$$

The subscript i is introduced to denote different electronic states with corresponding eigenvalues, U_i. Repeatedly solving the electronic wavefunction for varying nuclear arrangements creates what is referred to as a potential energy surface (PES), where the nuclear degrees of freedom make up the axis of the PES (or space) such that each position on the surface has a corresponding nuclear arrangement and a calculated electron distribution, with energy $U_i(\boldsymbol{R})$. Under the BO approximation, the exact positions of the electrons do not influence nuclear motion since the nuclei are too slow to respond. Instead the nuclei respond to the time-averaged influence of the electrons (the mean electron field). Therefore, the PES is sufficient to model the electrostatic potential exerted on the nuclei. The Hamiltonian for the nuclear wavefunction becomes:

$$\hat{\mathrm{H}}\Psi_{N,i}(\boldsymbol{R}) = [\hat{\mathrm{T}}_N(\boldsymbol{R}) + U_i(\boldsymbol{R})]\Psi_{N,i}(\boldsymbol{R}) \tag{1.8}$$

With solution:

$$\hat{\mathrm{H}}_N\Psi_{N,i,j}(\boldsymbol{R}) = E_{i,j}(\boldsymbol{R})\Psi_{N,i,j}(\boldsymbol{R}) \tag{1.9}$$

Where the subscript j is used to denote different nuclear (or vibrational) states, which have eigenvalues $E_{i,j}(\boldsymbol{R})$. Such that each ith electronic state, or PES, has a corresponding set of vibrational energy levels, j (see Figure 1.2). This combination of vibrational (j index) and electronic (i index) information leads to the term 'vibronic' states (vibrational and electronic) to describe the overall state of the system. Although the BO approximation has been widely used to successfully model the energy states of molecules, it is important to note that it breaks down under situations where there are large non-adiabatic effects, such as if two PESs come into close proximity- parts of the PES known as conical intersections.

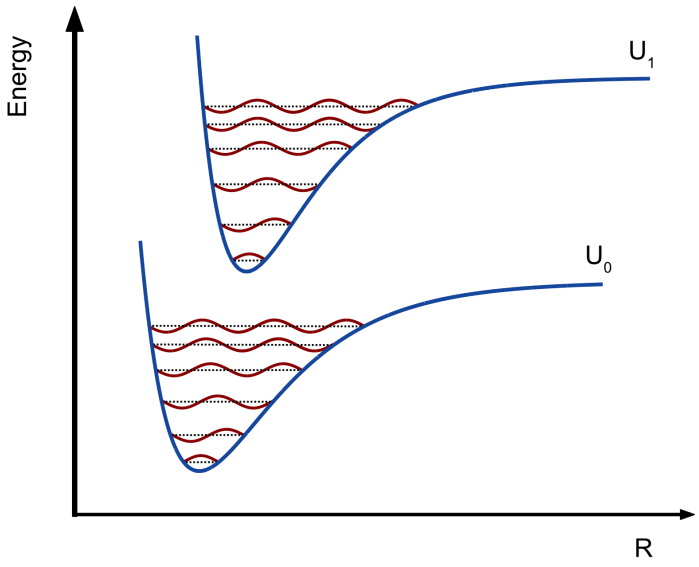

Figure 1.2: Potential energy surfaces (blue lines) and corresponding vibrational eigenstates (red lines) plotted along a nuclear degree of freedom

Thus far only radiative transitions in a two-level system have been discussed, which presents an extremely simplified model compared to the optical responses observed in most molecular systems. The introduction of vibrionic states adds further complexity to molecular absorption and emission spectra (compared to the schematic in Figure 1.1) even with just two electronic states, as there are multiple possible transitions. The Franck-Condon principle (a consequence of the BO approximation) states that only vertical

transitions can occur, and the probability is proportional to the square of the vibrational overlap integral.[19] This can lead to closely spaced peaks in the corresponding absorption spectrum. Moreover, unlike in the simple two-level system without vibrational states, the absorption and emission frequencies can differ. A molecule can return to the initial electronic state but retain quanta of vibrational excitation, or it could undergo vibrational energy relaxation before emission, both resulting in an observed red-shifted emission. Vibrational energy relaxation is a process in which the molecule transitions to a lower vibrational energy level (on the same PES so the electronic state does not change) by transferring energy to multiple coupled modes elsewhere in the molecule (*e.g.* the total energy of the molecule is maintained) or to the surrounding bath where the energy is lost from the molecule. The latter mechanism is only active in the condensed phase.

Of course, typically a molecule will have many electronic states and so there may be multiple decay pathways. Often a distinction is made between radiative and non-radiative decay according to whether the process involves emission of a photon. Repopulation of the ground state, or reaching a new equilibrium, can involve a combination of both radiative and non-radiative processes. [19]

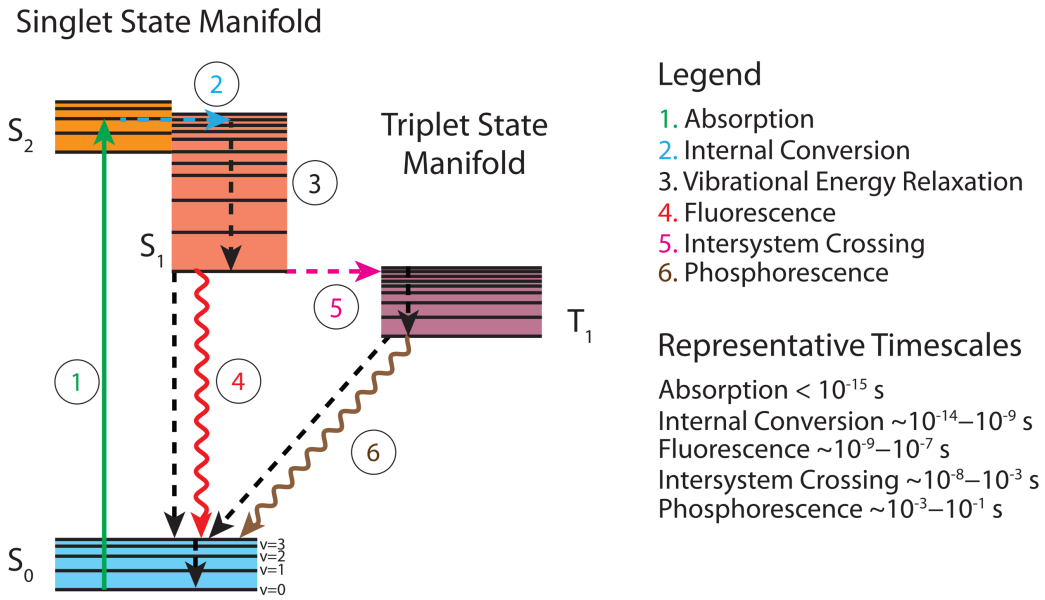

Figure 1.3: Jablonski diagram for a molecule in solution and representative timescales for labelled processes.

Jablonski diagrams are one way to represent the competing decay pathways for molecular systems, and an example is given in Figure 1.3. Note that unlike PESs, there is no meaningful horizontal axis on a Jablonski diagram, and it bears no relation to molecular coordinates or degrees of freedom. As indicated in Figure 1.3, the typical timescales upon

which different processes occur vary by many orders of magnitude and are directly related to the probability of each pathway. Conventionally singlet states (all electrons are in pairs with opposing spins, such that the spin quantum number, S, is 0) are denoted S_n, where the subscript refers to the energetic ordering of the states, and so S_0 corresponds to the electronic ground state (all occupied orbitals contain a pair of antiparallel spin electrons). In excited singlet states one of the electrons from the highest occupied molecular orbital is promoted to a higher energy molecular orbital, but the electron spins remain antiparallel. Triplet states correspond to electronic configurations where two of the orbitals, each contain one electron with parallel spin states, so S=1. Transitions between singlet and triplet (T_n) states are formally forbidden due to the spin selection rule. However, these transitions can occur through coupling of spin and orbital angular momentum, and thus accounts for the slower timescales typically associated with intersystem crossing and phosphorescence. In Figure 1.3, processes 4 and 5, fluorescence and intersystem crossing, are examples of competing pathways because they both provide a way for the molecule to return back to S_0.

In contrast to the molecular Jablonski diagram picture, the electronic energy levels of inorganic semiconducting solids are typically described in terms of energy bands and the density of states. Notionally, energy bands can be interpreted as such densely spaced energy levels that individual states become indistinguishable. This occurs due to the dense spacing of atoms within a lattice; the atomic orbitals of adjacent atoms 'overlap' and so interact very strongly. This broadens the discrete energy levels into a continuous range of energies that are delocalised though the lattice. Consequently, the density of states must be introduced to expresses the number of states available within a given energy range.

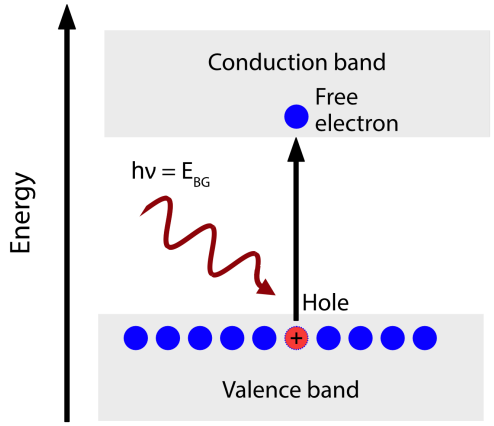

Figure 1.4: Schematic illustrating the conduction and valence bands of a semiconductor, and free electron and hole carrier generation upon absorption of light.

In semiconductors there are two key energy bands called the valence band and the conduction band, as illustrated in Figure 1.4. For a semiconductor, the valence band states are lower in energy and filled (occupied) with electrons at 0 Kelvin, whereas the conduction band states are higher in energy and are unoccupied. The difference in energy between the maximum energy of the valence band and the minimum energy of the conduction band is called the band gap. Under appropriate conditions, a photon with energy equal to or greater than the band gap energy can excite an electron from the valence band into the conduction band. The resulting absence of an electron in the valence band is referred to as a hole, which is a positively charged quasi-particle. Both valence band holes and conduction band electrons can move semi-freely within the material and therefore conduct charge. The motion of free electrons and holes is determined by the band structure of the material in $\underline{k}$ (or wave vector) space, which is not discussed here but is routinely covered in solid-state physics textbooks. If the electron is excited to an energy above the minimum of the conduction band it is called a hot charge carrier because it can lose energy (through scattering for example) and 'cool' to the conduction band edge (analogous to vibrational cooling in molecular systems). Free electrons and holes can recombine and emit a photon if they meet in the material.

Some semiconductors have exciton states in the bandgap just below the conduction band of the material. Excitons form if, as the electron/hole pair are created, they maintain coulombic attraction but enter a stable orbit. Excitons are generally categorised into two types: Wannier-Mott excitons, are weakly bound (~10s meV) so have a large diameter, can diffuse freely through materials, and tend to form in semiconductors. The second variety are Frenkel excitons, which are tightly bound (~0.8-1 eV) so have a small radius, are localised to molecules or a number of molecules, can migrate through electronic energy transfer, and they tend to form in insulators and molecular crystals.

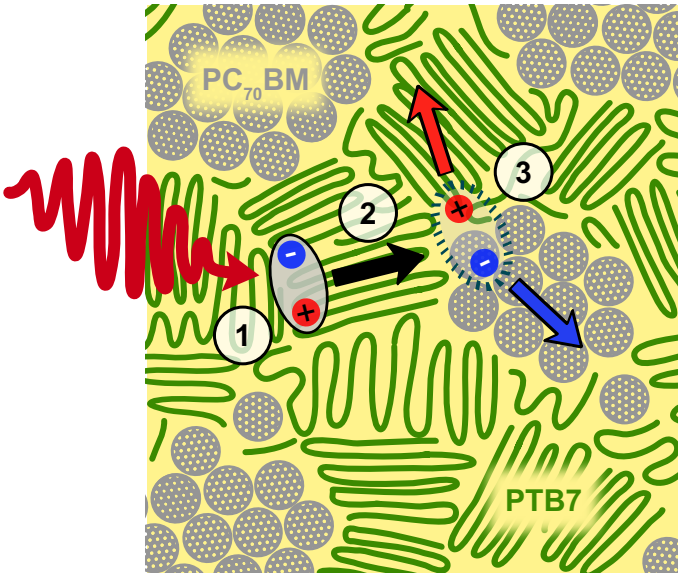

Figure 1.5: Schematic to illustrate the three key processes involved in charge generation in bulk heterojunction thin films (see text for details).

Generation of free charge carriers through absorption of light is the fundamental process required to generate a voltage in photovoltaic semiconducting materials. [20] This is schematically illustrated in Figure 1.5 for a bulk-heterojunction of PTB7 (electron donor) and $PC_{70}BM$ fullerene (electron acceptor). Photoexcitation of the sample generates Frenkel excitons in the semiconducting polymer (indicated by green lines) domain (process 1), which can migrate (process 2) to an interface with the $PC_{60}BM$ (grey shapes). Here charge transfer (process 3) can occur to generate electrons and holes, which then migrate through the thin film via respective acceptor and donor domains. There is extensive ongoing research into the development of new photovoltaic materials, such as hybrid organic-inorganic perovskite crystal structures and bulk heterojunctions. My studies of these materials are detailed in later chapters. As mentioned in section 1.1, the dynamics of charge carriers following generation can be complex. Within nanostructured photovoltaic systems understanding and optimising these processes can be complicated further by the nanoscale inhomogeneity of samples, since the dynamic response may vary between sub-ensembles in different locations within the macroscopic sample. [21,22]

1.2.2. Non-linear Optics and Perturbation Theory

Non-linear optical processes are described as multiple interactions of light and matter that lead to modification of the optical response of the material. The response of the material shows a non-linear dependence with respect to the light intensity. Typically, manifestation

of such effects requires the high intensities only possible with laser light. Assuming a lossless and dispersionless material, and treating polarisation and field strength as scalar properties for simplicity, the polarisation (***P***) of the material can be expressed as a power series of the electric field strength (***E***):

$$\begin{aligned} \boldsymbol{P}(t) &= \boldsymbol{P}^{(1)}(t) + \boldsymbol{P}^{(2)}(t) + \boldsymbol{P}^{(3)}(t) + \cdots \\ &= \epsilon_0 \chi^{(1)} \boldsymbol{E}(t) + \epsilon_0 \chi^{(2)} (\boldsymbol{E}(t))^2 + \epsilon_0 \chi^{(3)} (\boldsymbol{E}(t))^3 + \cdots \end{aligned} \tag{1.10}$$

Where the superscripts denote the order of the parameter (*i.e.* $\boldsymbol{P}^{(1)}(t)$ is the first order polarisation), ϵ_0 is the permittivity of free space and χ is the susceptibility of the material.[23]

Under normal (weak) illumination conditions only the first term makes a significant contribution to the polarisability of the material, so a linear relationship between the electric field strength and the macroscopic polarisation is observed. However, under higher intensity coherent illumination, the higher order terms become significant and non-linear optical processes can be realised. Pulsed lasers, especially on the order of 10-100s of femtoseconds in length, are particularly suited to generating non-linear processes because of the high peak power intensities relative to continuous wave sources.

These non-linear processes are vital to laser science and are used to interrogate a large number of different phenomena. Indeed, all the ultrafast time-resolved spectroscopies discussed in this thesis are third-order non-linear optical spectroscopies, requiring third order processes to occur in the sample to generate signal. Data acquired using any time-averaged linear spectroscopic techniques (specifically FTIR and UV/visible absorption spectra) shall henceforth be referred to simply as linear absorption spectra for distinction.

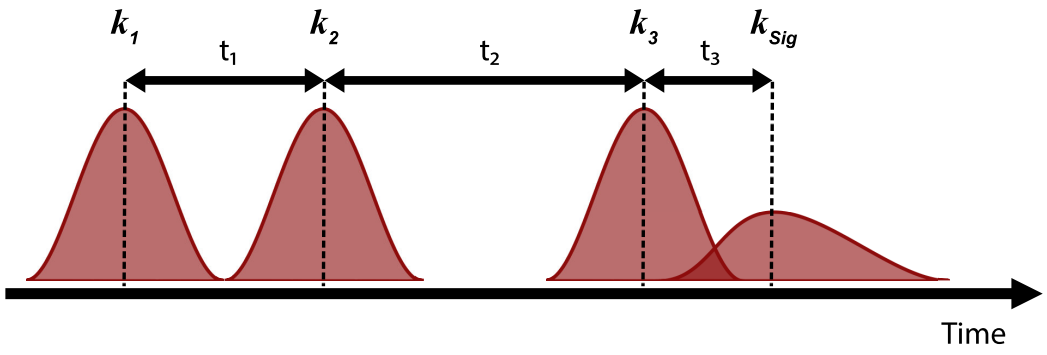

Figure 1.6: Pulse sequence for a third order non-linear spectroscopy experiment.

To generate a third order non-linear signal, a sample must interact with three external fields, or laser pulses,[24] as illustrated in Figure 1.6. The first two pulses, labelled according to their associated wave vectors, $\boldsymbol{k}_1$ and $\boldsymbol{k}_2$, are referred to as pump pulses, and

$\boldsymbol{k_3}$ acts as the probe pulse. As already discussed, when light is incident on a dipole, the oscillating electric field of the light forces the dipole to oscillate. In section 1.2.1 it was implied that light of the resonant frequency could instantaneously excite a population into an excited state, which is a simplified explanation. In reality when a light pulse perturbs a dipole, initially it creates a superposition between the initial and resonant excited states. Using Dirac bra-ket notation, $|n\rangle$ is the nth eigenstate (aka population state) of the time independent Hamiltonian and $\langle n|$ is the complex conjugate of that state. Consider the case for a single molecule with a dipole with three associated energy levels; the initial ground state, $|0\rangle$, with energy E_0, a first excited state, $|1\rangle$, with energy E_1, and the second excited state, $|2\rangle$, with energy E_2, as illustrated in Figure 1.7. If a laser pulse that is resonant with the transition from the ground state to the first excited state perturbs the system, immediately after the interaction the state of the dipole can be described by a linear superposition of $|0\rangle$ and $|1\rangle$:

$$\begin{aligned} |\Psi(t)\rangle &= C_0 \mathrm{e}^{-\mathrm{i}E_0 t/\hbar}|0\rangle + iC_1 \mathrm{e}^{-\mathrm{i}E_1 t/\hbar}|1\rangle \\ &= c_0(t)|0\rangle + c_1(t)|1\rangle \end{aligned} \tag{1.11}$$

Where the coefficients c_n are the relative time-dependent population associated with the two eigenstates. This coherent linear superposition of states is termed a wave packet. The wave packet can evolve with time, according to the response function $R(t)$ of the dipole. If the dipole is not perturbed further, eventually the superposition will collapse, returning the dipole to a population state (either $|0\rangle$ or $|1\rangle$) through the process of decoherence. If the superposition collapses to the ground state, the dipole re-emits a photon with energy equal to $E_1 - E_0$. A photon emitted from a single dipole radiates with a $\sin\theta$ distribution, where θ is the angle between the dipole displacement direction and the propagation direction of the photon. This angular distribution is the cause of the decreased transmission observed at resonant frequencies in linear absorption spectra as light at resonant frequencies can be re-radiated in a direction non-collinear with the initial propagation direction. Notably, the detectors used to measure light intensity in experiments are typically sensitive to the square of the electromagnetic field, resulting in a dependence on the square of the transition dipole moment.

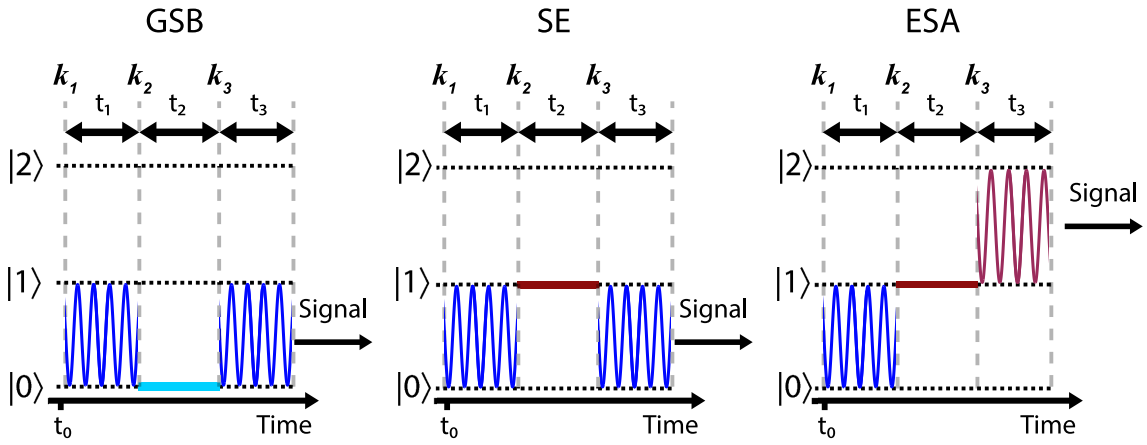

Figure 1.7: Three examples of the way a dipole can respond to the described perturbations

The case just described is for the interaction with only one laser pulse. In the case of the sequence detailed in Figure 1.6 and with reference to Figure 1.7; the first pulse, $\boldsymbol{k_1}$, creates a superposition of states between $|0\rangle$ and $|1\rangle$. If the superposition does not spontaneously collapse within time delay t_1, $\boldsymbol{k_2}$ then acts on the system, and this perturbation converts the superposition into a population of either the ground $|0\rangle$ or the first excited $|1\rangle$ state. After waiting time t_2, $\boldsymbol{k_3}$, the probe pulse converts the system back into a superposition between states. Since there will be population in the ground and first excited states this superposition could between $|0\rangle$ and $|1\rangle$ again (per Figure 1.7(a) or (b)), or between $|1\rangle$ and $|2\rangle$ (see Figure 1.7(c)). It is the collapse of this superposition that generates the signal field detected in third order non-linear spectroscopies. The three cases in Figure 1.7 correspond to (a) ground state bleach, (b) stimulated emission and (c) excited state absorption, and the physical origin will be discussed in section 2.3.1.

Importantly, however, the signal that is detected with ultrafast spectroscopy techniques is the result of a macroscopic polarisation of the sample ($\boldsymbol{P}^{(3)}(t)$ from equation 1.10). The macroscopic polarisation arises from the interference of the individual dipoles within the ensemble and so the ensemble response is measured. Immediately after the first pump pulse perturbs the system, the perturbed dipoles oscillate in phase with each other (because the phase was imparted by the laser field). Consequently, they interfere constructively, creating a large macroscopic oscillating polarisation within the material. With time, however, the ensemble can dephase, gradually diminishing the macroscopic polarisation.

This dephasing occurs because the responses of individual molecules or dipoles within the ensemble varies. This can be considered in terms of the dipoles oscillating at slightly different frequencies or, equivalently, the states of different molecules being at

slightly different energies (Note the energy (E_0 and E_1) dependence of the exponential in equation 1.11). There will always be an intrinsic uncertainty in the energy of the states, but in addition, different molecules may have slightly different energy states due to differences in the environments of the molecules (inhomogeneity). Both of these effects lead to an exponential decay of the macroscopic polarisation (and therefore signal) with time, and since the Fourier transform of an exponential decay is a Lorentzian, this corresponds to the linewidth of the associated spectroscopic feature, with faster dephasing and shorter lifetimes leading to broader line shapes. These two situations will be discussed further in section 2.3.1 in terms of their effect on 2DIR data.

During pump-probe experiments (transient absorption and transient IR in this thesis) there is no t_1 time delay (in the semi-impulsive limit), because both pump pulses arrive simultaneously at the sample from the same beam. Therefore, there is no time for decoherence of individual dipoles, or dephasing of the ensemble to occur in t_1. Instead the maximum population possible is promoted into the excited state. So, the loss of signal is purely due to population relaxation during t_2. However, crucially, in mixed time-frequency domain 2DIR spectroscopy measurements there are two pump pulses and the time delay between them, t_1, is varied, this will be discussed further in section 2.3.2. In all the ultrafast experiments detailed in this thesis the two pump pulses are collinear such that the signal field is emitted colinear to the probe pulse due to $\boldsymbol{k}$-vector conservation:

$$\begin{aligned} \boldsymbol{k_{sig}} &= +\boldsymbol{k_1} - \boldsymbol{k_2} + \boldsymbol{k_3} \\ \boldsymbol{k_{sig}} &= -\boldsymbol{k_1} + \boldsymbol{k_2} + \boldsymbol{k_3} \end{aligned} \tag{1.12}$$

In either instance, as $\boldsymbol{k_1} = \boldsymbol{k_2}$, the signal is always emitted in the $+\boldsymbol{k_3}$ direction. Therefore, rather than the (relatively small) electric field of the signal being detected directly (background free), the probe and signal fields are detected together, and the signal is said to be 'self-heterodyned'. Methods such as phase cycling in 2DIR or modulating the pump pulse in pump-probe experiments are therefore required to extract the desired signal.

Typically, when considering the origin of signals in ultrafast spectroscopy data it is more straightforward to interpret the data in terms of a series of transitions between population states (ignoring coherences between states). Therefore, in the following section the origin of different signals will largely be discussed in this way.

1.2.3. Ultrafast Time-resolved Spectroscopy Experiments

1.2.3.1. Transient Absorption

Conceptually the simplest ultrafast time-resolved spectroscopy technique, and one of the most widely used, is transient absorption spectroscopy (TA), which uses UV, visible or near-IR pump and typically broadband super-continuum probe pulses. The basic components of TA are shown in Figure 1.8. The pump and probe laser beams are focused and overlapped in the sample. Pump pulses are alternately blocked and unblocked (as indicated by a chopper wheel in Figure 1.8) such that the probe pulse interrogates pumped and unpumped sample successively. Note that the waiting time (t_2) and pump-probe time delay (t) are used to describe the same time delay in 2DIR and TA measurements, respectively. This time delay between the pump and probe pulses is varied and at each measured delay time the signal is calculated as:

$$\Delta A(\lambda, t_2) = -\log \frac{I_{pumped}(\lambda, t_2)}{I_{unpumped}(\lambda)} \tag{1.13}$$

for probe wavelength, λ, and at pump-probe delay time, t_2. The dynamics of the sample after excitation can then be followed by monitoring the signal evolution as a function of delay time. For TA experiments, time zero is defined as the time delay when the pump and probe are overlapped in time at the sample so that negative time corresponds to the probe interrogating an un-pumped sampled. As indicated in Figure 1.8, in TA experiments the probe is normally broadband white light, so that a range of wavelengths probe the sample with every laser pulse. The self-heterodyned signal can be digitised by either using a spectrometer to select the wavelength of interest and a single element detector, or instead dispersed onto a CCD array where the entire probe spectrum can be recorded (as indicated in Figure 1.8). The latter case provides the advantage of allowing data to be acquired over many probe wavelengths with each laser pulse.

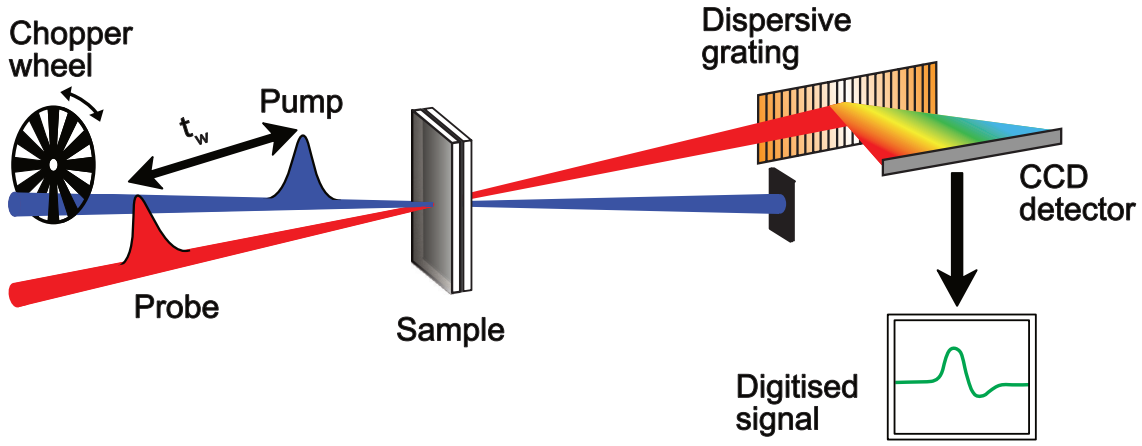

Figure 1.8: Diagram representing key components of TA spectroscopy apparatus

From equation 1.12 it is apparent that processes that cause the sample to (1) absorb more light following excitation result in a positive signal, whereas those that cause the sample to (2) absorb less light, or (3) emit light, give a negative signal. Typically, these three cases can be assigned to three processes: (1) Excited State Absorption (ESA), (2) Ground State Bleach (GSB) and (3) Stimulated Emission (SE), which are explained as follows (see Figure 1.9 for reference): Before excitation the system is in its ground state. Following absorption of photons from the pump pulse at frequency E_{01}, some of the population is transferred to an excited state. The removal of population from the ground state results in the sample appearing more transmissive to the probe at the frequency E_{01} (since there is less ground state population to absorb at this frequency), which gives rise to a negative GSB feature.

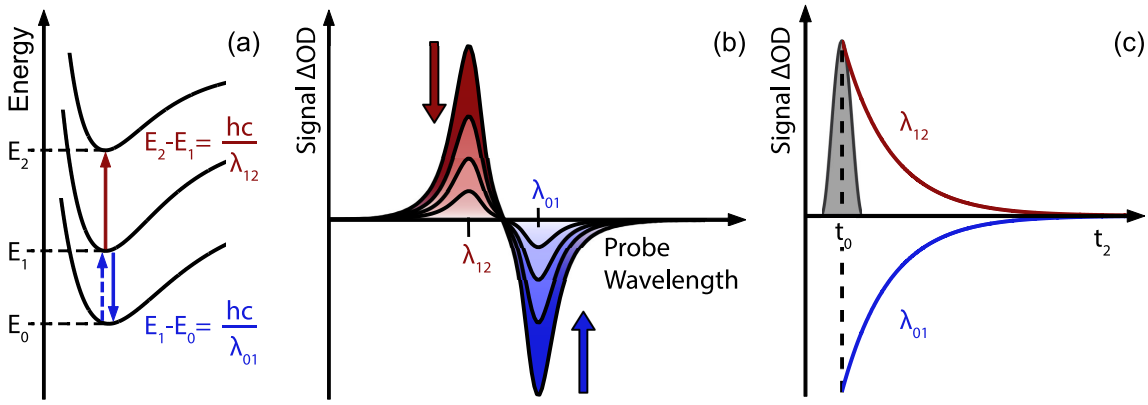

Figure 1.9: (a) The absorption and emission processes between 3 electronic states that lead to GSB/SE and ESA features (b) TA signals for a GSB/SE and an ESA (c) GSB/SE and ESA signal kinetics decaying exponentially

The probe pulse can also stimulate the excited state population to emit a photon (at frequency E_{01}) and return to the ground state, SE, thereby also giving a negative signal at frequency E_{01}. Finally, the excited state population may absorb probe photons and become excited further to a higher excited state resulting in a positive signal, an ESA, at a frequency corresponding to this transition (E_{12}). Note that observation of the ESA and GSB/SE signal relies on E_{01} and E_{12} occurring at different frequencies which corresponds to non-uniform spacing in the electronic energy levels of the system, otherwise the positive and negative signals would appear at the same frequency and potentially cancel out.

Once the origin of a given feature is understood, its dynamics can be used as a convenient way to monitor the population of a given state. For example, in Figure 1.9 plotting the intensity of the ESA or GSB/SE features against pump-probe delay time shows the loss of population from the first excited state. Generally, the rate of decay (or probability per unit time) from a given process or decay pathway is assumed to be constant, and so population decay due to a single pathway can be modelled as an exponential decay:

$$population \propto Ae^{(-t/\tau)} \tag{1.14}$$

Where A is a constant related to the amplitude of the signal and τ is referred to as the lifetime or time constant. Decay from states with multiple decay pathways exhibiting constant decay rates can be modelled as a sum of exponential decays. There are important exceptions to this assumption of a constant decay rate, notably in the case of charge carrier dynamics, where opposite charges can annihilate each other if they collide, so a higher population leads to a greater probability of population loss. Although population dynamics are a core part of transient absorption data, there are many other processes and effects that can lead to changes in signal intensity. Features can overlap, grow rather than decay, and shift in frequency, all of which leads to far more complex data than that described above.

TA is used in this thesis in chapter 2, to measure the photo-active dynamics of hollow gold nanoparticles with J-aggregates on their surface. In chapter 3 a similar technique, time-resolved infrared (TRIR), is also discussed. Like TA, TRIR uses a UV/visible or near-IR pump to excite the sample but probes the sample with a mid-infrared pulse, such that the pump excites the system to a new electronic state, but then transitions between vibronic energy levels are probed. 2D infrared spectroscopy (2DIR) is also used in chapter 3. 2DIR uses a broadband IR pump and probe pulses to interrogate the dynamics of (electronic) ground state vibrational modes. 2D techniques allow both the pump and

probe axes to be frequency resolved, which can provide great insights into system dynamics, and is discussed in more detail in the following section.

1.2.3.2. 2DIR Spectroscopy

2D time-resolved spectroscopies allow for correlation between broadband pump and probe frequencies which is particularly useful to resolve overlapping transient features and isolate cross-peaks as a function of time. [25-28] An example 2DIR spectrum for formamindium lead iodide perovskite thin films (see chapter 3) is shown in Figure 1.10(a), for a positive t_2 delay. As is common for mid-IR data the pump and probe frequencies are displayed in wavenumbers. The pump wavenumber (corresponding to ω_1) is plotted along the horizonal axis and the probe is along the vertical axis (ω_3), as will be the convention throughout this thesis.

2DIR data can be readily interpreted from an understanding of corresponding pump-probe data; one way to view the 2DIR spectrum displayed in Figure 1.10 is if data from multiple narrowband pump-broadband probe spectra acquired at incrementally different pump frequencies but for the same t_2 delay were stacked vertically. Therefore, as per the case for the pump-probe data in Figure 1.9, negative features (displayed in blue in Figure 1.10) can be assigned to GSB/SE, while the positive features (displayed in red) correspond to an ESA. Note that the negative feature is positioned on the diagonal of the plot (indicated by the black line), showing consistent pump and probe frequencies, as would be expected for a GSB. The positive feature, however, is offset from the diagonal because the probe frequency at which the feature is be detected (ω_{12}) is lower in energy than the frequency used to excite the feature (ω_{01}). As mentioned previously, throughout 2DIR measurements the system remains in the ground electronic state, therefore the difference in energy spacing between the vibrational states ($\omega_{01} \neq \omega_{12}$) can be directly attributed to the anharmonicity of the associated vibrational potential well (see Figure 1.10(b)).

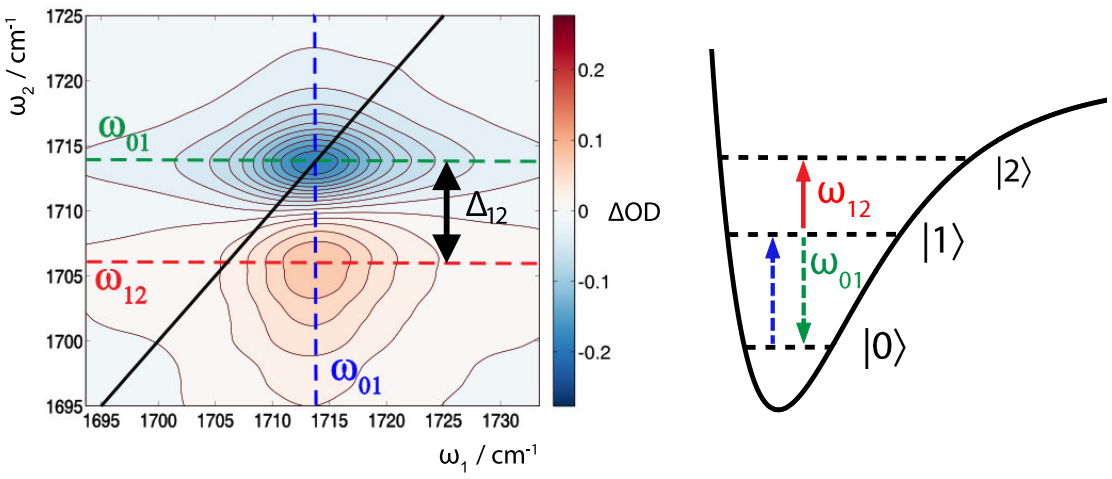

Figure 1.10: Example of 2DIR data acquired at t_2 = 1 ps for formamidinium lead iodide perovskite sample with vibronic energy level transitions corresponding to the signal. 2DIR diagonal indicated by solid black line, dashed coloured lines are to indicate frequencies.

There are many advantages of 2D spectroscopy over 1D counterparts, which facilitates a greater understanding of the system under study. The line-shapes (2D shape of features) resolved in 2D data provides a major advantage when investigating the extent to which a system is homogeneous or inhomogeneously broadened, and the process of spectral diffusion. Broadening refers to the linewidth of features and was briefly mentioned in section 1.2.2. The intrinsic (and minimum) linewidth associated with a spectral feature is called the homogeneous linewidth and results from the intrinsic distribution of energies (or uncertainty) the state can exist at, as dictated by the Heisenberg uncertainty principle: the lifetime of a state is directly related to the uncertainty in the energy of the state. Inhomogeneous broadening on the other hand, results from differences in the environments experienced by the probed species. If a molecule is placed in an electrostatic potential it will affect the energy level spacing of the molecule. Therefore, the electrostatic potential produced by the environment surrounding a photoactive species can cause the absorption/emission frequency of the species to shift. An ensemble of emitters in an inhomogeneous environment such as a solution with a polar solvent, can therefore display a broad distribution of absorption/emission frequencies because of the variety of environments experienced by the molecules (Figure 1.11).

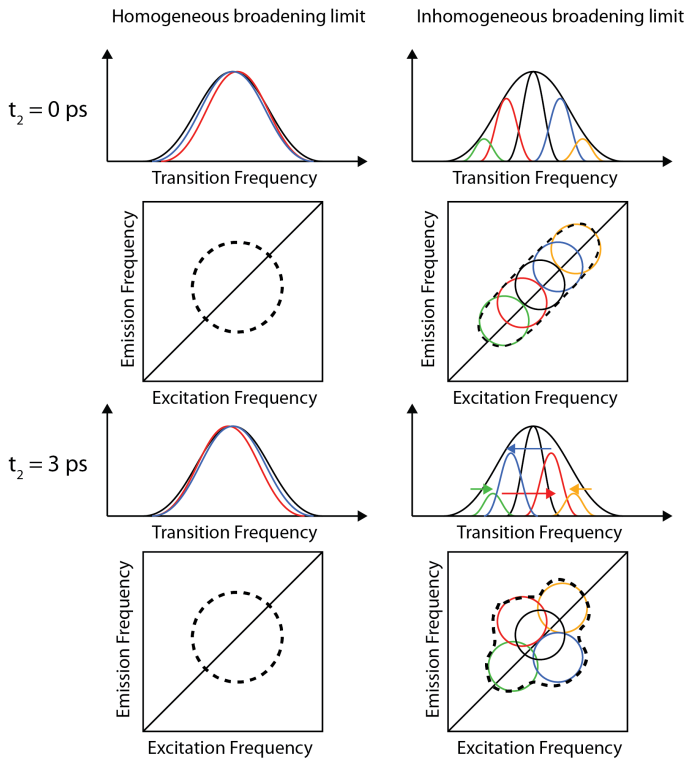

Figure 1.11: The effect of homogeneous and inhomogeneous broadening on 2DIR line shapes for t_2 = 0 and 3 ps.

Since homogeneous broadening is intrinsic, it is static, and the linewidth of a homogeneously broadened feature is equal on the excitation and emission axes. Therefore, an exclusively homogeneously broadened feature appears round in a 2D spectrum (see Figure 1.11) and does not change shape with t_2 delay. In contrast a predominantly inhomogeneously broadened feature appears elongated along the diagonal at early time delays, and the homogeneous line width of the ensemble determines the anti-diagonal width. This is because the different sub-ensemble populations (in different environments) can be excited at different pump frequencies, and initially maintain a correlation between the excitation and emission frequencies (Figure 1.11).

Inhomogeneous broadening is not necessarily a static effect because the environment of the probed species can change with time, dynamically changing the energy levels of the species. If this occurs, the species may interact with the probe at a significantly different frequency to that with which it was excited by the pump. The process of changes in a species' environment destroys the correlation between the excitation and detection frequencies (the frequency-frequency correlation) and is called spectral diffusion. With increasing t_2 delays, it causes spectral features to broaden along the anti-diagonal, destroying any correlation in the ω_1-ω_3 map. The process of spectral diffusion can be monitored in 2DIR data using measures such as the centre line slope (CLS) which quantify

the gradient along which the features are predominantly broadened, thereby giving insight to the timescales of molecule/solvent, or emitter/environment, interactions.[29] The timescale on which spectral diffusion occurs can vary by orders of magnitude between different systems.[30] Another key component of 2D measurements is cross-peaks which result from coupling between two oscillators with different energies. Since coupling strength is highly dependent on distance between the dipoles, cross-peaks are particularly useful for gaining structural information about the system. [28] Cross-peaks are a hallmark of 2D spectroscopy, and therefore important to mention, however no cross peaks were observed in this work, so they will not be discussed further.

There are multiple approaches to acquire 2DIR spectra, and include purely frequency domain methods, or mixed time-frequency domain techniques.[31] Very few 2DIR experiments are now acquired in a purely time domain measurement. Purely frequency domain 2DIR acquisition is similar to hole-burning experiments and effectively operates as described above, repeated measurements (broadband probe) are made while shifting the frequency of the pump between measurements such that a 2D map can be generated. The 2DIR data in this thesis, however, was collected using a mixed time-frequency domain approach. This means the broadband mid-IR signal (collinear to the probe pulse) was frequency dispersed and focussed on a linear array detector. In this pump-probe geometry the pump-probe and 2DIR signals are emitted collinearly, so phase cycling is required to isolate the latter signal and construct the pump frequency axis. Phase cycling exploits the need for two pump pulses interactions (as described in section 1.2.2) to generate a third order signal, by scanning the time delay, t_1, between $\boldsymbol{k_1}$ and $\boldsymbol{k_2}$, causing them to destructively and constructively interfere at different frequencies at the sample. Using a known phase relationship between the pump pulses, only signals reliant on the phase of both pumps can be extracted (*i.e.* pump-probe signals arising from two interactions with one pump are removed) and the pump frequency axis (ω_1) can be constructed using a Fourier-transform along t_1, to generate the final 2D correlation map.

1.3. Summary

Ultrafast pump-probe spectroscopies are a versatile range of techniques that give insight to the rich dynamics of photoactive states with femtosecond time resolution. Time-resolved spectroscopy techniques can be applied to gases, solutions and solid samples. In this thesis I will use three ultrafast spectroscopy techniques to investigate condensed phase

nanomaterial samples. In chapter 2 I will discuss TA measurements of hollow gold nanoshells with J-aggregates in solution. In chapter 3 experiments on thin films of formamidinium lead iodide perovskite using TRIR and 2DIR will be detailed. Finally, in chapter 4, I will outline work to develop a transient absorption microscope to investigate bulk heterojunction thin film samples.

References

(1) Pokropivny, V. V.; Skorokhod, V. V. Classification of Nanostructures by Dimensionality and Concept of Surface Forms Engineering in Nanomaterial Science. **2007**, *27* (5), 990–993.

(2) Kreyling, W. G.; Semmler-Behnke, M.; Chaudhry, Q. A Complementary Definition of Nanomaterial. *Nano Today* **2010**, *5* (3), 165–168.

(3) Dick, K.; Dhanasekaran, T.; Zhang, Z.; Meisel, D. Size-Dependent Melting of Silica-Encapsulated Gold Nanoparticles. *J. Am. Chem. Soc.* **2002**, *124* (10), 2312–2317.

(4) Wu, C.-Y.; Wolf, W. J.; Levartovsky, Y.; Bechtel, H. A.; Martin, M. C.; Toste, F. D.; Gross, E. High-Spatial-Resolution Mapping of Catalytic Reactions on Single Particles. *Nature* **2017**, *541* (7638), 511–515.

(5) Martín-Palma, R. J.; Martinez-Duart, J. M. *Nanotechnology for Microelectronics and Photonics*, 2nd ed.; Elsevier, 2017.

(6) Savage, K. J.; Hawkeye, M. M.; Esteban, R.; Borisov, A. G.; Aizpurua, J.; Baumberg, J. J. Revealing the Quantum Regime in Tunnelling Plasmonics. *Nature* **2012**, *491* (7425), 574–577.

(7) Da Róz, A. L.; Ferreira, M.; de Lima Leite, F.; Oliveira, O. N. *Nanoscience and Its Applications*; William Andrew Publishing, 2017.

(8) Hornyak, G. L.; Dutta, J.; Tibbals, H. F.; Rao, A. *Introduction to Nanoscience*; CRC Press, 2008.

(9) Wolf, E. L. *Nanophysics and Nanotechnology: an Introduction to Modern Concepts in Nanoscience*; Wiley, 2015.

(10) Salata, O. V. Applications of Nanoparticles in Biology and Medicine. *J Nanobiotechnol* **2004**, *2* (1), 3–6.

(11) Seo, J.; Kim, S.; Park, H. H.; Da Yeon Choi; Nam, J.-M. Nano-Bio-Computing Lipid Nanotablet. *Sci. Adv.* **2019**, *5* (2), eaau2124–14.

(12) Sharma, N.; Ojha, H.; Bharadwaj, A.; Pathak, D. P.; Sharma, R. K. Preparation and Catalytic Applications of Nanomaterials: a Review. *RSC Adv.* **2015**, *5* (66), 53381–53403.

(13) Hwang, I. W.; Soci, C.; Moses, D.; Zhu, Z.; Waller, D.; Gaudiana, R.; Brabec, C. J.; Heeger, A. J. Ultrafast Electron Transfer and Decay Dynamics in a Small Band Gap Bulk Heterojunction Material. *Adv. Mater.* **2007**, *19* (17), 2307–2312.

(14) Polli, D.; Altoè, P.; Weingart, O.; Spillane, K. M.; Manzoni, C.; Brida, D.; Tomasello, G.; Orlandi, G.; Kukura, P.; Mathies, R. A.; et al. Conical Intersection Dynamics of the Primary Photoisomerization Event in Vision. *Nature* **2010**, *467* (7314), 440–443.

(15) Scholes, G. D.; Fleming, G. R.; Olaya-Castro, A.; van Grondelle, R. Lessons From Nature About Solar Light Harvesting. *Nature Chem* **2011**, *3* (10), 763–774.

(16) Lakhwani, G.; Rao, A.; Friend, R. H. Bimolecular Recombination in Organic Photovoltaics. *Annu. Rev. Phys. Chem.* **2014**, *65* (1), 557–581.
(17) Jakowetz, A. C.; Böhm, M. L.; Zhang, J.; Sadhanala, A.; Huettner, S.; Bakulin, A. A.; Rao, A.; Friend, R. H. What Controls the Rate of Ultrafast Charge Transfer and Charge Separation Efficiency in Organic Photovoltaic Blends. *J. Am. Chem. Soc.* **2016**, *138* (36), 11672–11679.
(18) Fox, M. *Optical Propertied of Solids*, Second Edition. Oxford University Press, 2010.
(19) Rohatgi-Mukherjee, K. K. *Fundamentals of Photochemistry*; Wiley, 1978.
(20) Heeger, A. J. 25th Anniversary Article: Bulk Heterojunction Solar Cells: Understanding the Mechanism of Operation. *Adv. Mater.* **2014**, *26* (1), 10–28.
(21) Grancini, G.; Polli, D.; Fazzi, D.; Cabanillas-Gonzalez, J.; Cerullo, G.; Lanzani, G. Transient Absorption Imaging of P3HT:PCBM Photovoltaic Blend: Evidence for Interfacial Charge Transfer State. *J. Phys. Chem. Lett.* **2011**, *2* (9), 1099–1105.
(22) Atkin, J. M.; Sass, P. M.; Teichen, P. E.; Eaves, J. D.; Raschke, M. B. Nanoscale Probing of Dynamics in Local Molecular Environments. *J. Phys. Chem. Lett.* **2015**, *6* (22), 4616–4621.
(23) Boyd, R. W. *Nonlinear Optics*, 3rd ed.; Academic Press: London, 2008.
(24) Joo, T.; Jia, Y.; Yu, J. Y.; Lang, M. J.; Fleming, G. R. Third-Order Nonlinear Time Domain Probes of Solvation Dynamics. *J. Phys. Chem.* **1996**, *104* (16), 6089–6108.
(25) Ginsberg, N. S.; Cheng, Y.-C.; Fleming, G. R. Two-Dimensional Electronic Spectroscopy of Molecular Aggregates. *Acc. Chem. Res.* **2009**, *42* (9), 1352–1363.
(26) Oliver, T. A. A. Recent Advances in Multidimensional Ultrafast Spectroscopy. *R. Soc. open sci.* **2018**, *5* (1), 171425–21.
(27) Cho, M. Coherent Two-Dimensional Optical Spectroscopy. *Chem. Rev.* **2008**, *108* (4), 1331–1418.
(28) Hamm, P.; Zanni, M. *Concepts and Methods of 2D Infrared Spectroscopy*; Cambridge University Press, 2011.
(29) Kwak, K.; Rosenfeld, D. E.; Fayer, M. D. Taking Apart the Two-Dimensional Infrared Vibrational Echo Spectra: More Information and Elimination of Distortions. *J. Phys. Chem.* **2008**, *128* (20), 204505–204511.
(30) Kiefer, L. M.; Kubarych, K. J. Solvent-Dependent Dynamics of a Series of Rhenium Photoactivated Catalysts Measured with Ultrafast 2DIR. *J. Phys. Chem. A* **2015**, *119* (6), 959–965.
(31) Shim, S.-H.; Zanni, M. T. How to Turn Your Pump–Probe Instrument Into a Multidimensional Spectrometer: 2D IR and Vis Spectroscopies via Pulse Shaping. *Phys. Chem. Chem. Phys.* **2009**, *11* (5), 748–761.

Chapter 2. Ultrafast Transient Absorption Spectroscopy of Hollow Gold Nanoshells and J-aggregate Hybrids

2.1. Introduction

The optical properties of metallic nanoparticles are one of the epitomising examples of the unusual qualities materials can gain simply by virtue of being reduced to the nanoscale.[1,2] Indeed, gold nanoparticles are often cited in introductory nanoscience texts as the earliest application of a nanomaterial (even if the creators lacked an understanding of the effect); they have been used for centuries to add colour to transparent or translucent materials, such as stained glass, with examples dating back to the 8th century BCE.[3] However, it wasn't until 1852 that Michael Faraday first suggested that the optical properties of the particles could result from their size.[4] Despite this long history, over recent decades understanding of the unusual properties of metallic nanoparticles has increased significantly. The advancement and invention of analytical tools for nanoscience which has made the study of light-matter interactions of metallic nanoparticles a vibrant and very active area of research.[5,6] Gold nanoparticles are already widely used in imaging, sensing, and catalysis but have also shown potential in areas as diverse as solar energy capture,[7] quantum information[8,9] and medicine.[10]

Plasmonics are a key source of metallic nanoparticles' unusual optical properties. Plasmons are the collective coherent oscillations of metallic free electrons. At the surface of materials with a high density of free electrons,[11] *e.g.* metals or heavily doped semiconductors,[12] incident light can excite and couple to plasmons to form surface plasmon polaritons. Polaritons are defined as hybrid particles that are formed by photons strongly coupled to electric dipoles (*polari*sation and pho*ton*), which in the context of surface plasmon polaritons, is the oscillatory electronic dipole of the plasmon.[13] The electric fields of surface plasmon polaritons decay exponentially with increasing distance from the surface and hence are, as the name would suggest, spatially confined to the surface of the material (~20 nm for surface plasmons on metals, excited with visible wavelengths).[14]

Surface plasmon polaritons in nanomaterials can have strikingly different effects to those in bulk materials due to effect of localisation. When a metallic nanoparticle is smaller than the wavelength of incident light, the entire particle experiences an electric field in the same direction, producing a plasmon that is distributed over the entire particle volume, as

illustrated in Figure 2.1. These plasmons can create larger evanescent fields and higher extinction coefficients than surface plasmon polaritons on the surface of bulk metals because they are confined to the nanoparticles.[15]

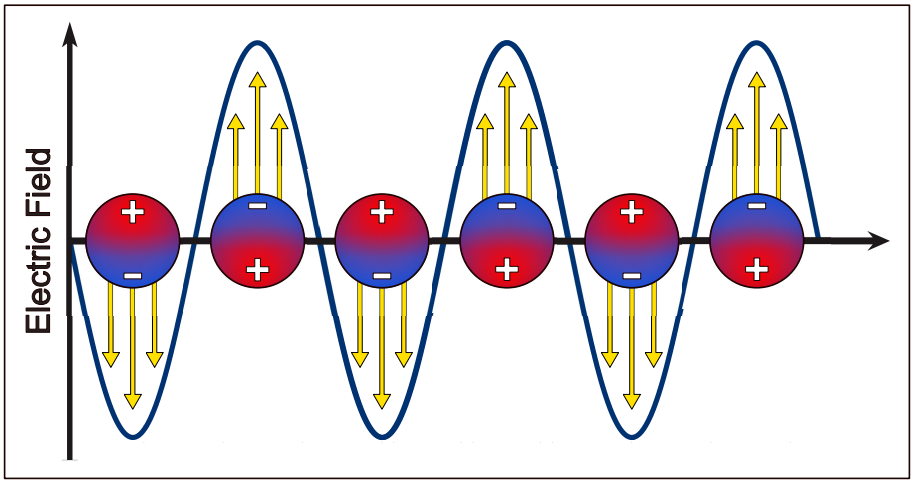

Figure 2.1: Diagram of an incident light field exciting LSPRs in spherical nanoparticles. The change in the free electron charge distribution is indicated by the coloured shading and charges.

Therefore, they are referred to as localised surface plasmon polaritons (henceforth referred to as plasmon) and nanoparticles or nano-structures are said to support localised surface plasmon resonances (LSPRs).[3,12] LSPRs can occur in any appropriately shaped nanomaterials with a sufficiently high density of free electrons.[11] This phenomenon means that LSPRs facilitate the confinement of light to sub-diffraction limit length scales, a concept which is instrumental to the field of nano-photonics.[16]

The confinement means the electric field strength associated with LSPRs can be extremely high at the surface of the nanoparticles. To generate such field strengths without LSPRs would otherwise require powerful lasers or extremely efficient microcavities. These high field strengths can be used to enhance or alter the optical response of other species in close proximity to the nanoparticle through the Purcell effect (the modification of a species' spontaneous emission rate due to its environment[17]) or through direct coupling to the LSPR. To achieve strong coupling often a LSPR is coupled to a molecular exciton with a large dipole strength, and the resulting coupled systems are often referred to as 'hybrids'. Such effects open up numerous potential applications for metallic nanoparticles and have already been applied in surface enhanced spectroscopy techniques such as surface enhanced Raman scattering[18] or metal enhanced fluorescence.[19] Therefore, understanding the coupling between LSPR and other species is both important on a fundamental level but also for application purposes.

Conveniently, the energy of a LSPR peak of metallic nanoparticles can be tuned by changing either the size or shape of the nanoparticle, the surface of the nanoparticle (roughness or coating), or the material of the nanoparticle and its surrounding medium. Gold nanoparticles are commonly used as plasmonic structures since they are comparatively easy to synthesise, have low toxicity, and are efficient plasmon resonators. The LSPRs of many types of gold nanoparticle have be studied including solid gold nanoparticles (SGNs), gold nanocages,[20] nanocubes,[21] nanorods,[22] nanotriangles[23] or nanodisks,[24] and nanoshells.[25] The term gold 'nanoshell' has been used to describe a layer of gold coating a metallic or dielectric core (usually silicon), or, as in this work, a quasi-spherical gold shell which encapsulates some solution from the nanoparticle synthesis. To distinguish the latter case, these particles will henceforth be referred to as hollow gold nanoshells (HGNs).

HGNs are useful plasmonic nanostructures because the energy levels associated with the LSPRs can be tuned to correspond to wavelengths throughout the visible spectrum and into the NIR simply by changing the size of the particle or the shell thickness.[26] Theoretical studies have proposed that this is because HGNs host plasmons on the inner and outer surfaces of the shell which couple and hybridise into bonding and antibonding states delocalised over both surfaces (Figure 2.2). The lower energy (symmetric coupling) mode is predicted to interact strongly with light, whereas the higher energy (anti-symmetric coupling) mode interacts more weakly and additionally is damped by gold interband transitions. Hence what is commonly referred to as the LSPR in HGNs is actually the lower energy hybridised mode. With this model in mind it is interesting to consider how the coupling of the LSPR with an excitonic system may be affected by the proximity of the excitonic species to the inner or outer surfaces of the HGNs. In several studies the electric field strength of HGNs has been simulated and depending on the shell thickness it has been found that the field strength in the cavity can be comparable or higher than the field strength at the outer surface.[27-29] Potentially this could lead to stronger coupling effect for HGNs with excitonic material positioned inside the nanoparticle. However, thus far this consideration has been neglected in experimental work.

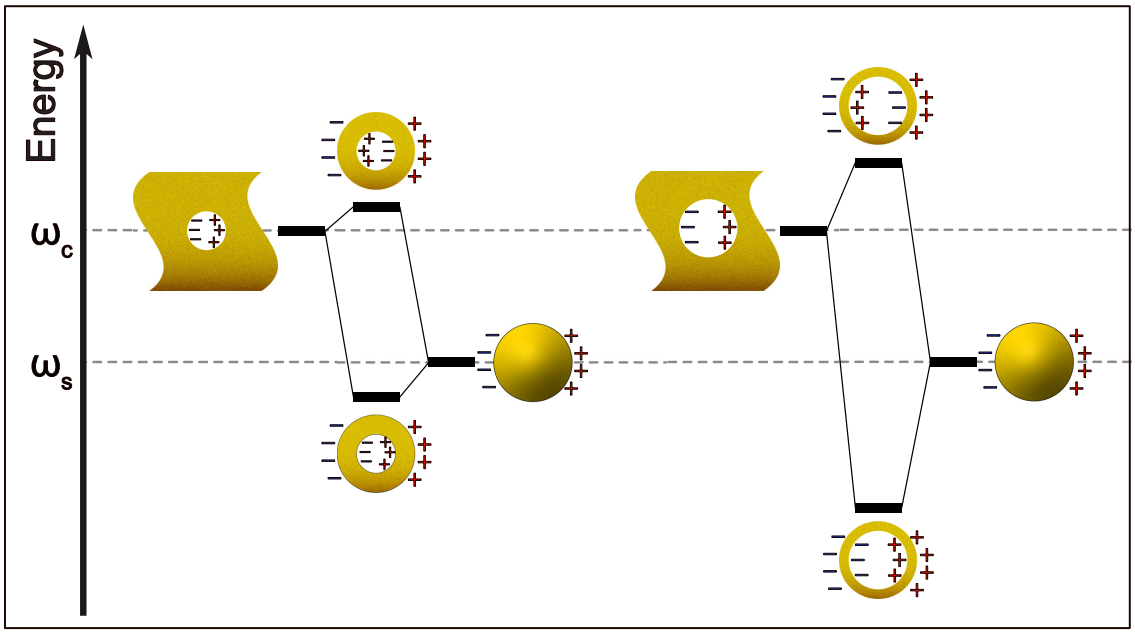

Figure 2.2: Energy level diagram illustrating the effects of hybridisation between LSPRs on the inner and outer surfaces of spherical HGNs, with frequencies ω_c and ω_s respectively, as detailed in ref.[30] The lower energy hybrid mode is symmetrically coupled (as indicated by charge distribution/dipoles) and interacts strongly with light whereas the higher energy (anti-symmetric coupling) does not. A thinner shell leads to a stronger coupling and so a larger splitting.[30,31]

This chapter explores the coupling between excitonic J-aggregates and HGNs using transient absorption spectroscopy. J-aggregates (named after E.E. Jelly who discovered the phenomenon[32]) are supramolecular assemblies of strongly absorbing molecules. Upon aggregation in solution, the absorption spectrum is dramatically changed relative to the monomer: the lowest energy absorption band is significantly narrower and red-shifted. [33] 5,6-dichloro-2-(3-(5,6-dichloro-1-ethyl-3-(3-sulphopropyl)-1,3-dihydro-2H-benzimidazol-2-ylidene)-1-propenyl)-1-ethyl-3-(3-sulphopropyl)-1H-benzimidazolium sodium salt (TDBC) was used as the J-aggregate in this study, with the chemical structure given in Figure 2.3(a). The first electronically excited state of TDBC can be described as a Frenkel exciton (a tightly bound electron–hole pair). The close physical proximity of the molecules within the aggregate leads to strong dipole–dipole coupling and formation of excited states delocalised over many adjacent units (estimated to be 16 monomers in TDBC[34]). The effect of coupling transition dipole moments is illustrated, for the sake of simplicity, for a homodimer (AB) in Figure 2.3(b). In separation the two identical monomers, A and B, have the same excited state energy, E_0. When the two molecules are brought close together, they experience dipole-dipole coupling of strength V. In the strong electronic coupling regime, this yields two new electronic states, E^- and E^+ split by 2V. In

J-aggregates the lower energy state, (E^- in the homodimer) corresponds to the 'J-band'; absorption is the result of hybridisation between adjacent stacked molecules in the aggregate with aligned transition dipoles in a head-to-tail configuration. The higher energy state, E^+, corresponds to an optically dark 'H-band' where molecules lie in the same configuration but head-to-head (and thus the transition dipole moments cancel) leading to an optically dark state. The absorption band is narrowed due to 'exchange narrowing'; electronic energy transfer between the constituent molecules in the J-aggregate occurs on such a fast timescale such that one only sees the average frequency.[35]

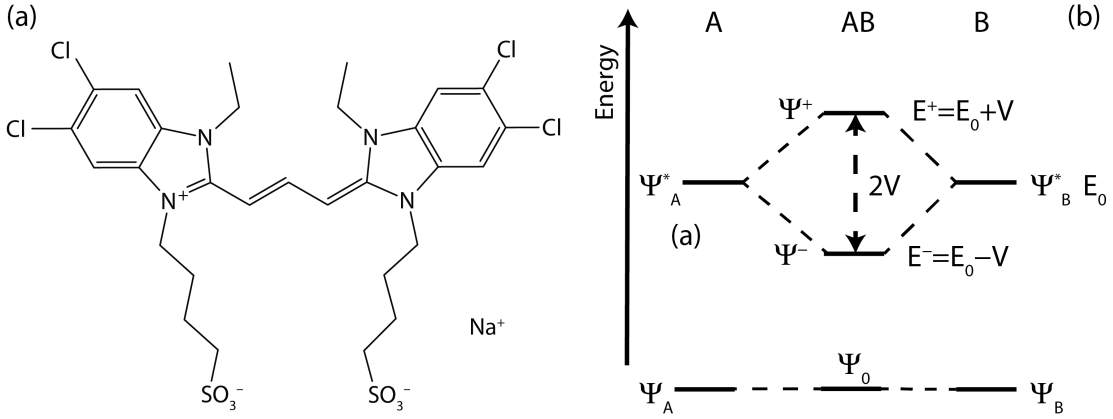

Figure 2.3: (a) Molecular structure of TDBC dye. (b) Schematic energy level diagram for the ground (Ψ) and first excited (Ψ*) states of a coupled homodimer (AB).

The large transition dipole moments of J-aggregates and the high field strength associated with gold nanoparticles' LSPRs, make them an ideal system to study coupling between LSPRs and excitons. There have been several studies of the steady state spectroscopic response of J-aggregates on the surface of both solid[36,37] and hollow[27] metallic nanoparticles. When J-aggregates couple to LSPRs in HGNs a range of spectroscopic responses have been reported, including a decrease in absorption (or 'induced transparency'), near the J-aggregate absorption band maximum, Fano line shapes, or Rabi splitting. Fano resonances result from coupling between a discrete state and a broad continuum of states and can give a variety of dips or inflections in the absorption spectrum line shape of the coupled system. [38,39] Rabi splitting, on the other hand, occurs when energy is exchanged between coupled modes at rates faster than they are damped, causing them to form two hybrid states, with two separate peaks in the coupled system line shape with a difference in energy called the Rabi splitting energy. [40] However, electrodynamic simulations by Faucheaux, *et al.* showed that the seemingly distinct spectral responses could be explained by one underpinning theory, and rationalised by differences of LSPR-

exciton coupling strengths which could be tuned by varying the LSPR damping (or dephasing) rate.[41] Systems with weak coupling between the LSPR and the J-aggregate exciton result in a Fano-type line shape, whereas stronger coupling results in Rabi splitting and the formation of a hybrid plasmon/exciton states, with corresponding quasi-particles: plexcitions.

In terms of ultrafast studies of HGNs and J-aggregates, (as far as I am aware) only one TA study has been published by Fofang *et al.*,[42] although there have been several ultrafast studies of HGNs alone[26,43,44] or SGNs coupled with J-aggregates. [36,45,46] J-aggregates and HGNs exhibit rich time-resolved responses independently, with both species displaying excitation-power dependent kinetics.[42] The study by Fofang *et al.* in 2011 showed that for J-aggregates bound to the outer surface of HGNs the dynamics of the (plexcitonic) hybrid are very different to those of the uncoupled J-aggregate.[42] In addition, they observed two Fano resonance features in the early-time (at pump and probe overlap) line-shape of the complex, which they attribute to coupling to two separate states of the J-aggregate.[42] However, this prior study did not explore the population relaxation channels or investigate effects that may be expected from spectral hole burning.

My collaborator, Dr Núñez Sánchez from the University of Vigo has successfully synthesised HGN with J-aggregates on the inside of HGNs, which provides the opportunity to test how J-aggregate proximity to the plasmons on the inner and outer surfaces of the HGN affects the hybrid particle's optical response, and has never been explored with ultrafast measurements previously. In this chapter TA measurements of three types of nano-shell / TDBC dye J-aggregate hybrid are detailed: nanoshells with J-aggregates only on the outer surface of the shell, only on the inside, and both on the outside and inside of the shell. In addition, spectral filters were used to limit the pump spectral range to investigate the interaction of the two plexcitonic states (or the response either side of the Fano coupling feature) and this represents the first pump wavelength dependence study of J-aggregate-HGN hybrids.

2.2. Experimental Methods

2.2.1. Sample Preparation and Characterisation

All samples were synthesised by the group of Dr Sara Núñez Sánchez, at the University of Vigo (Spain). The HGNs were synthesised using a galvanic replacement, which is a seeded growth method that uses silver nanoparticles to create hollow gold nanoparticles. J-aggregates were added during the water-based synthesis to create HGNs that encapsulate J-aggregates, or afterwards for samples which only have J-aggregates on the surface. The HGNs were stabilised with CTAB (Cetrimonium bromide) to prevent aggregation, except the sample of HGNs in which J-aggregates are only encapsulated inside the HGNs. In order to ensure no J-aggregates were on the surface of these nanoparticles, they were dispersed in ethanol (a solvent where TDBC does not form J-aggregates) and the surface was functionalised with polyethylene glycol (PEG), to prevent TDBC molecules from binding to the HGN surface. As a control and to aid interpretation of the data, solutions of J-aggregates in water, monomeric TDBC in ethanol and samples of HGNs without any J-aggregates with CTAB in water, and PEG in ethanol were also synthesised. The HGNs in each sample were imaged with transmission electron microscopy to determine the particle size distributions, and the visible absorption spectra of the samples were recorded at the University of Vigo before the samples were shipped to Bristol. A summary of the samples, their functionalisation and the abbreviations used throughout this chapter are given in Table 2.1.

Table 2.1: Samples studied in this chapter with details of the functionalisation, solvent and short-hand abbreviation.

Sample	Functionalisation and solvent	Abbreviation
HGNs	CTAB in water	HGN
HGNs with PEG coating	PEG in ethanol	P-HGN
HGNs with J-aggregates outside	CTAB in water	J_SHGN
HGNs with J-aggregates outside & inside	CTAB in water	J_SJ_CHGN
HGNs with J-aggregates inside	PEG in ethanol	P-J_CHGN

2.2.2. Transient Absorption

Transient absorption measurements were performed using an apparatus that I constructed. The pump and probe pulses for these experiments were generated using 40% of the output of a 1W, 1 kHz, 800nm Ti-Sapphire amplifier (Coherent, Libra). A 90:10 beam splitter divided the 0.4 W into two beam lines which were used to produce 600 nm pump and white light probe pulses for the TA experiment, respectively.

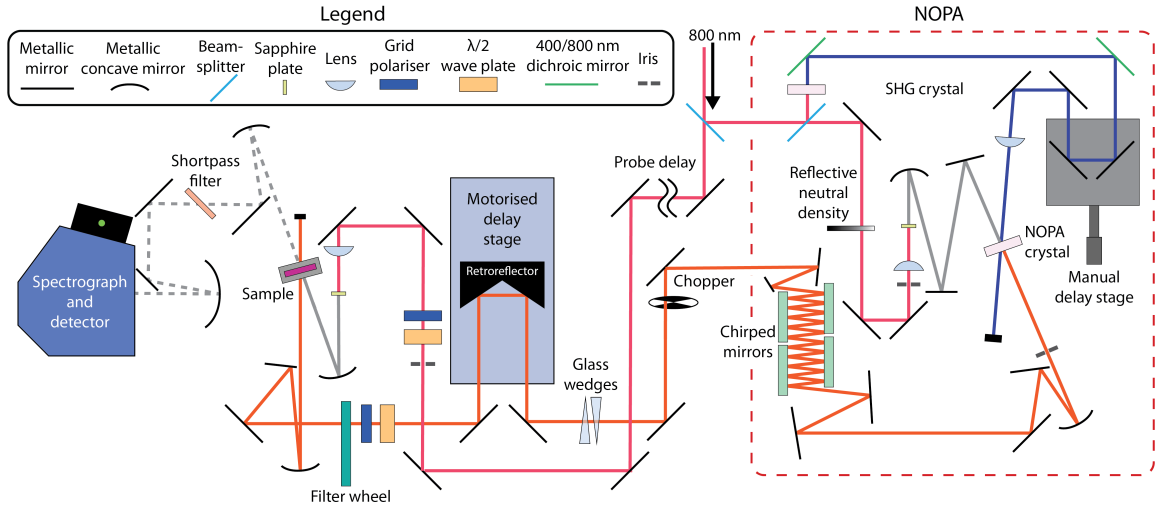

Figure 2.4: Schematic of experimental apparatus used for transient absorption measurements.

The 600 nm pump pulses were generated using a home-built non-collinear optical parametric amplifier (NOPA). The optical layout for the NOPA and experimental setup is given in Figure 2.4. This was achieved by dividing the incoming beam with a 10:90 beam splitter. The 10% beam was focussed into a sapphire plate (2 mm, c-cut Sapphire) with a plano-convex lens (f = 5 cm) to generate a white light seed. A variable density neutral density wheel was used to adjust the intensity of the NIR to ensure the WL generation was stable and spatially homogeneous. The resulting white light (and residual 800 nm) was collimated by a silver concave mirror in a tight 'V' configuration (see diagram) and focused into a BBO crystal (Eksma optics, 5.0 × 5.0 × 2.0 mm crystal, $\theta = 31.5°$, $\phi = 90°$). The 90% portion of the 800 nm beam was frequency doubled in a BBO crystal (Eksma optics, 5.0 × 5.0 × 0.2 mm crystal, $\theta = 29.2°$, $\phi = 90°$) to generate 400 nm. The residual 800 nm was then removed via two 800/400 dichroic mirrors (CVI, BSR-48-1025). The 400 nm beam was routed via a mechanical delay stage and focused into the NOPA BBO crystal with a 20 cm focal length lens (Thorlabs, UV-fused silica, LA4102) and spatially overlapped in the crystal with the white light seed.

The NOPA output was optimised to generate approximately 100 nm of bandwidth (FWHM) centred at 600 nm. This was achieved by iteratively changing the relative spot sizes of the 400 nm pump and the white light seed in the BBO crystal, (both the lens focusing the pump light into the crystal and the collimation/focusing mirror of the white light were on translation stages for this purpose), changing the relative timing of the two pulses (controlled by the mechanical delay stage in the 400 nm beam line), altering the BBO crystal angle, and changing the crossing angle between the seed and 400 nm pump beams. The beam mode of the resulting NOPA output was inhomogeneous, so the most intense and uniform part of the generated light was isolated using an iris and collimated with a curved silver mirror (f = 25 cm).

The NOPA output (see spectra in Figure 2.5) was inevitably chirped due to the transmissive optics used and non-linear crystals. Therefore, three sets of chirp mirrors (Layertech 148545, 470–810 nm GDD = –40 fs^2 per pair of bounces) were used for pulse compression. The beam was then directed onto a silver retroreflector (PLX, OW-20-1) on a motorised high precision delay stage (Physik Instrumente, M-531.DG1, 305 mm travel corresponding to a maximum delay of ~2 ns) before being focused into the sample with a (f = 20 cm) plano-concave silver mirror. Neutral density filters and spectral filters were used in the pump line before the sample, both filters were pre-compensated for in pump pulse compression. At the sample the pump beam focal spot size was approximately 90 µm in diameter.

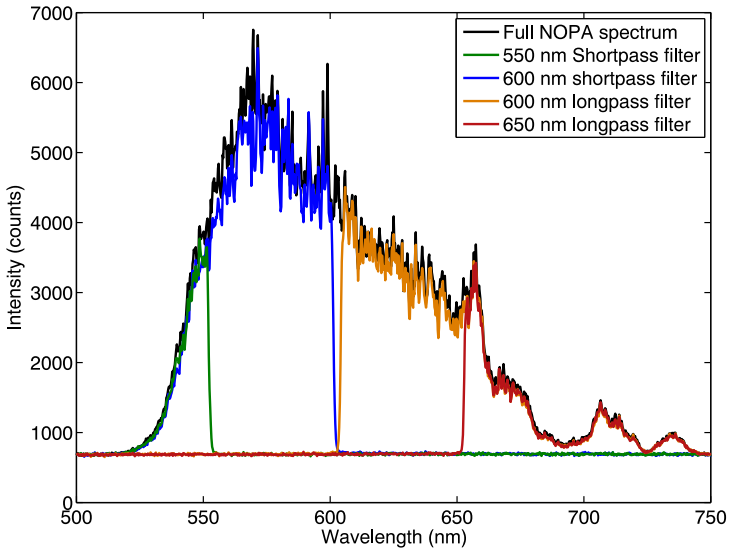

Figure 2.5: Pump NOPA spectrum before spectral filtering (black line) and with different filters (coloured lines).

The white light probe was generated by focusing the 800 nm beam in a sapphire plate (2 mm, c-cut Sapphire) after an approximately 4 m delay line to match the NOPA pathlength. A polariser/waveplate pair were used to attenuate the 800 nm light before the sapphire crystal to allow the intensity of the 800 nm light to be adjusted to give stable white light continuum. The polariser was also used to set the relative polarisation of the white light probe to the 600 nm pump. The generated white light (and residual 800 nm) was focused into the sample using a convex silver mirror (f = 20 cm) and overlapped with the pump beam at the focus. After the sample the probe beam (with the collinear signal) was collimated using a 2" diameter curved mirror (f = 25 cm). Before the detector the residual 800 in the white light was removed by means of a long-pass filter (Thorlabs DMSP750B). Any residual pump scatter was removed with a polariser (Meadowlark, GPM-100-UNC) positioned parallel to the polarisation of the probe.

The WLC probe and signal were focused using a 2" diameter convex mirror (f = 15 cm) onto the slit of a Czerny-Turner spectrograph (Shamrock 163, Andor) which frequency dispersed and focussed the beams onto a linear 1024 element CCD array detector (Entwicklungsbüro Stresing). The spectrograph was calibrated using the Neon emission lines from a calibration lamp (Newport, 6032) before data acquisition.

The digitised data were recorded using a Labview acquisition program. Data were recorded at the repetition rate of the laser (1 kHz) in blocks of 1000 shots. Each block was comprised from alternating pump on and pump off shots. From these data, 500 transient absorption (recorded in ΔOD, as defined in equation 1.13) were generated. The statistics of these spectra were then analysed and used to reject any data within the series that deviated from the mean by a standard deviation of 0.4, and thus rejected ~60% of the data acquired. Subsequently the data were then averaged and written to a data file. This procedure was repeated for a large variety of pre-programmed time delays to form one cycle. The data were then averaged over multiple cycles (typically between 5–10 depending on the signal-to-noise ratio).

A cuvette of dye solution (Oxazine 4 dissolved in methanol) was used to find time zero (pump and probe temporally overlapped in the sample). Then the position of the sample cell, the spot sizes of the pump and probe, and their overlap in the sample were adjusted to maximise the TA signal. For all measurements, the relative polarisation of the pump and probe pulses was set to magic angle. Samples were diluted prior to TA measurements to obtain a maximum OD between 0.3–0.6. Measurements on PEG coated

samples were performed in static UV fused silica cuvette with a 1.0 mm pathlength (Starna, Type 21), as they were found to adhere to the surfaces of the optical cells. All other samples were continually flowed throughout experiments in 0.5 mm pathlength UV fused silica flow cells (Starna, Type 48). Following TA measurements, the visible absorption spectra of the samples were recorded to ensure no degradation occurred.

2.3. Results & Discussion

2.3.1. Pulse Compression and Characterisation

The pump was compressed by iteratively changing the number of bounces between the chirp mirror pairs to maximise the intensity of coherent oscillations in TA measurements of Oxazine 4 dye. The origin of this signal is a vibrational wave packet, and its intensity is directly proportional to the pump pulse duration. [47] Once the compression was optimised, the non-resonant cross-correlation between the pump and probe was measured in a water sample to estimate the duration of the instrument response function (IRF). An example is shown in Figure 2.6(a), where it is evident that the non-resonant cross-correlation signal at shorter probe wavelengths occurs at earlier time delays than for longer probe wavelengths due to the positively chirped white light supercontinuum probe. This was corrected for in all datasets with post-measurement processing. The black line in Figure 2.6(b) shows the cross-correlation signal averaged over all the probe wavelengths (480–700 nm) in the chirp-corrected data. It shows an intense positive feature flanked by two less intense negative features. This line shape is characteristic of coherent artefacts induced by cross phase modulation, which is common in pump-probe experiments utilising chirped white light super continuum probes.[48] Ernsting and co-workers[49] derived an analytical expression to fit this functional form, in the limit the probe pulse is far longer than the pump, and allows for the pump pulse duration to be estimated:

$$\Delta OD(\omega_{pr}, t) \approx Ce^{\frac{[-t+t_0(\omega_{pr})]^2}{\Delta_{pu}^2}} \times \sin\left[\frac{1}{2\beta\Delta_{pu}^2} - \frac{[t+t_0(\omega_{pr})]^2}{2\beta\Delta_{pu}^4}\right] \qquad (2.1)$$

Where t is the pump-probe time delay, $t_0(\omega_{pr})$ is the probe frequency dependent time zero, β is the chirp rate, Δ_{pu} is the pump pulse duration and C is the cross-phase modulation amplitude. Fits to the data (overlaid dashed blue line in Figure 2.6(b)) to equation 2.1 returned an IRF of 27 fs.

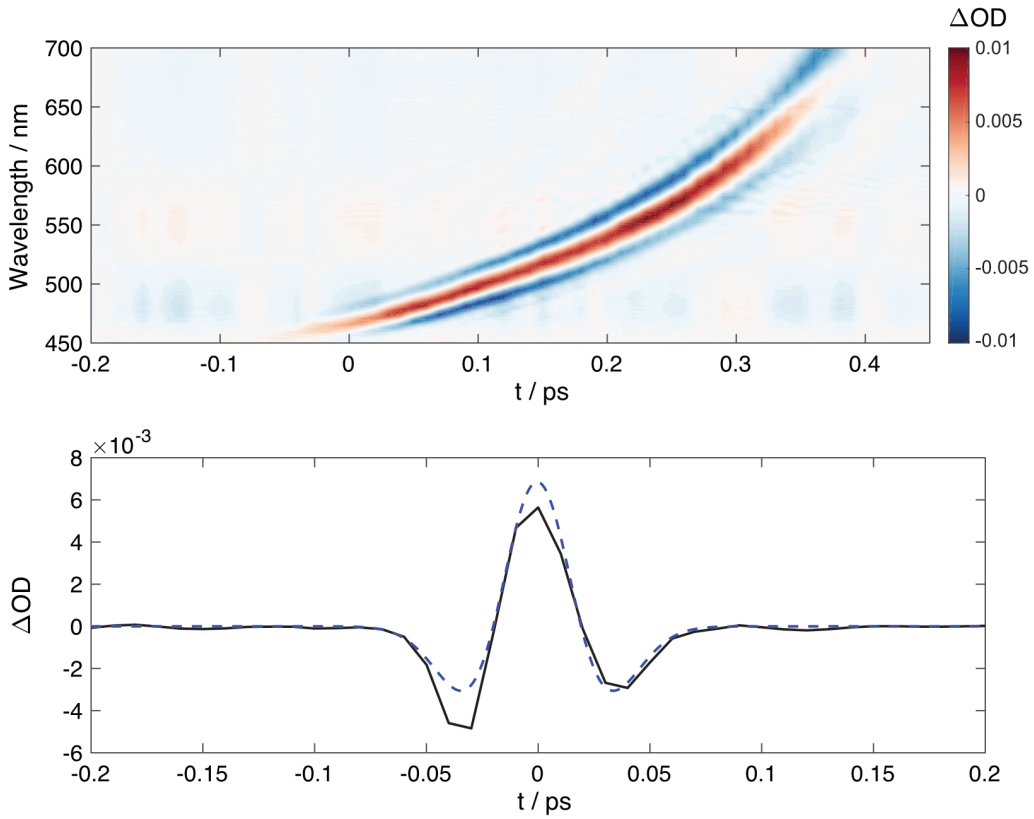

Figure 2.6: (a) Non-resonant signal of the pump-probe overlap (time 0) in methanol (b) average response taken over probe window (black line) after chirp correction data processing and a fit to IRF using eq. 2.1 (blue dashed line).

2.3.2. Sample Characterisation

TEM measurements of the HGNs taken and analysed at the University of Vigo give an indication of polydispersity of our samples (see Table 2.2) and revealed 8–9% variation in the particle diameters.

Table 2.2: HGN particle diameters as determined by TEM measurements by Dr Núñez Sánchez's group.

Sample	Particle Diameter / nm
HGN	85 ± 8
P-HGN	87 ± 7
J_SHGN	87 ± 8
$J_S J_C$HGN	77 ± 7
P-J_CHGN	86 ± 8

Linear visible absorption spectra of the samples are shown in Figure 2.7. All HGNs samples exhibited a broad LSPR absorption peak at ~600 nm (Figure 2.7(b-f)), which is consistent with prior studies.[29] The asymmetry in the LSPR absorption line shape is the result of underlying gold inter-band transitions,[50] which occur at ~2.4 eV (516 nm), with a weak absorption tail down to ~1.8 eV (689 nm). During synthesis the thickness of the HGNs was optimised to tune this resonance to peak at approximately 600 nm to coincide with the J-aggregate absorption maxima (587 ± 1 nm), see Figure 2.7(a). The absorption line shape associated with HGN LSPRs (Γ) is very broad and in the homogeneous broadening limit, the linewidth of the LSPRs is given by*: [6,51,52]

$$\Gamma = \frac{2\hbar}{T_2^*} + \frac{\hbar}{T_1} \tag{2.2}$$

where T_2^* is the pure dephasing timescale, and T_1 is the contribution from population relaxation. It has been shown for gold nanoparticles that the T_1 term is dominant and hence the homogeneous linewidth can give a direct measure the population lifetime.[6,51,52] In this limit, broad LSPR line shapes are indicative of short LSPR lifetimes, *e.g.* a 400 meV line width yields an LSPR lifetime of ~10 fs. [52]

* Note, in some literature the time taken for the oscillating electrons that form the plasmon to lose their phase relationship (destroying the plasmon polariton) is referred to as decoherence time,[29] in others it is referred to as the dephasing time.[6,51] In this work I use the term dephasing time.

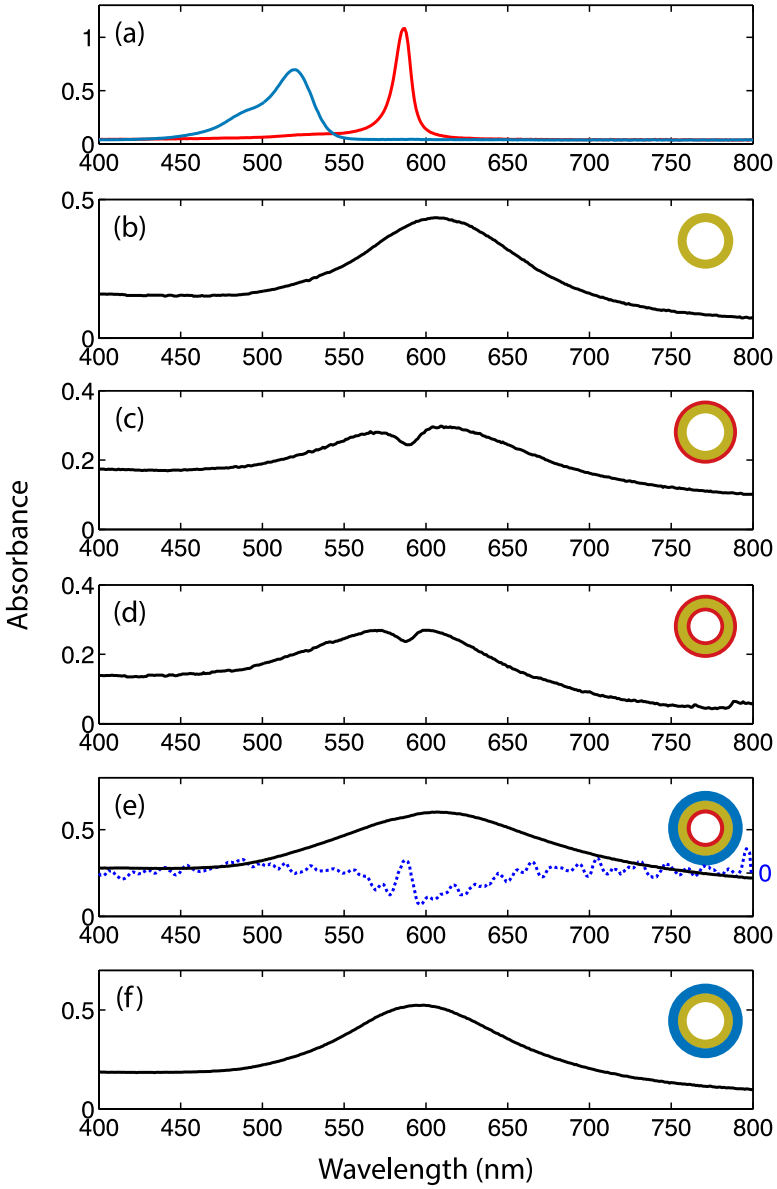

Figure 2.7: Visible absorption spectra of samples: (a) TDBC monomer (blue line) and TDBC J-aggregate (red line) in ethanol and water respectively (b) HGNs in water, (c) J_SHGNs in water, (d) J_SJ_CHGNs in water (e) P-J_CHGN in ethanol with first derivative (blue dotted line), and (f) P-HGN in ethanol.

In the hybrid samples, there is an evident decrease in absorption where the J-aggregate absorption is expected. This effect has been attributed to coupling between the HGN and J-aggregate, and is most apparent for the sample where the J-aggregates are on the outside of the nanoparticle (J_SHGN- see Figure 2.7(c)). The linear spectra of HGNs with J-aggregates on the inside only (J_CHGN) only exhibit a slight indent at the J-aggregate absorption peak (Figure 2.7(e)), which may arise due to far weaker coupling *cf.* J_SHGN. To highlight this feature the first derivative of the absorption spectrum is included in Figure 2.7(e).

It is common practice to use the energy difference between the two peaks as a measure of the coupling strength.[45,53,54] This analysis returns values of 100 ± 10 meV for the J_SJ_CHGN samples and 143 ± 10 meV for J_SHGN. Comparing this data to the simulations by Faucheaux *et al.,*[41] the absorption spectra in Figure 2.7 are most similar to those classified under the strong Fano resonance category. Faucheaux *et al.* stated that the most important factor in determining the coupling strength of HGNs and J-aggregates is the plasmon linewidth (Γ) and distinguish between two coupling regimes based on a comparison of line widths (and thus pure dephasing) of the plasmon, Γ, and exciton (ω). The strongly coupled Rabi splitting regime is defined when the plasmon oscillator is weakly damped so the associated linewidth is very narrow compared to the excitonic resonance ($\Gamma << \omega$) and conversely, the weakly coupled Fano regime occurs when the plasmon is heavily damped, so its linewidth is broad compared to the exciton line shape ($\Gamma >> \omega$). Taking half the FWHM of the HGNs sample on the red side of the spectrum (a method used by Berciaud *et al.* to avoid the effects of the intra-band transitions on the line-shape[50]), gives a FWHM value of 400 ± 20 meV. The corresponding FWHM of TDBC J-aggregates is 35 ± 5 meV, and thus indicates my HGNs fall within the Fano coupling regime.

2.3.3. Transient Absorption Results

Unfortunately, the sample with J-aggregates only on the inside of the HGN (P-J_CHGN) did not exhibit sufficiently strong coupling for the effect to be obvious in TA studies. Based on preliminary measurements not discussed here, I am confident that a different sample exhibiting stronger coupling (*e.g.* gold thinner shell) would enable this to be studied. Therefore, the following discussion focusses on understanding the response of the HGNs with J-aggregates on the outer surface, and J-aggregates on the inside and outside. However, before addressing the effects of coupling to J-aggregates, in the following section I will discuss the TA response of J-aggregates and the HGNs independently, which exhibit complex dynamics in their own right.

2.3.3.1. J-aggregates

Figure 2.8(a) displays TA data for selected pump-probe time delays of TDBC J-aggregates in water. The dispersive line-shape with an asymmetric tail on the shorter wavelength side is typical of previous studies.[34] It is well established that the J-aggregate transient line-shapes are determined by the number of molecules within the aggregate that excitation is delocalised over (delocalisation chain length), [34] which depends on the J-aggregate formation conditions. [33] The negative feature in Figure 2.8(a) corresponds to overlapping GSB/SE from the one-exciton state. A one-exciton state corresponds to a single excitation spread out over the delocalisation chain length within a J-aggregate.

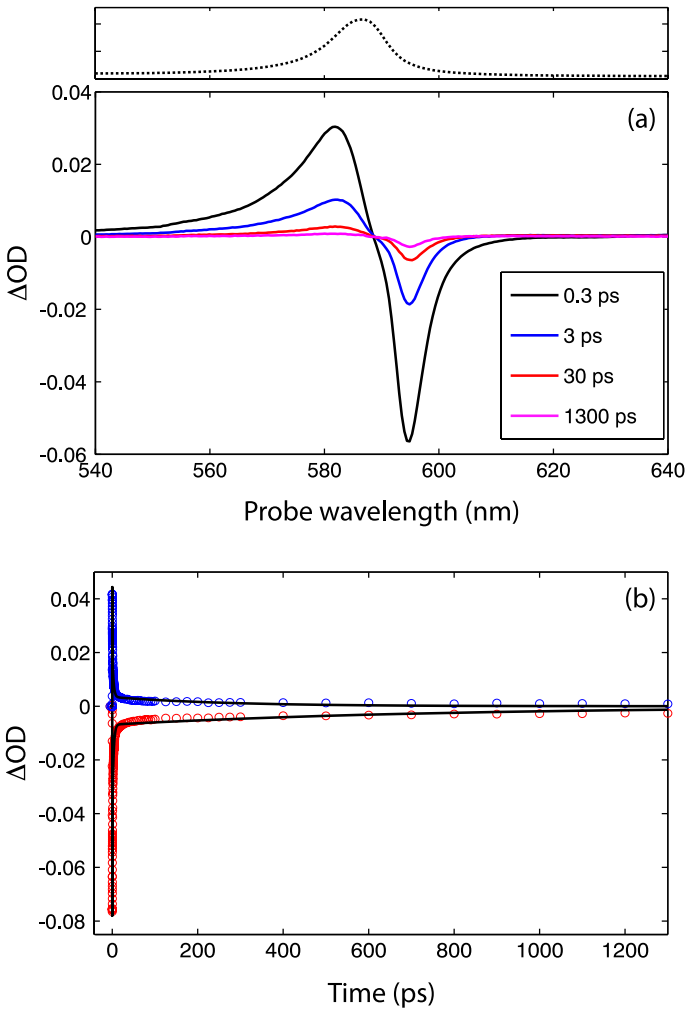

Figure 2.8: (a) TA spectra of TDBC J-aggregates in water solution for the displayed pump-probe time delay, with the linear absorption spectrum for reference. (b) Kinetics associated with the GSB/SE at 595 nm and ESA features at 580 nm (open circles) overlaid with fits to a Gaussian convolved with a three-part exponential decay function (black solid lines).

The positive feature present at shorter probe wavelengths is an ESA corresponding to a two-exciton state, *i.e.* a second exciton is generated within the same delocalisation

length, or region of the aggregate as the original exciton.[47,48] Due to electron-correlation, excitation of the second exciton requires more energy than the first, so the ESA is blue-shifted relative to the bleach. The kinetics (single wavelength slices) associated with these two features (580 nm for the ESA, and 595 nm for the bleach) are shown in Figure 2.8(b), and display an instantaneous rise (within the IRF) followed by a multi-component decay. The kinetics of the GSB/SE at 595 nm and ESA at 580 nm were fitted with a Gaussian convoluted with a triexponential decay to model the IRF and excited state relaxation dynamics respectively, as shown in Figure 2.8(b). This returned time constants (τ_1, τ_2 and τ_3) and corresponding amplitudes (A_1, A_2 and A_3) given in Table 2.3.

Table 2.3: Time constants and corresponding amplitude components from a triexponential fit to the GSB/SE and ESA features of TDBC J-aggregate data

Feature	Time constants and associated amplitudes					
	τ_1 / ps	A_1 / %	τ_2 / ps	A_2 / %	τ_3 / ps	A_3 / %
GSB/SE	0.32 ± 0.02	52 ± 6	2.7 ± 0.1	40 ± 5	800 ± 200	7.4 ± 0.8
ESA	0.29 ± 0.02	56 ± 6	2.7 ± 0.1	37 ± 4	260 ± 60	6.8 ± 0.8

Based on prior studies, the sub-picosecond and several picosecond time constants, which are in agreement within the reported uncertainty for both the ESA and GSB/SE features, can be attributed to exciton-exciton annihilation, *e.g.* two excitons within the same J-aggregate migrate towards each other and form a two-exciton state. This two-exciton state then relaxes via internal conversion to the one-exciton state. This causes the GSB feature to recover more quickly than the ESA feature in the shortest time component. However, the SE from the 1-exciton state is unaffected by these dynamics.[34] The 100s of picosecond component decays more slowly for the GSB/SE feature compared to the ESA. Van Burgel *et al.* reported a 220 ps time constant for the fluorescence lifetime from the TDBC one-exciton state,[34] which is similar to the third time constant of the ESA measured here. The inconsistency with the much longer third time-component of the GSB/ESA is likely due to intersystem crossing from the one-exciton manifold into a triplet state that does not have a spectroscopic signature in the white light supercontinuum probe window.[54] For a more comprehensive analysis of these time constants, exciton-exciton annihilation should not be modelled as an exponential decay, since the rate of annihilation decreases with the population density, however this a well-studied phenomenon and diverges from the focus of this chapter.[55]

2.3.3.2. Hollow Gold Nanoparticles in Water

TA data of the HGNs in water were recorded at six different pump pulse energies between 15 and 90 μW. All the recorded datasets show a negative bleach feature centred at approximately 605 nm, flanked by two positive features, with maxima at ~500 nm and typically greater than 700 nm, henceforth referred, out of convenience, to as high and low energy ESAs. TA spectra recorded with 90 μW pump pulses are displayed in Figure 2.9(a). The maxima associated with these features shift as a function of the time delay and exhibit rich dynamics over a variety of timescales. As Figure 2.9(b) shows, all features in the spectra rise on a ~0.5 ps timescale, in clear contrast to the J-aggregate data (Figure 2.8(b)).

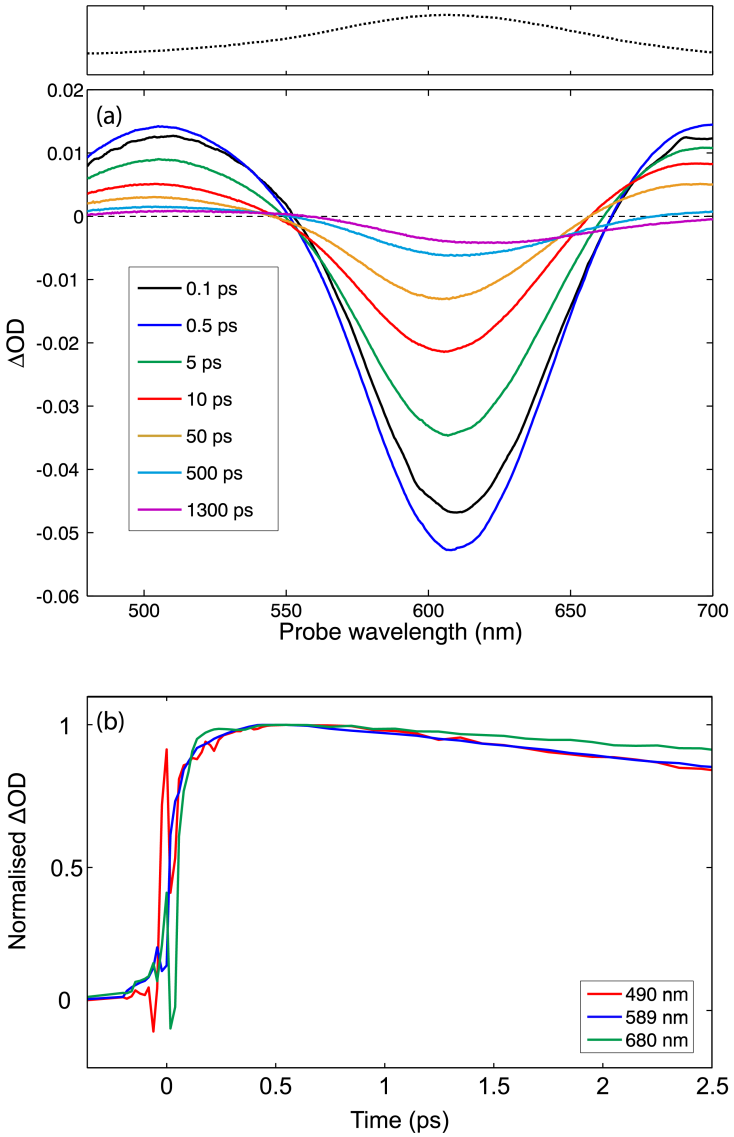

Figure 2.9: (a) TA spectra for HGNs in water for the indicated pump-probe delays using 90 μW pump pulses, (b) single wavelength kinetic slices for the GSB/SE (589 nm) and ESA (490 and 680 nm) features. The 'spike' at time zero in the 490 nm trace arises from cross-phase modulation.

Between 1 ps and ~200 ps the kinetics associated with the GSB/SE and ESAs exhibit an oscillatory behaviour in intensity with a period of ~50 ps as shown in the 2D contour map in Figure 2.10. Further, the peak wavelengths associated with these features also oscillate in wavelength with this period (see the black line in Figure 2.10 for the minimum of the bleach feature). The effect is most obvious in the kinetics of the low energy ESA, where amplitude of the oscillatory part of the signal is significant compared to the underlying population dynamics. Finally, at late time delays, the bleach feature appears to red-shift. These observed complex dynamics must result from overlapping features shifting in frequency and decaying on different timescales.

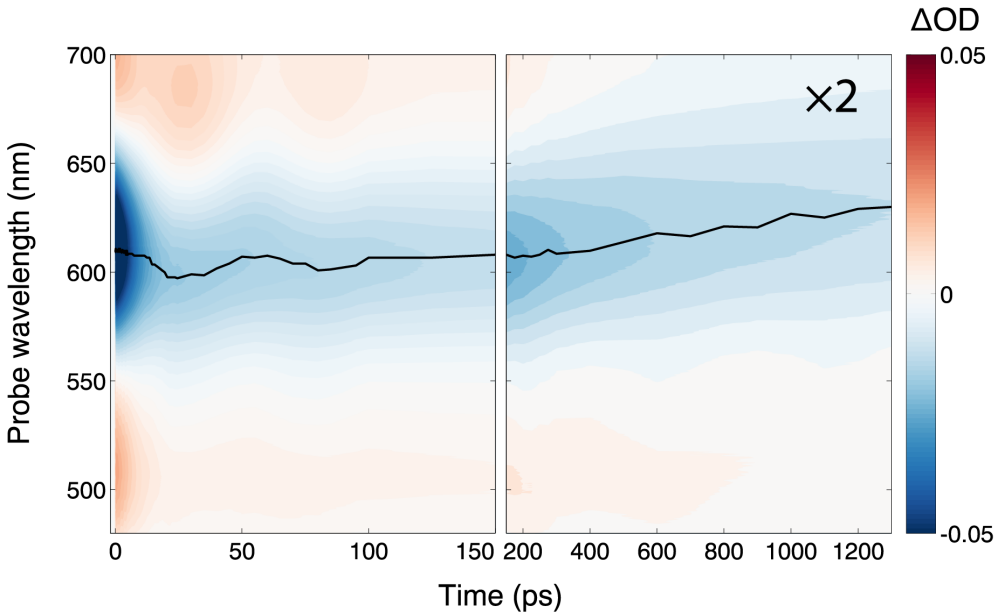

Figure 2.10: Contour map of the same data as in Figure 2.9(a) showing the early (0–150 ps) and late (200–1250 ps) data on different time axes. Note that the intensity of the transient signal for 200–1250 ps time delays has been scaled by a factor of 2.

The features and dynamics observed in my data are consistent with previous TA studies of both HGNs[26,43,44] and SGNs. [56-58] Although the origin of the ESAs and slow rise have not been properly established for HGNs, the origin of such features have been far more thoroughly studied for SGNs,[58-60] and the early time processes giving rise to observed dynamics were explained as follows:

(1) The pump pulse excites LSPR at the plasmon resonance frequency and, if sufficiently energetic, gold interband transitions.
(2) The plasmon dephases in ~10 fs, producing a non-thermal electron population.
(3) This electron population thermalises through electron-electron scattering on a ~500 fs timescale, producing the observed slow-rise in the feature kinetics.

(4) This results in a 'hot' electron population, with energies easily equivalent to thousands of degrees, and thus very far from equilibrium with the metal lattice's phonon population.
(5) The hot electrons change the electronic properties of the metal, causing the plasmon band to broaden and shift in central frequency, producing an overlapping positive transient feature that dominates the wings of the ground state bleach feature.
(6) Electron-phonon coupling allows the electron population to cool, transferring energy to the phonon population on a sub-picosecond timescale. (*e.g.* repartition of the energy)
(7) This impulsive heating of the lattice initiates an expansion of the NP and thus drives coherent nuclear breathing modes of the NPs.
(8) The NPs couple to the surroundings (bath) through phonon-phonon coupling and finally dissipate the excess energy in the system.

For the HGN data presented here, the slow rise of the features at early time is consistent with point (3) above.[58] The two ESAs and the GSB/SE features rise to a maximum/minimum intensity between 360 and 550 fs, for all of the measured pump powers, which indicates that the rise time is not affected by the effective temperature of the hot electron population, which is expected in the weak perturbation regime. [52]

The origin of the two ESA features is explained by (5), they are the result of the new plasmon band position of the excited particle. In a study of solid gold nanoparticles, Hartland *et al*. modelled the TA line shape with a sum of two Lorentzian functions: [61] a negative function that models the bleach of the plasmon band, and a slightly broader, positive Lorentzian that models the new position of the plasmon band following excitation. Figure 2.11 shows a similar analysis applied to my HGN data at 1 ps for 90 μW pump power. The data was fit (without any imposed constraints) yielding fit parameters shown in Table 2.4. Also shown in Figure 2.11 is a similar fit using a sum of two Gaussians, and the parameters are given in Table 2.4.

The two fit types result in markedly different line shape components for the negative bleach/SE and the positive ESA features. The Gaussian sum shows a much narrower negative feature than the positive one, whereas the linewidths from the sum of Lorentzians are comparable. Similarly, the central peak position of the two Gaussians are separated by ~30 nm, whereas the Lorentzian line-shapes have consistent central

wavelengths. A broadening and shifting of the ESA relative to the bleach would be expected from the early-time processes, and given the aforementioned effects of size polydispersity in the sample it is reasonable to expect the bleach and ESA line-shapes to more closely resemble a Gaussian than a Lorentzian due to some inhomogeneous broadening component (see Table 2.2). Based on this reasoning and the better fit returned by a sum of Gaussians, I conclude that this is the most appropriate way to model my data.

Table 2.4: Parameters returned from fitting 1 ps transient HGN transient absorption spectrum to a sum of Lorentzian or Gaussian functions.

	Linewidth / nm	Central wavelength / nm	Amplitude factor	Relative intensity of peak
Lorentzian sum	160 ± 30	610.9 ± 0.9	100 ± 200	47 %
	140 ± 20	610.2 ± 0.5	–100 ± 200	53 %
Gaussian sum	260 ± 30	640 ± 10	0.0174 ± 0.0005	20 %
	47.3 ± 0.3	609.2 ± 0.1	–0.0676 ± 0.0006	80 %

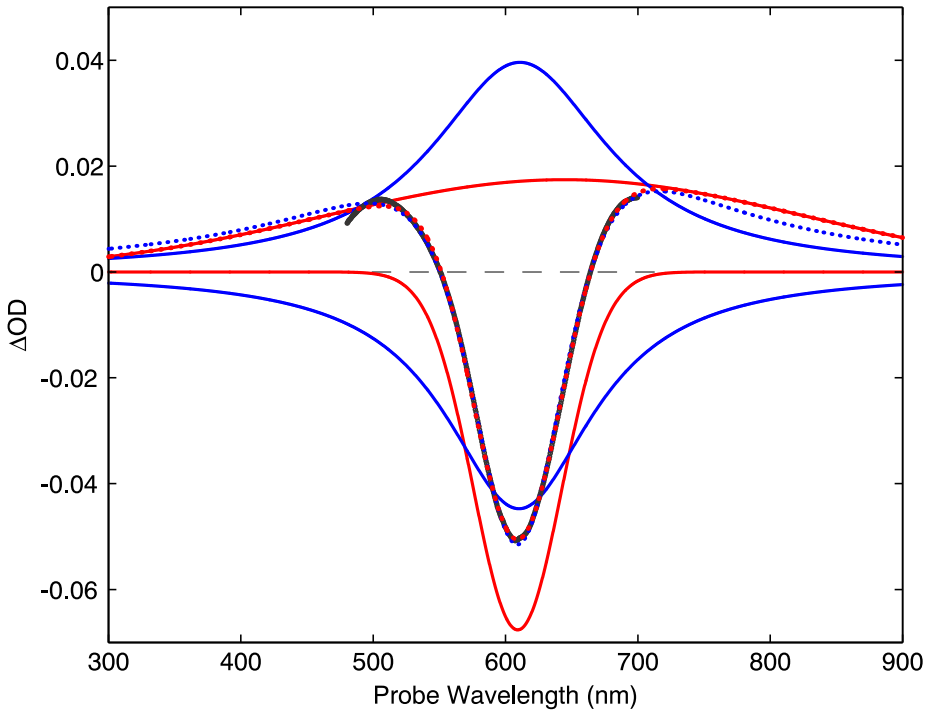

Figure 2.11: Sum of two Lorentzian line shapes (blue dotted line) and two Gaussians (red dotted line) to the data as shown in Figure 2.9 at 1 ps (black solid line). The solid blue and red lines show the two Lorentzians and Gaussians respectively. The two Lorentzian line shapes have been reduced by a factor or 10 for clarity.

The observed ~50 ps oscillations have been well studied for bare HGN samples.[26,29,43,44] As mentioned in (7) of the above list, they are due to breathing mode oscillations of the HGNS (periodic particle expansion and contraction). The rapid heating of the phonon population occurs on a timescale faster than the characteristic timescale of these oscillations. This impulsive heating causes the particle to rapidly expand, before contracting due to the elasticity of the particle providing a restoring force, hence harmonic oscillatory breathing modes are launched. The equilibrium position of these oscillations is about the diameter of the hot particle (which is larger in diameter than the particle at room temperature).[61] This periodic change in the size of the particle modulates the particles' electron density, which in turn periodically shifts the position and width of the LSPR, hence creating the observed oscillations in the kinetics and spectral features' peak positions.[26,43,56] Single nanoparticle studies have shown that such acoustic mode oscillations can be long-lived, lasting for over 750 ps in bipyramidal gold nanoparticles[62] and over 1 ns in gold nanorods.[63] However, the oscillations decay more rapidly in the (ensemble measurement) data reported here, which is likely to be due to ensemble dephasing resulting from the polydispersity of the samples.[61,62,64,65]

In order to extract the frequency of the breathing mode oscillations in my data, the data were interpolated along the time domain to create evenly spaced data points. Data at time points earlier than 10 ps were removed to eliminate the effects of the slow rise kinetics, then the kinetic data at each probe wavelength were fit to a biexponential decay. The biexponential fits were then subtracted from the original data, to generate a dataset comprised purely from coherent breathing mode oscillations, as shown in Figure 2.12 (a) and (b). In this resulting data, it is apparent that the oscillations on either side of the GSB/SE feature are out of phase, this is because the breathing mode oscillations cause the ESA to shift back and forth in wavelength about a central (nodal) position. As the HGN cools the plasmon moves to shorter wavelengths so the nodal position red-shifts. The time domain data were then apodized with a Tukey window and zero padded before being Fourier transformed along the time axis (Figure 2.12(c)). The maxima of the relevant oscillation were located (signals at low frequencies resulting from instrumental noise were discounted). As shown in Figure 2.12(d), 10 data points either side of the maxima (probe wavelength 656 nm) were averaged and the peak was taken as the average breathing mode frequency of the sample.

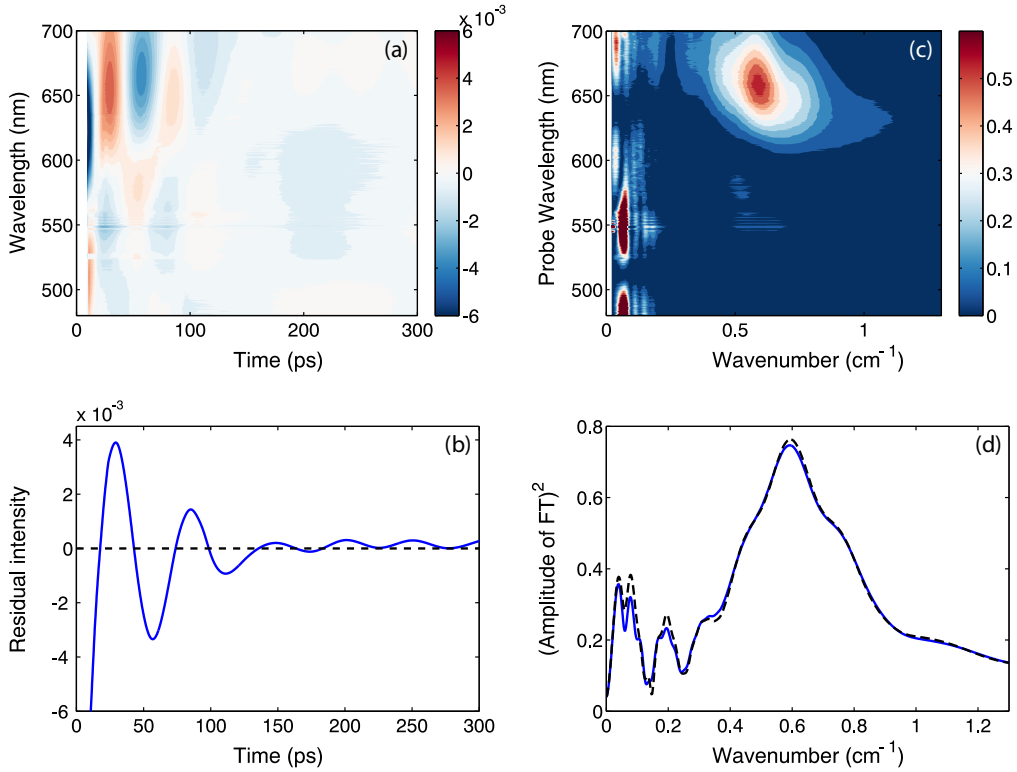

Figure 2.12: (a) Coherent phonon response of HGNs between 20–300 ps, extracted from TA spectra by subtraction of biexponential population decay fit (b) Kinetics associated with probe 656 nm, (c) Fourier transform (see text for details) of (a), (d) slice of (c) at probe wavelength = 656 nm (black dashed line) and average over 20 pixel (blue line).

The breathing mode frequencies returned from this analysis ranged from 0.59 – 0.62 cm^{-1} for the different datasets which corresponds to periods of 53.7 – 56.5 ps, which is in a range that is consistent with prior studies of HGNs breathing modes.[43] My studies also showed that the breathing mode period exhibits a power dependence (see Figure 2.13). SGN studies have explored the power dependence of the phonon frequencies, however, to the best of my knowledge, this is the first time such an effect has been observed for HGNs. The effect can be attributed to a softening (lower spring constant) of the metal at higher temperatures resulting in a reduced frequency, so that higher powers result in longer oscillatory periods.

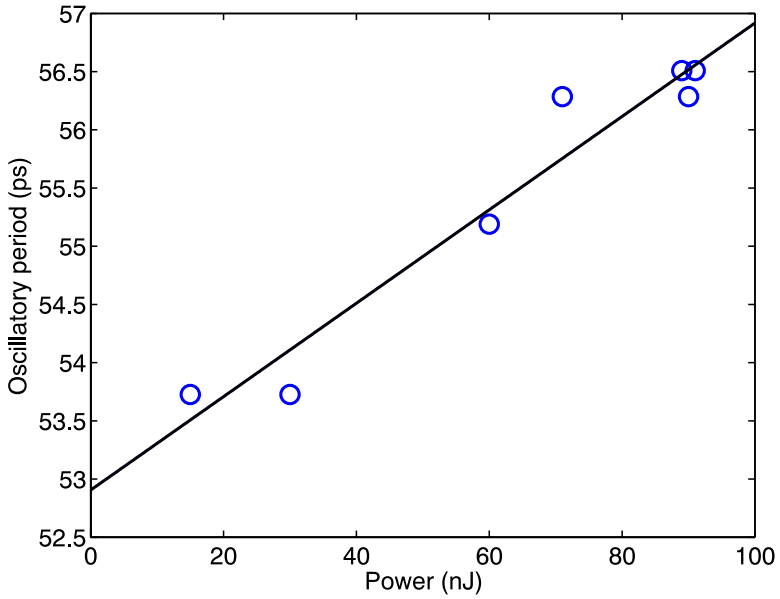

Figure 2.13: Power dependent oscillatory period of HGNs.

As expected from previous studies of HGNs, the population decay kinetics (neglecting the slow rise and breathing mode effects), depend strongly on the pump power, with the lifetimes greatly extended for higher pump powers. As can be seen in Figure 2.14, at low powers (15 μW) the features largely rise and fall in unison, which would be expected for a GSB/SE and overlapping ESA arising from the same hot electron population. However, at high powers (91 μW) the low energy ESA (monitored at 680 nm) exhibits very different kinetics, becoming negative at late time. Given the clear power dependence of this effect, I attribute it to an increased blue-shift of the ESA/new LSPR position at higher temperatures, as was proposed by Wiederrecht *et al.* for SGNs.[66]

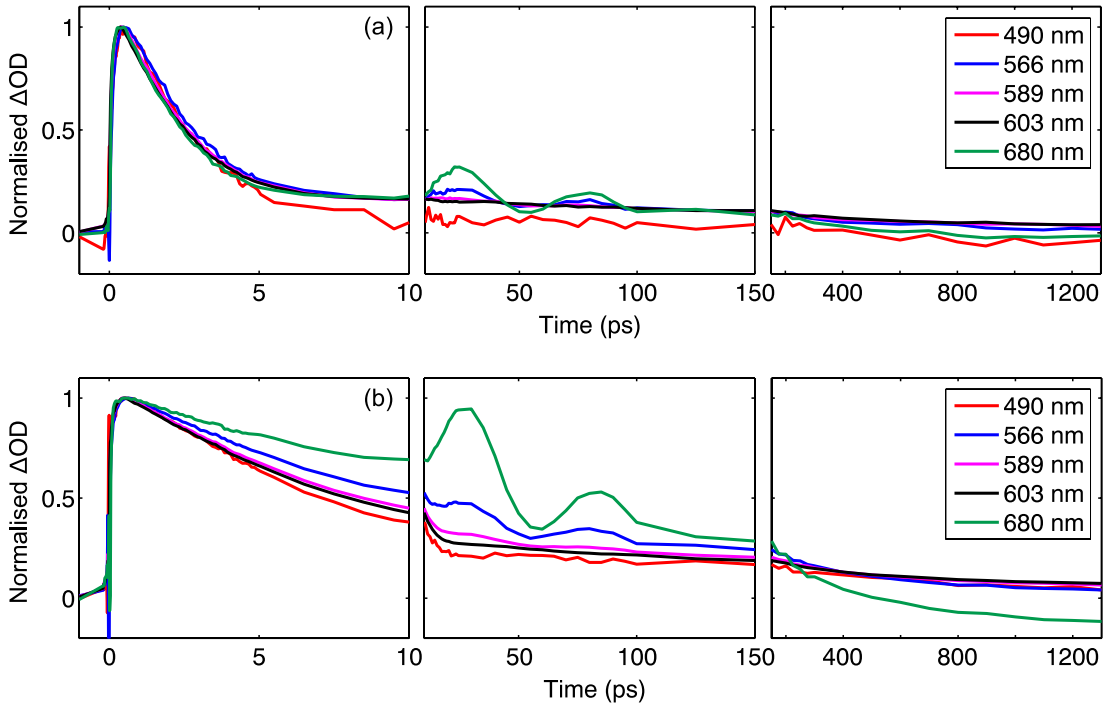

Figure 2.14: Normalised kinetics of HGNs at different probe wavelengths (as indicated) following a 15 μW (a) and 91 μW (b) pump pulse excitation

The GSB/SE kinetics can be fit to biexponential decays (See Figure 2.15 (a) for the fits at different pump powers) by excluding the first 0.6 ps to remove the effects of the slow rise in early time. At lower powers the data fit well to a biexponential decay, but at higher powers data at > 200 ps deviate significantly from the fit. Potentially this could indicate the existence of a third longer-lived component that only becomes significant at higher powers due to the longer-lived population.

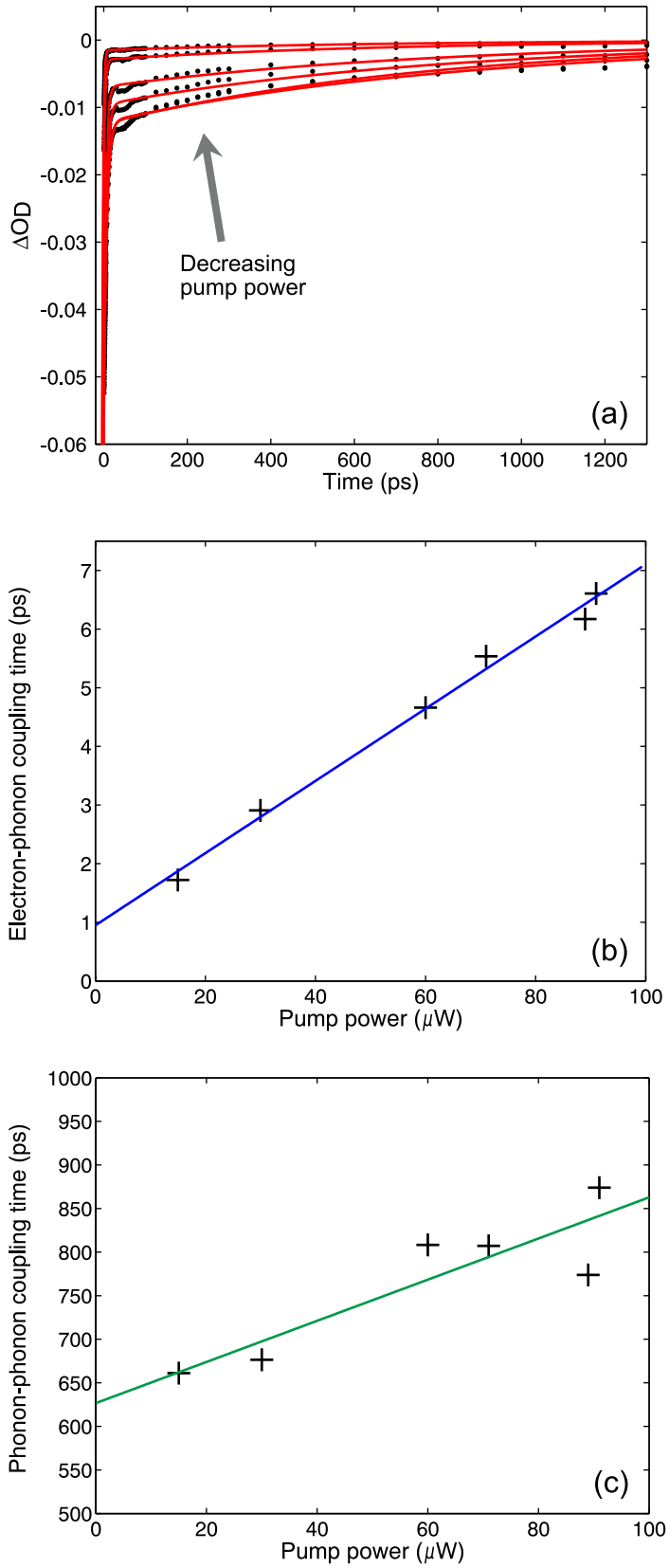

Figure 2.15: (a) Biexponential fits (red line) to GSB/SE kinetic data (blue points) at 607 nm at various pump pulse powers (excludes data at < 0.6 ps) for HGN sample. (b) Resulting electron-phonon coupling, and (c) Phonon-phonon coupling, time constants with linear fits

The biexponential fits to the data return time constants on the order of picoseconds (2–7 ps range) and hundreds of picoseconds (600–900 ps range). In literature these two timescales are typically associated with electron-phonon scattering and phonon-phonon scattering respectively. [3,44] Electron-phonon coupling is the primary route for the hot electron population to cool, transferring energy to the metal lattice. The effective temperature associated with the electron population is dependent on the pump power intensity, which in turn means the electron-phonon coupling rate also displays a similar power dependency. Fitting the electron-phonon time constants to a straight line, and extrapolating to zero pump power, gives a measure of the electron-phonon scattering rate at room temperature. As shown in Figure 2.15(b) this method gives a value of 1.4 ± 0.5 ps, which is comparable with values observed in prior HGN studies, depending on the HGN dimensions. [44] A power dependence to the phonon-phonon coupling time constant has been predicted in SGN studies. [67] Although prior HGN studies did not observe a correlation in this factor, the data presented here shows a weak power dependence (Figure 2.15(c)).

2.3.3.3. Hollow Gold Nanoparticles with J-aggregates on the Outer Surface (J_SHGN)

The effect of J-aggregate excitons coupling to the HGN LSPR is immediately obvious from the TA spectra displayed in Figure 2.16. The bleach feature is spectrally shifted and split into two at all time delays investigated. In literature describing SGN studies,[68] it is conventional to refer to the parts of the bleach on the low and high energy sides of the splitting as the lower polariton branch (LPB) and the upper polariton branch (UPB) respectively. However, I consider this nomenclature to be misleading for reasons that shall be discussed later in this chapter, so will primarily refer to these features by the wavelengths at which they occur (~603 nm and ~566 nm). Consistent with the linear absorption spectra, the divide between the 566 nm & 603 nm transient features is observed at a longer wavelength compared to the J-aggregate transient ESA feature (see section 2.3.3.1) and the linear absorption spectrum peak observed for the J-aggregates in solution. However, the position of the divide shifts from 595 ± 1 nm at early times (0.1 ps) to 590 ± 1 nm at late times (1 ns).

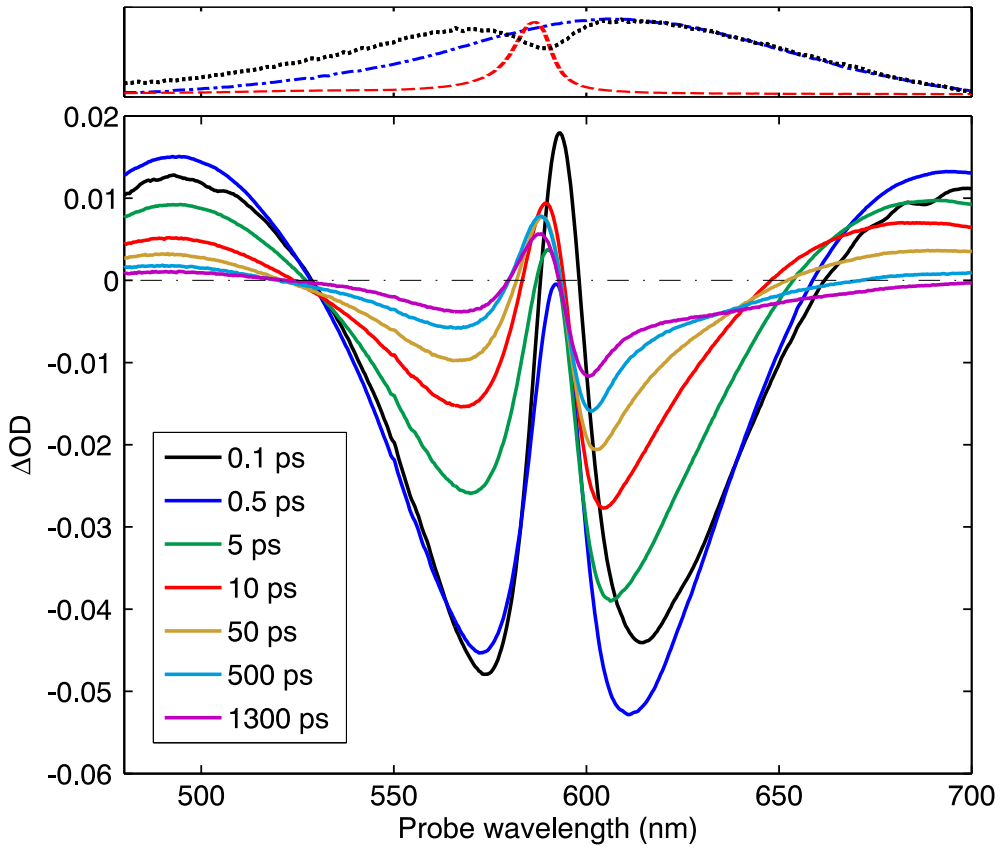

Figure 2.16: TA spectra of J_SHGNs at the indicated pump-probe delay times, acquired with 125 μW pump pulses. Upper panel shows linear spectra of the J_SHGN (black dotted line), J-aggregate (red dashed line), and HGN (blue dash-dot line) samples for line-shape reference.

Figure 2.17 shows the normalised kinetics associated with the 566 nm, 603 nm, divide, and two ESA features. As was the case for the HGNs samples, it is likely that these kinetics result from the rise and decay of overlapping features. Oscillations due to the HGNs breathing modes are again visible in the 603 nm feature and lower energy ESA (680 nm) kinetics. The breathing mode time period of this sample with a 125 μW pump was found to be 64.7 ps, far longer than found for HGNs on their own using the same pump power. However, in contrast to the HGN's TA data, in this data the kinetics associated with the features evolve at different rates and the signal is longer lived than either the HGNs or J-aggregates on their own. At early times the slow-rise in the intensity of the features (which I attributed to the dephasing of the plasmon and subsequent thermalisation of the hot electrons in section 2.3.3.2) is still present in this data.

The kinetics of the two ESAs (as illustrated by kinetic slices taken at probe wavelengths 490 nm and 680 nm in Figure 2.17) clearly show notably different population dynamics. It seems that the population that causes the 566 nm bleach/SE are also

responsible for the higher energy ESA, given that after the initial rise these features exhibit similar kinetics. The same is likely to be true for the 603 nm feature and the lower energy ESA, despite the fact that at late time delays their kinetics deviate significantly. This effect was also observed in the HGN sample (at higher pump powers) and I attributed this cooling in HGNs which induced a frequency shift in the ESA. The positive signal at the divide between the 566 nm & 603 nm features (~589 nm) is somewhat surprising since it could not result from simply splitting into two separate polariton branches. It could instead occur due to the reduced intensity of the bleach at this wavelength allowing the signal from an ESA feature to preponderate.

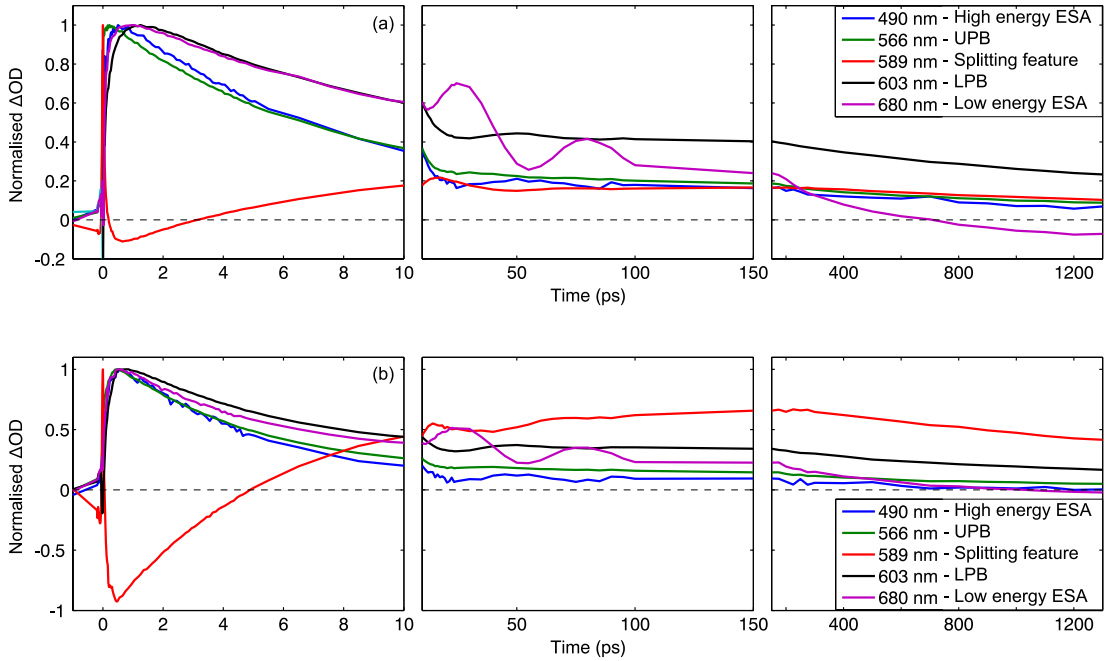

Figure 2.17: Normalised kinetics of J_SHGNs at different probe wavelengths (as indicated) following a excitation with a (a) 125 μW pump pulse, and (b) a pump pulse with a spectrum limited a 600 nm long-pass filter.

A comparison of selectively exciting the sample at different wavelengths is shown in Figure 2.18 and provided further crucial insights into the J-aggregate HGNs hybrid. At first sight Figure 2.18 may give the impression that the time-resolved spectral line shapes vary significantly depending on the excitation frequency, but it is important to recognise that changing the spectral range of the pump pulse also impacted the excitation power, and therefore a careful distinction must be made between effects of the excitation wavelength and the excitation power (see the next section for further discussion). Instead, the key observation from Figure 2.18 is that no matter at which wavelength the sample is excited both the 566 nm & 603 nm features bleach.

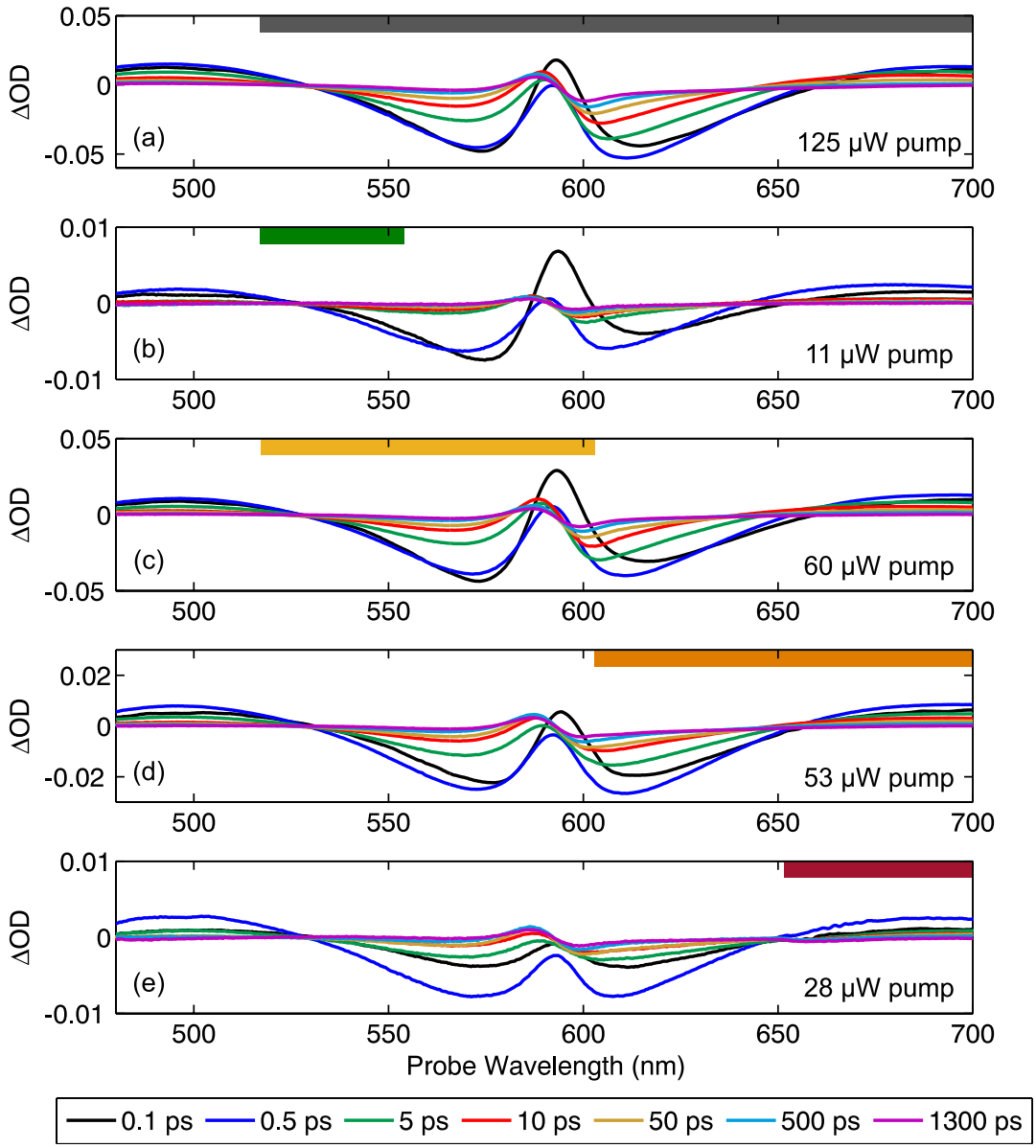

Figure 2.18: TA response of J_SHGNs following excitation with different wavelength (and power) pump pulses, as indicated by the coloured bars at the top of each plot: (a) full pump spectrum, (b) <550 nm, (c) <600 nm, (d) >600 nm, and (e) >650 nm.

The immediate splitting response can be explained if the pump (at any of the wavelength ranges used) excites the plasmon, which in turn evanescently excites and couples immediately (within the pump excitation) to the J-aggregates, and thus induces a splitting of the bleach. Note that I rule out dipole-coupling between the HGN and J-aggregate prior to photoexcitation because the HGN in the valence band has no overall dipole moment. This coupling of the HGNs and J-aggregates must occur on a timescale faster than the IRF and the plasmon dephasing timescale (~10 fs). This interpretation agrees with the finding of Wiederrecht and co-workers for SGNs. [15]

The relatively short-lived ESA which is apparent at very early time delays (< 0.2 ps) between the 566 nm and 603 nm features is dependent on the pump excitation wavelength, and entirely absent from data using λ > 650 nm excitation (Figure 2.18(e)). This is an important finding, as prior J_SHGN TA studies did not include a thorough wavelength dependence.[42] Recalling the linear absorption spectrum of the J-aggregates in solution (Figure 2.7(a)) and the laser spectra with and without long/short pass filters (Figure 2.5); with the 600 nm long pass filter applied, the pump is capable of exciting the long wavelength tail of the J-aggregate absorption spectrum, whereas the pump spectrum limited by the 650 nm long pass filter is not. Therefore, for panels (a-d) in Figure 2.18, it is possible to excite either the LSPR associated with the HGN or the J-aggregates directly (assuming they are uncoupled in the ground state). In these measurements any J-aggregates on the surface of the HGNs that were unable to couple to the gold NP LSPR would also have been excited. Therefore, for TA experiments with pump excitation at < 650 nm, I would expect to see signatures of direct J-aggregate excitation*, e.g.* dispersive GSB/SE and 2-exciton ESA (see Figure 2.8(a)), festooned on top of signal from LSPRs coupled to the bound J-aggregates. Note that the TA spectra of these J-aggregates will depend on the precise local environment of the excitonic species, which has been reported to change slightly when tethered to metallic surfaces. [69] Figure 2.18(e) is therefore the only TA spectrum in this dataset, and not previously reported in the literature, which contains spectral signatures of only the J_SHGN hybrid system.

For all the datasets presented above, the kinetics of the 566 nm feature fit well to a biexponential decay (excluding the first 1.5 ps), as did the kinetics associated with the 603 nm feature, (first 2 ps excluded from the fit). These fits are shown in Figure 2.19 and summarised in Table 2.5. When the sample was excited by pump pulses with shorter wavelengths the ground state bleach recovery took longer. However, since the absorption of the sample varies with wavelength, the excitation powers used with different pump wavelengths cannot be directly compared as a measure of excitation energy, therefore only general trends associated with excitation power can be ascertained from these data.

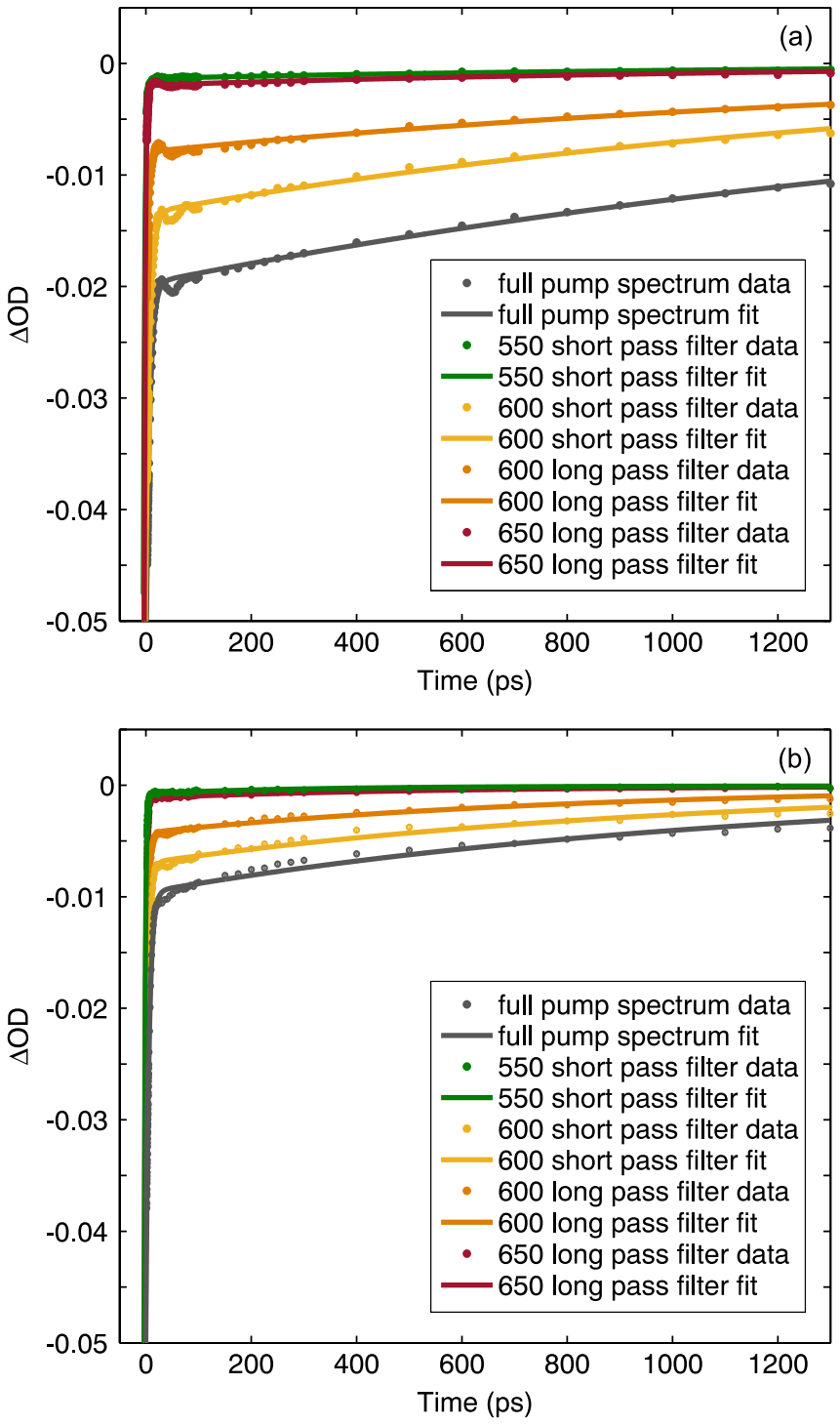

Figure 2.19: Biexponential fits to the 603 nm feature (a), and the 566 nm feature (b), for JSHGNs following excitation with different wavelength (and power) pump pulses, as indicated.

The time constants returned from these fits are given in Table 2.5, and show that the amplitude of each component does not show any clear correlation with the excitation wavelength. However, there is an apparent general trend of higher excitation powers

resulting in greater amplitudes associated with the long-lived components. There is also a general trend of higher excitation powers resulting in larger time constants. Both of these effects were observed for the bare HGNs sample.

The shorter lifetime components decay on a timescale consistent with that of the electron-phonon scattering observed in the uncoupled HGN samples (between 2–7 ps). The larger time constants differ significantly between the 566 nm and 603 nm features' kinetics, with the 566 nm component being much shorter. The possibly of population transfer from the 566 nm feature to the 603 nm feature was investigated by attempting to fit the 603 nm feature's kinetics with a three-part exponential, where one component was a positive rise to capture an increase in population upon relaxation from the 566 nm feature. This analysis did not give an improved fit compared to the biexponential function.

Table 2.5: Time constants and corresponding amplitude components from biexponential fits to the 566 nm and 603 nm features in TA data of HGNs with J-aggregate on the outer surface. These data were taken with the pump spectrum modified by different filters and subsequently at different powers. Corresponding fits shown in Figure 2.19.

Pump laser spectrum	Power / μW	λ_{probe} / nm	τ_1 / ps	A_1 / %	τ_2 / ps	A_2 / %
Full pump spectrum	125	566	6.0 ± 0.2	79	1100 ± 100	21
		603	7.0 ± 0.3	64	2100 ± 200	36
550 nm short pass	11	566	2.02 ± 0.09	92	320 ± 90	8
		603	2.63 ± 0.09	84	1300 ± 100	16
600 nm short pass	53	566	4.9 ± 0.1	83	1000 ± 80	17
		603	7.3 ± 0.3	70	1600 ± 100	30
600 nm long pass	59	566	4.33 ± 0.08	84	840 ± 60	16
		603	4.7 ± 0.2	70	1700 ± 200	30
650 nm long pass	28	566	2.43 ± 0.06	91	560 ± 80	9
		603	2.2 ± 0.1	84	1300 ± 200	16

Given that the origin of the splitting phenomena observed in this sample has been attributed to plasmon-exciton coupling in prior SGN studies, and the two split features are assigned as UPB and LPBs, it is very surprising that the kinetics of this system still fit to a biexponential decay function, as per the uncoupled HGNs. I would have expected that at least three exponential components would be required to fit these data: two to represent the decay of the hot electron population that is excited by the decay of plasmons but do not couple to J-aggregate excitons, and at least one additional component to model the decay of the coupled system.

2.3.3.4. HGNs with J-aggregates in the Core and on the Outer Surface (J_CJ_SHGN)

Figure 2.20 displays the TA data recorded for J_CJ_SHGN samples under various excitation conditions. The TA spectra are broadly similar to the response of the J_SHGN samples, exhibiting positive features at the extremes of the probe window and a central bleach that is split in two by a feature that is positive at early pump-probe time delays. However as observed in the linear absorption spectra, the intensity of the divide between the 566 nm and 603 nm features is generally less pronounced than for the J_SHGN data, despite the fact that the J_CJ_SHGN particles have a higher density of J-aggregates to couple with: *e.g.* inside of HGN core and on the outer-shell.

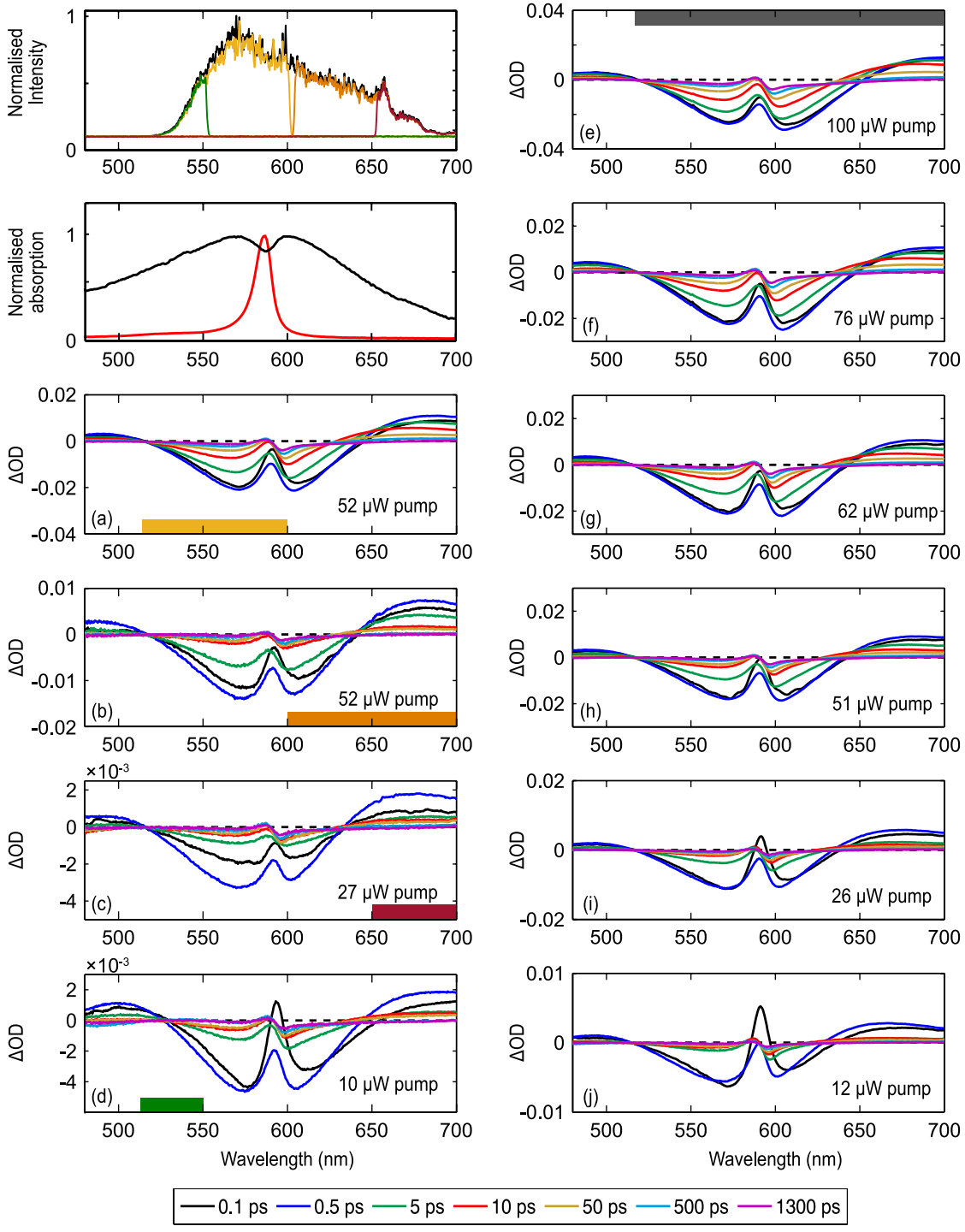

Figure 2.20: TA response of J_SJ_CHGNs at different pump wavelengths (a-d), as indicated and different pump powers: (e-j) with the full pump spectrum. Pump spectra with filters and linear absorption spectra of J_SJ_CHGNs (black) and J-aggregates (red) included for reference top left.

It is tempting to conclude a less pronounced splitting in the plasmon bleach feature is an indicator of weaker LSPR-exciton coupling. However, from the data acquired with the full pump NOPA spectrum, the apparent magnitude in the splitting depends on the pump excitation power (Figure 2.20(e-j)). It is clear that the dividing feature has a greater

intensity relative to the other features at lower pump powers. This is counterintuitive if the splitting solely arises from electronic coupling. The observation is more consistent with the total 'splitting' observed in the TA data arising from the J_SJ_CHGN particles and the overlapping J-aggregate ESA, and the latter saturates at higher pump powers. Although this J-aggregate ESA is at a different wavelength to the ESA of the J-aggregates in solution, as mentioned previously, the absorption spectra of dyes have been shown to change when on the surface of metallic nanoparticles. [69] Further, at late delay times (~1300 ps), the TA spectra of the hybrid are reminiscent of the J-aggregates TA spectra in solution at late delay times.

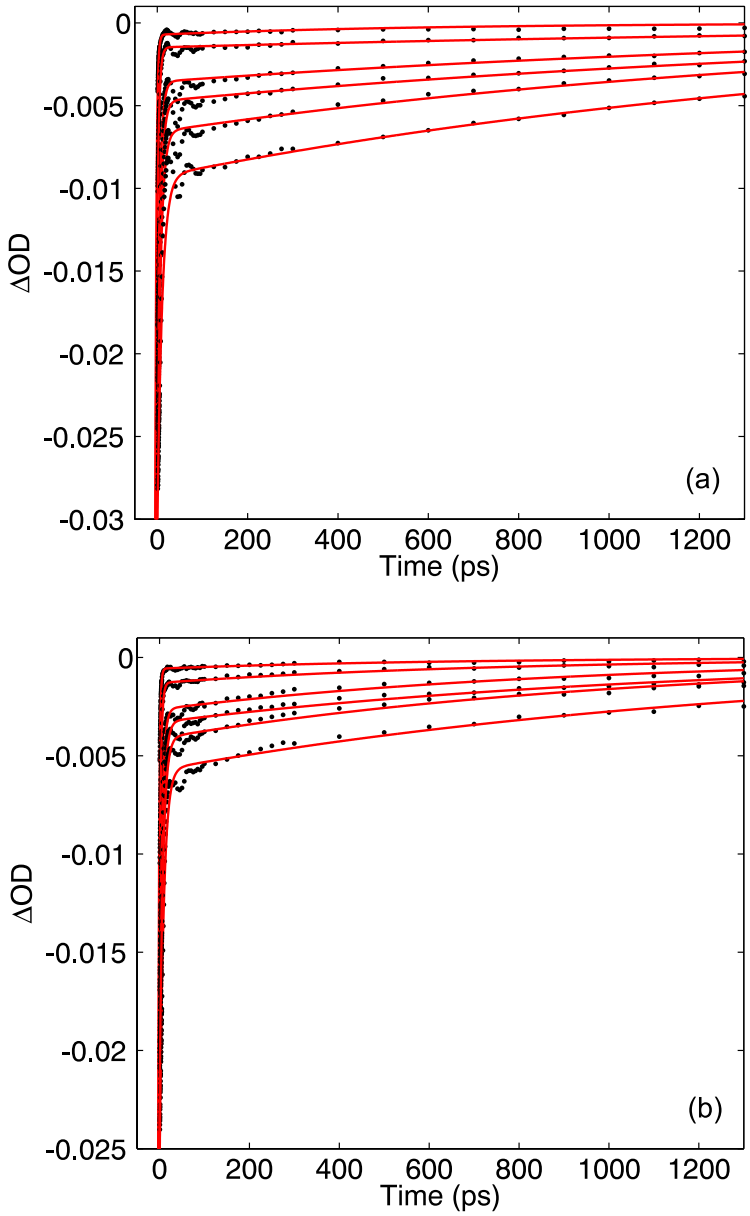

Figure 2.21: Biexponential fits to kinetics at probe wavelengths (a) 603 nm and (b) 566 nm for J_SJ_CHGNs at different pump powers. TA data displayed in Figure 2.20(e-j).

This assignment would also explain why this feature shows a slight excitation wavelength dependence. Comparing panels (c) and (i) of Figure 2.20, the sample was excited with similar pump excitation powers (27 and 26 μW, respectively) but different pump wavelengths: Figure 2.20(c) shows data acquired with pump wavelengths longer than 650 nm, whereas the data shown in Figure 2.20 (i) were acquired using the full NOPA pump spectrum. Due to the lower absorbance of the sample at wavelengths > 650 nm the actual energy imparted to the sample in dataset (c) is likely to be lower than that in (i), yet (counter to the observed power dependence trend) the splitting (or overlapping positive) feature is less intense. Again, as per the J_SHGN sample, > 650 nm excitation will not excite any 'free' J-aggregates, and the TA response will reflect that just of the hybrid J_SJ_CHGN system.

As observed in the J_SHGN data, the rise time of the features is dependent on the pump wavelength, with pump spectra including wavelengths longer than 550 nm resulting in different rise timescales associates with the features, the features all rise in unison for > 550 nm excitation. Therefore, this provides further evidence that the excitation wavelength dependence arises from excitation of gold interband transitions which are submerged under the LSPR in the linear absorption spectrum.

The kinetics of the features in this sample are similar to those observed for the other hybrid sample and HGN sample, in that following an initial rise the kinetics of the bleach features can be fit to biexponential decays (see Figure 2.21). Following the interpretation that the 'splitting' feature is in fact due to a J-aggreagte ESA, this consistent slow rise indicates that the plasmon is excited and dephases very quickly (~10fs, certainly within the IRF) in all samples. Such that the dynamics measured in these experiments result from the hot electron population creation and subsequent cooling. The contrast in the kinetics of the splitting/J-aggregate ESA feature compared to the kinetics of the J-aggregates in solution, suggests that the hot electron population can re-excite the J-aggregates in some way, slowing the decay of this feature. Whether this is through (phonon) heating or hot-electron transfer is unclear but warrants further investigation.

As was observed for J_SHGN samples, in all of the measurements of this sample the 603 nm feature lives longer than the 566 nm feature. However, when the normalised kinetics of the two hybrid samples are compared directly (see Figure 2.22) it is apparent that the kinetics of the 566 nm feature are consistent, but the kinetics of the 603 nm feature at t > 20 ps differ significantly between the two samples, and that the J_SHGN transient

signals are far longer lived. This is true even when comparing datasets acquired using a 650 nm short pass filter such that neither the J-aggregate nor gold interband transitions are (directly) excited.

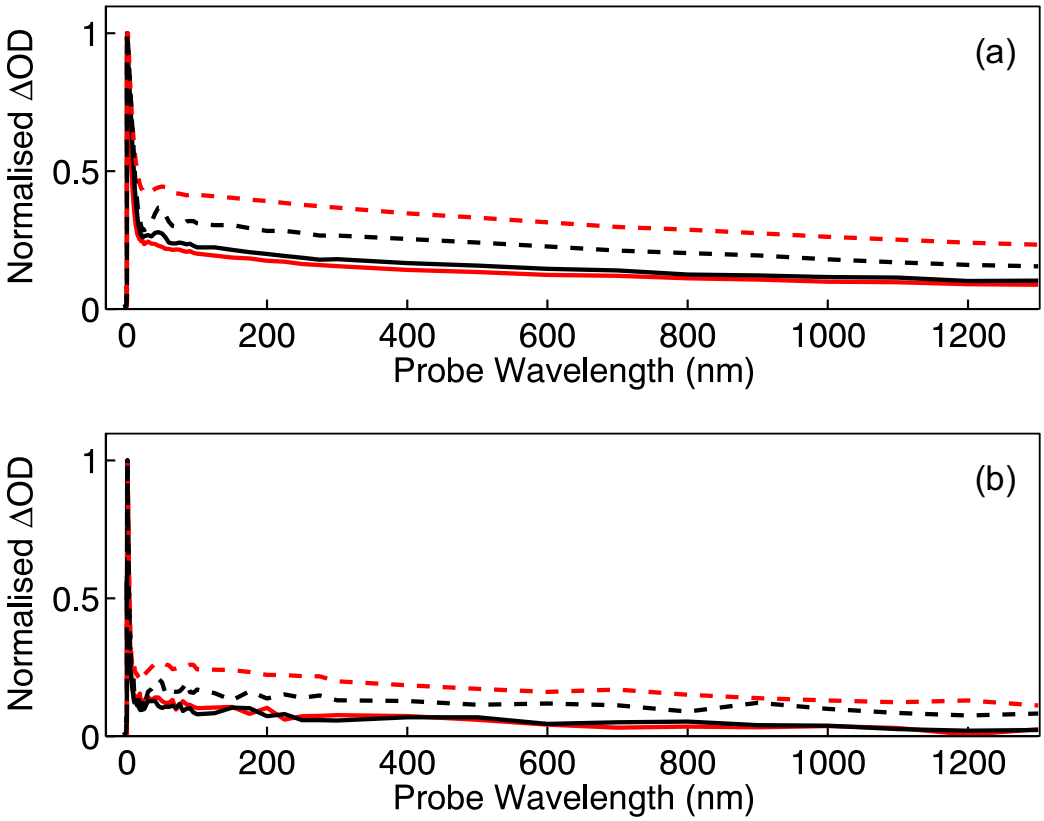

Figure 2.22: kinetics of the 566 nm (solid lines) and 603 nm (dashed) features following excitation with the full pump spectrum (a), and the pump limited to wavelengths greater than 650 nm (b), for J_SJ_CHGN (black line) and J_SHGN (red lines) samples.

The shortest time constants returned from fitting these data are plotted in Figure 2.23 as a function of pump excitation power and display a linear relationship, similar to that observed for the HGNs without J-aggregates. The shorter time constants are fairly consistent between the 566 nm and the 603 nm features. However, for the longer time constants there is a clear discrepancy between the power dependence of the 603 nm feature and the 566 nm feature. The 566 nm feature exhibits a linear power dependence, with the time constant increasing with pump power, as per the HGN data. In contrast, the power dependence of the 603 nm feature phonon-phonon coupling time constant is clearly not linear, but the reason for this observation is unclear.

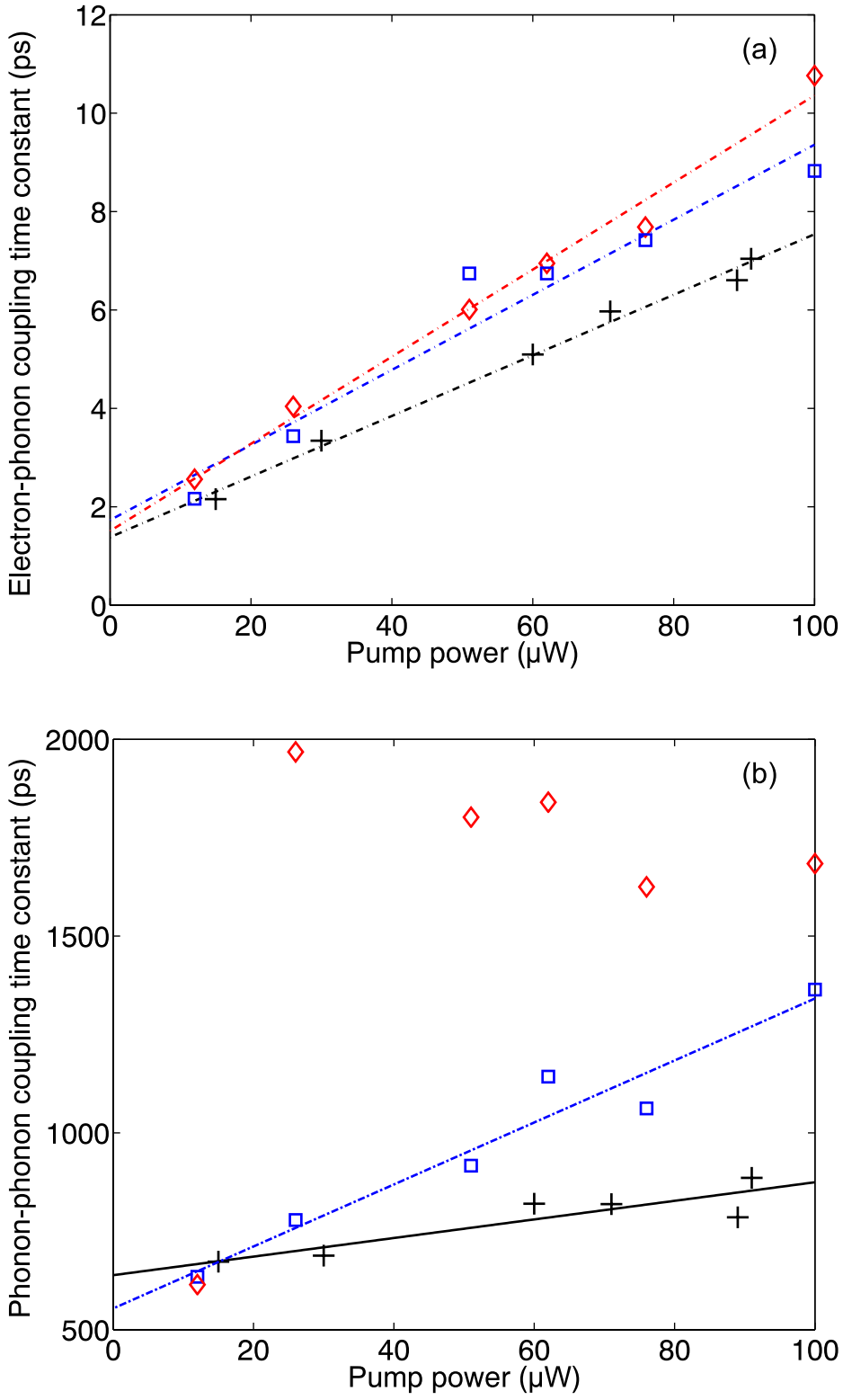

Figure 2.23: Power dependence of (a) electron-phonon and (b) phonon-phonon time constants extracted from biexponential fits to $J_S J_C$HGNs monitored at the 566 nm feature (blue) and the 603 nm feature (red), with linear fits. HGNs (black) data included for reference.

2.4. Conclusions and Future Work

In this chapter, the transient response of hybrid systems consisting of hollow gold nanoshells and TDBC J-aggregates was investigated. TA measurements were performed on HGNs with TDBC J-aggregates on the outer surface, inner surface, and both surfaces. As far as I am aware, this study is the first to investigate the transient response of HGNs with J-aggregates inside them.

Time-resolved measurements of the HGNs alone revealed a broad bleach feature flanked by ESA features, attributed to bleach from the LSPR excited by the pump with a broader and overlapping ESA feature from the excited state LSPR. These overlapping features exhibited complex dynamics. The data exhibits a power independent slow rise in the first ~0.5 ps, which is characteristic of plasmons dephasing within the IRF (expected to be ~10 fs from SGN studies), followed by the resulting hot electron population thermalising through electron-electron scattering. The ensuing decay in signal results from electron-phonon and phonon-phonon coupling allowing the HGN electron population to cool. I determined for the first time, the power dependent phonon breathing modes of HGNs.

In terms of the coupling strength between the J-aggregates and the HGNs, it was observed from the linear absorption spectra that the splitting effect due to J-aggregates on the inner surface of the HGN was generally weaker than in hybrids with HGNs on the outer surface of the HGNs. Theoretical studies have predicted that the optically active LSPR of HGNs is actually a hybrid mode between the LSPRs of the inner and outer surfaces of the nanoshell, which is closer in energy to the outer surface LSPR. Therefore, the weaker response from J-aggregates may be due to the optically active mode being more strongly associated with the outer surface of the HGN. However, this will require further studies to investigate, with carefully controlled shell thicknesses of the HGNs and tuning of the LSPR to give a variety of coupling strengths.

The transient studies of HGNs with J-aggregates outside (J_SHGN), or both inside and outside (J_SJ_CHGN) revealed insights into the system studied, and the pump excitation wavelength dependence proved crucial in distinguishing the effects of overlapping features. As was observed for the uncoupled HGNs, the transient data exhibited a slow rise at early time. In addition, the decay of the transient signal occurred with time constants that were largely consistent between the coupled and uncoupled systems. Based on these similarities, it is clear that, as for the uncoupled HGNs, the plasmons in the hybrid system dephase quickly (~10fs) and within this period couple to the J-aggregate excitons giving

rise to the apparent splitting of the associated bleach features. In the samples studied here any differences in the kinetics of the samples with J-aggregates seems to stem from a decrease in the phonon-phonon coupling rate which may be due to the layer of J-aggregates on the outer surface of the HGN acting as an insulating layer, slowing the cooling of the HGN. Comparison of the kinetics of a sample exhibiting coupling but with J-aggregates on the inside of the HGN only may allow this to be investigate further in future studies.

Interpreting this data is hindered by the number of overlapping features, the shifting of the LSPR with heating and particle breathing modes, and the possibility of the spectral frequencies of the J-aggregate occurring at different frequencies when adsorbed to the metal than when in solution.[69] Therefore this work could benefit greatly from computational modelling and 2-dimensional electron spectroscopy measurements to resolve the overlapping transient features and frequency resolve the pump excitation dependence. Future work should also include repeating TA measurements of samples of HGN with J-aggregates only contained within the hollow cavity, to further investigate the effects of positioning the J-aggregates inside, rather than on the surface of the HGNs. Finally, performing similar measurements to these on a range of HGN samples with a variety of sizes and shell thicknesses would allow the effects of detuning the LSPR resonance and, potentially, a variety of coupling strengths to be systematically investigated and provide fundamental insights.

References

(1) Louis, C.; Pluchery, O. *Gold Nanoparticles for Physics, Chemistry and Biology*, 1st ed.; Imperial College Press: Singapore, United States, 2012; pp 1–5.

(2) Jennings, T.; Strouse, G. Past, Present, and Future of Gold Nanoparticles. In *Bio-Applications of Nanoparticles*; Bio-Applications of Nanoparticles; Springer, New York, NY: New York, NY, 2007; Vol. 620, pp 34–47.

(3) Amendola, V.; Pilot, R.; Frasconi, M.; Maragò, O. M.; Iatì, M. A. Surface Plasmon Resonance in Gold Nanoparticles: a Review. *J. Phys.: Condens. Matter* **2017**, *29* (20), 203002–203049.

(4) Faraday, M. X. the Bakerian Lecture.—Experimental Relations of Gold (and Other Metals) to Light. *Phil. Trans. R. Soc.* **1857**, *147*, 145–181.

(5) Hertzog, M.; Wang, M.; Mony, J.; Börjesson, K. Strong Light–Matter Interactions: a New Direction Within Chemistry. *Chem. Soc. Rev.* **2019**, *48* (3), 937–961.

(6) Hartland, G. V. Optical Studies of Dynamics in Noble Metal Nanostructures. *Chem. Rev.* **2011**, *111* (6), 3858–3887.

(7) Li, X.; Choy, W. C. H.; Lu, H.; Sha, W. E. I.; Ho, A. H. P. Efficiency Enhancement of Organic Solar Cells by Using Shape-Dependent Broadband Plasmonic Absorption in Metallic Nanoparticles. *Adv. Funct. Mater.* **2013**, *23* (21), 2728–2735.

(8) Maye, M. M.; Luo, J.; Lim, I.-I. S.; Han, L.; Kariuki, N. N.; Rabinovich, D.; Liu; Zhong, C.-J. Size-Controlled Assembly of Gold Nanoparticles Induced by a Tridentate Thioether Ligand. *J. Am. Chem. Soc.* **2003**, *125* (33), 9906–9907.
(9) Chikkaraddy, R.; de Nijs, B.; Benz, F.; Barrow, S. J.; Scherman, O. A.; Rosta, E.; Demetriadou, A.; Fox, P.; Hess, O.; Baumberg, J. J. Single-Molecule Strong Coupling at Room Temperature in Plasmonic Nanocavities. *Nature* **2016**, *535* (7610), 127–130.
(10) Yao, J.; Yang, M.; Duan, Y. Chemistry, Biology, and Medicine of Fluorescent Nanomaterials and Related Systems: New Insights Into Biosensing, Bioimaging, Genomics, Diagnostics, and Therapy. *Chem. Rev.* **2014**, *114* (12), 6130–6178.
(11) Ogarev, V. A.; Rudoi, V. M.; Dement'eva, O. V. Gold Nanoparticles: Synthesis, Optical Properties, and Application. *Inorg. Mater. Appl. Res.* **2018**, *9* (1), 134–140.
(12) Agrawal, A.; Cho, S. H.; Zandi, O.; Ghosh, S.; Johns, R. W.; Milliron, D. J. Localized Surface Plasmon Resonance in Semiconductor Nanocrystals. *Chem. Rev.* **2018**, *118* (6), 3121–3207.
(13) Fox, M. *Optical Propertied of Solids*, Second Edition. Oxford University Press, 2010.
(14) Törmä, P.; Barnes, W. L. Strong Coupling Between Surface Plasmon Polaritons and Emitters: a Review. *Rep. Prog. Phys.* **2014**, *78* (1), 013901–013935.
(15) Wiederrecht, G. P.; Wurtz, G. A.; Bouhelier, A. Ultrafast Hybrid Plasmonics. *Chemical Physics Letters* **2008**, *461* (4-6), 171–179.
(16) Hutter, E.; Fendler, J. H. Exploitation of Localized Surface Plasmon Resonance. *Adv. Mater.* **2004**, *16* (19), 1685–1706.
(17) Krasnok, A. E.; Slobozhanyuk, A. P.; Simovski, C. R.; Tretyakov, S. A.; Poddubny, A. N.; Miroshnichenko, A. E.; Kivshar, Y. S.; Belov, P. A. An Antenna Model for the Purcell Effect. *Sci. Rep.* **2015**, *5* (12956), 1–16.
(18) Stiles, P. L.; Dieringer, J. A.; Shah, N. C.; Van Duyne, R. P. Surface-Enhanced Raman Spectroscopy. *Annual Rev. Anal. Chem.* **2008**, *1* (1), 601–626.
(19) Aslan, K.; Wu, M.; Lakowicz, J. R.; Geddes, C. D. Fluorescent Core−Shell Ag@SiO2 Nanocomposites for Metal-Enhanced Fluorescence and Single Nanoparticle Sensing Platforms. *J. Am. Chem. Soc.* **2007**, *129* (6), 1524–1525.
(20) Skrabalak, S. E.; Chen, J.; Sun, Y.; Lu, X.; Au, L.; Cobley, C. M.; Xia, Y. Gold Nanocages: Synthesis, Properties, and Applications. *Acc. Chem. Res.* **2008**, *41* (12), 1587–1595.
(21) Ringe, E.; McMahon, J. M.; Sohn, K.; Cobley, C.; Xia, Y.; Huang, J.; Schatz, G. C.; Marks, L. D.; Van Duyne, R. P. Unraveling the Effects of Size, Composition, and Substrate on the Localized Surface Plasmon Resonance Frequencies of Gold and Silver Nanocubes: a Systematic Single-Particle Approach. *J. Phys. Chem. C* **2010**, *114* (29), 12511–12516.
(22) Cao, J.; Sun, T.; Grattan, K. T. V. Gold Nanorod-Based Localized Surface Plasmon Resonance Biosensors: a Review. *Sens. Actuators: B. Chem.* **2014**, *195*, 332–351.
(23) Scarabelli, L.; Coronado-Puchau, M.; Giner-Casares, J. J.; Langer, J.; Liz-Marzán, L. M. Monodisperse Gold Nanotriangles: Size Control, Large-Scale Self-Assembly, and Performance in Surface-Enhanced Raman Scattering. *ACS Nano* **2014**, *8* (6), 5833–5842.

(24) Barbillon, G.; Bijeon, J. L.; Plain, J.; Royer, P. Sensitive Detection of Biological Species Through Localized Surface-Plasmon Resonance on Gold Nanodisks. *Thin Solid Films* **2009**, *517* (9), 2997–3000.
(25) Prevo, B. G.; Esakoff, S. A.; Mikhailovsky, A.; Zasadzinski, J. A. Scalable Routes to Gold Nanoshells with Tunable Sizes and Response to Near-Infrared Pulsed-Laser Irradiation. *Small* **2008**, *4* (8), 1183–1195.
(26) Newhouse, R. J.; Wang, H.; Hensel, J. K.; Wheeler, D. A.; Zou, S.; Zhang, J. Z. Coherent Vibrational Oscillations of Hollow Gold Nanospheres. *J. Phys. Chem. Lett.* **2011**, *2* (3), 228–235.
(27) Sun, L.; Li, Z.; He, J.; Wang, P. Strong Coupling with Directional Absorption Features of Ag@Au Hollow Nanoshell/J-Aggregate Heterostructures. *Nanophotonics* **2019**, *8* (10), 1835–1845.
(28) Chandra, M.; Dowgiallo, A.-M.; Knappenberger, K. L., Jr. Controlled Plasmon Resonance Properties of Hollow Gold Nanosphere Aggregates. *J. Am. Chem. Soc.* **2010**, *132* (44), 15782–15789.
(29) Adams, S.; Zhang, J. Z. Unique Optical Properties and Applications of Hollow Gold Nanospheres (HGNs). *Coord. Chem. Rev.* **2016**, *320-321*, 18–37.
(30) Prodan, E.; Nordlander, P. Plasmon Hybridization in Spherical Nanoparticles. *J. Phys. Chem.* **2004**, *120* (11), 5444–5454.
(31) Wang, H.; Brandl, D. W.; Nordlander, P.; Halas, N. J. Plasmonic Nanostructures: Artificial Molecules. *Acc. Chem. Res.* **2007**, *40* (1), 53–62.
(32) Jelley, E. E. Molecular, Nematic and Crystal States of I: I-Diethyl--Cyanine Chloride. *Nature* **1937**, *139* (3519), 631–631.
(33) Würthner, F.; Kaiser, T. E.; Saha-Möller, C. R. J-Aggregates: From Serendipitous Discovery to Supramolecular Engineering of Functional Dye Materials. *Angew. Chem. Int. Ed.* **2011**, *50* (15), 3376–3410.
(34) van Burgel, M.; Wiersma, D. A.; Duppen, K. The Dynamics of One-Dimensional Excitons in Liquids. *J. Phys. Chem.* **1995**, *102* (1), 20–33.
(35) Hamm, P.; Zanni, M. *Concepts and Methods of 2D Infrared Spectroscopy*; Cambridge University Press, 2011.
(36) Antosiewicz, T. J.; Apell, S. P.; Shegai, T. Plasmon–Exciton Interactions in a Core–Shell Geometry: From Enhanced Absorption to Strong Coupling. *ACS Photonics* **2014**, *1* (5), 454–463.
(37) Auguié, B.; Le Ru, E. C. Optical Absorption of Dye Molecules in a Spherical Shell Geometry. *J. Phys. Chem. C* **2018**, *122* (33), 19110–19115.
(38) Fano, U. Effects of Configuration Interaction on Intensities and Phase Shifts. *Physical Review* **1961**, *124* (6), 1866–1878.
(39) Limonov, M. F.; Rybin, M. V.; Poddubny, A. N.; Kivshar, Y. S. Fano Resonances in Photonics. *Nat. Photonics* **2017**, *11* (9), 543–554.
(40) Wang, H.; Toma, A.; Wang, H.-Y.; Bozzola, A.; Miele, E.; Haddadpour, A.; Veronis, G.; De Angelis, F.; Wang, L.; Chen, Q.-D.; et al. The Role of Rabi Splitting Tuning in the Dynamics of Strongly Coupled J-Aggregates and Surface Plasmon Polaritons in Nanohole Arrays. *Nanoscale* **2016**, *8* (27), 13445–13453.
(41) Faucheaux, J. A.; Fu, J.; Jain, P. K. Unified Theoretical Framework for Realizing Diverse Regimes of Strong Coupling Between Plasmons and Electronic Transitions. *J. Phys. Chem. C* **2014**, *118* (5), 2710–2717.
(42) Fofang, N. T.; Grady, N. K.; Fan, Z.; Govorov, A. O.; Halas, N. J. Plexciton Dynamics: Exciton−Plasmon Coupling in a J-Aggregate−Au Nanoshell Complex Provides a Mechanism for Nonlinearity. *Nano Lett.* **2011**, *11* (4), 1556–1560.

(43) Dowgiallo, A.-M.; Schwartzberg, A. M.; Knappenberger, K. L., Jr. Structure-Dependent Coherent Acoustic Vibrations of Hollow Gold Nanospheres. *Nano Lett.* **2011**, *11* (8), 3258–3262.
(44) Dowgiallo, A.-M.; Knappenberger, K. L. Ultrafast Electron–Phonon Coupling in Hollow Gold Nanospheres. *Phys. Chem. Chem. Phys.* **2011**, *13* (48), 21585–21588.
(45) Simon, T.; Melnikau, D.; Sánchez-Iglesias, A.; Grzelczak, M.; Liz-Marzán, L. M.; Rakovich, Y.; Feldmann, J.; Urban, A. S. Exploring the Optical Nonlinearities of Plasmon-Exciton Hybrid Resonances in Coupled Colloidal Nanostructures. *J. Phys. Chem. C* **2016**, *120* (22), 12226–12233.
(46) Cacciola, A.; Di Stefano, O.; Stassi, R.; Saija, R.; Savasta, S. Ultrastrong Coupling of Plasmons and Excitons in a Nanoshell. *ACS Nano* **2014**, *8* (11), 11483–11492.
(47) Liebel, M.; Schnedermann, C.; Wende, T.; Kukura, P. Principles and Applications of Broadband Impulsive Vibrational Spectroscopy. *J. Phys. Chem. A* **2015**, *119* (36), 9506–9517.
(48) Lorenc, M.; Ziolek, M.; Naskrecki, R.; Karolczak, J.; Kubicki, J.; Maciejewski, A. Artifacts in Femtosecond Transient Absorption Spectroscopy. *Appl Phys B* **2002**, *74* (1), 19–27.
(49) Kovalenko, S. A.; Dobryakov, A. L.; Ruthmann, J.; Ernsting, N. P. Femtosecond Spectroscopy of Condensed Phases with Chirped Supercontinuum Probing. *Phys. Rev. A* **1999**, *59* (3), 2369–2384.
(50) Berciaud, S.; Cognet, L.; Tamarat, P.; Lounis, B. Observation of Intrinsic Size Effects in the Optical Response of Individual Gold Nanoparticles. *Nano Lett.* **2005**, *5* (3), 515–518.
(51) Sönnichsen, C.; Franzl, T.; Wilk, T.; Plessen, von, G.; Feldmann, J.; Wilson, O.; Mulvaney, P. Drastic Reduction of Plasmon Damping in Gold Nanorods. *Phys. Rev. Lett.* **2002**, *88* (7), 957–4.
(52) Devkota, T.; Brown, B. S.; Beane, G.; Yu, K.; Hartland, G. V. Making Waves: Radiation Damping in Metallic Nanostructures. *J. Phys. Chem.* **2019**, 1–13.
(53) Balci, S.; Küçüköz, B.; Balci, O.; Karatay, A.; Kocabas, C.; Yaglioglu, G. Tunable Plexcitonic Nanoparticles: a Model System for Studying Plasmon–Exciton Interaction From the Weak to the Ultrastrong Coupling Regime. *ACS Photonics* **2016**, *3* (11), 2010–2016.
(54) Munkhbat, B.; Wersäll, M.; Baranov, D. G.; Antosiewicz, T. J.; Shegai, T. Suppression of Photo-Oxidation of Organic Chromophores by Strong Coupling to Plasmonic Nanoantennas. *Science Advances* **2018**, *4* (7), eaas9552.
(55) Moll, J.; Harrison, W. J.; Brumbaugh, D. V.; Muenter, A. A. Exciton Annihilation in J-Aggregates Probed by Femtosecond Fluorescence Upconversion. *J. Phys. Chem. A* **2000**, *104* (39), 8847–8854.
(56) Hodak, J. H.; Henglein, A.; Hartland, G. V. Photophysics of Nanometer Sized Metal Particles: Electron−Phonon Coupling and Coherent Excitation of Breathing Vibrational Modes. *J. Phys. Chem. B* **2000**, *104* (43), 9954–9965.
(57) Knappenberger, K. L., Jr.; Schwartzberg, A. M.; Dowgiallo, A.-M.; Lowman, C. A. Electronic Relaxation Dynamics in Isolated and Aggregated Hollow Gold Nanospheres. *J. Am. Chem. Soc.* **2009**, *131* (39), 13892–13893.
(58) Voisin, C.; Christofilos, D.; Loukakos, P. A.; Del Fatti, N.; Vallée, F.; Lermé, J.; Gaudry, M.; Cottancin, E.; Pellarin, M.; Broyer, M. Ultrafast Electron-Electron

Scattering and Energy Exchanges in Noble-Metal Nanoparticles. *Phys. Rev. B* **2004**, *69* (19), 365–13.

(59) Hartland, G. V.; Besteiro, L. V.; Johns, P.; Govorov, A. O. What's So Hot About Electrons in Metal Nanoparticles? *ACS Energy Lett.* **2017**, *2* (7), 1641–1653.

(60) Voisin, C.; Del Fatti, N.; Christofilos, D.; Vallée, F. Ultrafast Electron Dynamics and Optical Nonlinearities in Metal Nanoparticles. *J. Phys. Chem. B* **2001**, *105* (12), 2264–2280.

(61) Hartland, G. V. Coherent Vibrational Motion in Metal Particles: Determination of the Vibrational Amplitude and Excitation Mechanism. *J. Phys. Chem.* **2002**, *116* (18), 8048–8055.

(62) Pelton, M.; Sader, J. E.; Burgin, J.; Liu, M.; Guyot-Sionnest, P.; Gosztola, D. Damping of Acoustic Vibrations in Gold Nanoparticles. *Nature Nanotech* **2009**, *4* (8), 492–495.

(63) Zijlstra, P.; Tchebotareva, A. L.; Chon, J. W. M.; Gu, M.; Orrit, M. Acoustic Oscillations and Elastic Moduli of Single Gold Nanorods. *Nano Lett.* **2008**.

(64) Major, T. A.; Lo, S. S.; Yu, K.; Hartland, G. V. Time-Resolved Studies of the Acoustic Vibrational Modes of Metal and Semiconductor Nano-Objects. *J. Phys. Chem. Lett.* **2014**, *5* (5), 866–874.

(65) Hartland, G. V. Ultrafast Studies of Single Semiconductor and Metal Nanostructures Through Transient Absorption Microscopy. *Chem. Sci.* **2010**, *1* (3), 303–307.

(66) Wiederrecht, G. P.; Wurtz, G. A.; Hranisavljevic, J. Coherent Coupling of Molecular Excitons to Electronic Polarizations of Noble Metal Nanoparticles. *Nano Lett.* **2004**, *4* (11), 2121–2125.

(67) Voisin, C.; Christofilos, D.; Del Fatti, N.; Vallée, F.; Prével, B.; Cottancin, E.; Lermé, J.; Pellarin, M.; Broyer, M. Size-Dependent Electron-Electron Interactions in Metal Nanoparticles. *Phys. Rev. Lett.* **2000**, *85* (10), 2200–2203.

(68) Balci, S.; Kocabas, C.; Küçüköz, B.; Karatay, A.; Akhüseyin, E.; Gul Yaglioglu, H.; Elmali, A. Probing Ultrafast Energy Transfer Between Excitons and Plasmons in the Ultrastrong Coupling Regime. *Appl. Phys. Lett.* **2014**, *105* (5), 051105–051106.

(69) Darby, B. L. Modified Optical Absorption of Molecules on Metallic Nanoparticles at Sub-Monolayer Coverage. *Nat. Photonics* **2015**, *10* (1), 40–45

Chapter 3. Investigating the Role of the Organic Cation in Formamidinium Lead Iodide Perovskite using 2DIR and TRIR spectroscopy

The results, data and discussion presented in this chapter have been published with the reference: V. C. A. Taylor, D. Tiwari, M. Duchi, P. M. Donaldson, I. P. Clark, D. J. Fermin, and T. A. A. Oliver, *J. Phys. Chem. Lett.* **2018,** 9(4), 895–901.

Dr. Devendra Tiwari synthesised and characterised the samples (x-ray crystallography and scanning electron microscopy) and performed molecular dynamics simulations. I collected the 2DIR data at the Rutherford Appleton Laboratory using apparatus constructed by Dr. Paul Donaldson. The TRIR data were collected in an established ultrafast laboratory at the University of Bristol. I analysed all the data and wrote the manuscript in discussions with my supervisor Dr Tom Oliver.

3.1. Introduction

Hybrid organic-inorganic perovskites have found recent prominence as the active photovoltaic layer in optoelectronic devices due to high and balanced charge mobilities,[1] tuneable bandgaps,[2] and high absorption cross-sections.[3] Perovskite films are cheap to synthesize using solution processing techniques, with functionality seemingly unimpaired by impurities, unlike competing semiconductors.[4] In addition to photovoltaics, perovskites have shown great promise for applications ranging from lasers,[5] photodetectors,[6] light-emitting devices,[7] thin film transistors [8] to spintronics.[9] Despite intense research efforts to enhance these promising attributes,[3,10-17] an underlying mechanistic understanding of these highly desirable properties remains nebulous.

Organic lead iodide perovskites take the stoichiometry $APbI_3$, where A is an organic cation. In an ideal cubic perovskite crystal structure the organic cation is caged within an inorganic lattice comprised of a cube of lead cations with an iodide octahedron around each lead cation (Figure 3.1). Despite a simple chemical structure, hybrid inorganic-organic lead halide perovskites have been shown to be inherently complex materials that support a diverse range of dynamical processes essential to their photovoltaic performance. These phenomena include organic and inorganic ion diffusion,[18] organic cation rotation,[14,15,19,20] and octahedral distortions[17,21] and operate over a multitude of timescales.

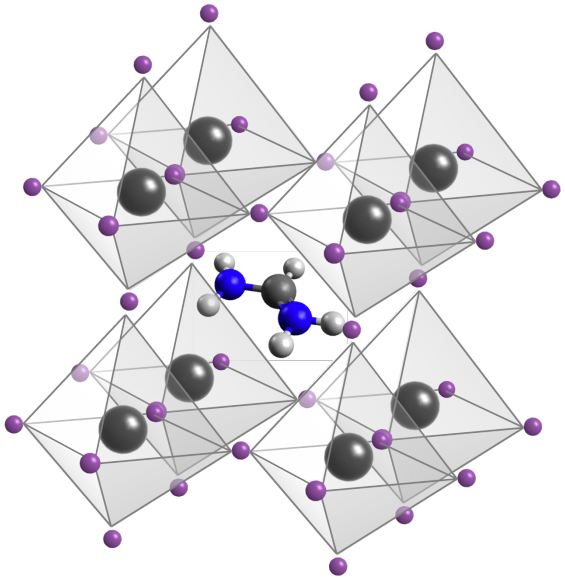

Figure 3.1: Schematic cubic perovskite crystal structure of $FAPbI_3$. The organic formamidinium cation is shown surrounded by an inorganic lattice of lead and iodine atoms, grey and purple respectively.

The choice of organic cation in lead halide perovskites is significant. It can determine the most stable phase at room temperature (*e.g.* orthorhombic *vs.* tetragonal), resulting in different band gap energies.[2,21-23] Whether this arises from purely steric effects and changes to the lead iodide lattice spacing, or via changes in electronic structure induced by different van der Waals interactions between the cation and surrounding inorganic lattice, is a matter of controversy.[24-26] Several prominent studies have proposed that the rapid reorientation and/or alignment of organic cations may be a crucial factor contributing towards the observed low charge recombination rates for hybrid perovskites. [1,16,23,27] The proposed mechanisms involve either (i) photoexcited charge carriers causing proximal cations to reorient, inducing fluctuations and distortions in the inorganic lattice through van der Waals electrostatic interactions and the formation of large polarons;[20,26,28,29] or (ii) neighbouring organic cation dipoles aligning to form (anti)ferroelectric domain, which can channel opposite charges away from each other via the boundaries of such domains.[23,27,30,31] Studies of the hybrid perovskite archetype, methylammonium lead iodide perovskite ($MAPbI_3$), revealed that the organic cation reorients on the order of several picoseconds at room temperature.[12,14,15,19]

Some of the latest hybrid lead halide perovskite thin films contain formamidinium ($NH_2CHNH_2^+$, FA^+) as the organic cation. These perovskites exhibit a favourable red-shift towards the ideal band gap.[32] A study examining the carrier diffusion length of single crystals, indicated that many lead-halide (Br, I) perovskites incorporating FA^+ display

increased carrier diffusion lengths by up to a factor of four (*cf.* methylammonium containing perovskites), which was attributed to ferroelectric domain formation.[1] Despite these promising photovoltaic properties, to date, experimental studies have yet to directly determine the presence of ferroelectric domains in formamidinium lead iodide perovskite ($FAPbI_3$) thin films, and make a direct connection between their promising photoactive properties and underlying molecular structure.

This work investigates the vibrational dynamics associated with the formamidinium cation in $FAPbI_3$ films and elucidates the influence of the reorientation time scales of FA^+ on the photophysical material properties using two- dimensional vibrational spectroscopy (2DIR). In addition, time-resolved infrared spectroscopy (TRIR) measurements were also used to probe the effect of photo-induced charges on the organic cation in $FAPbI_3$ thin films. This work shows, for the first time, that FA^+ reorientation is characterized by 470 ± 50 fs and 2.8 ± 0.5 ps time constants. Such rapid reorientation shows that ferroelectric domains are unlikely to play any role in long carrier lifetimes.

3.2. Experimental Methods

3.2.1. Sample synthesis and Characterisation

Two types of samples were synthesised: $FAPbI_3$ thin films deposited on Calcium Fluoride (CaF_2) substrates, and $FAPbI_3$ thin films sandwiched between hole transport material spiro-OMeTAD and electron acceptor titanium dioxide. All samples were prepared using a two-step synthesis to deposit the thin $FAPbI_3$ films. First, a lead iodide film was generated by gas phase iodination of a nanostructured PbS film spin-coated onto a CaF_2 substrate at 200 °C, following a recently reported procedure.[1] The resulting lead iodide film was then soaked in a solution of formamidinium iodide for 20 minutes and annealed at 170 °C for 10 minutes, before being left to cool under an argon atmosphere. Finally, the sample was capped with another calcium fluoride window and sealed with epoxy resin to inhibit exposure of the sample to ambient moisture.

Samples with charge transport materials were prepared to yield the following structure: $CaF_2/TiO_2/FAPbI_3$/spiro-OMeTAD/CaF_2. A compact TiO_2 layer was first deposited onto CaF_2 windows by spin-coating a 1:40 solution of titanium isopropoxide and ethanol at 5000 rpm, whilst heating at 500 °C in air. The $FAPbI_3$ layer was deposited directly onto the TiO_2 using the method described above. Finally, the hole transport layer

of spiro-OMeTAD was coated onto the $FAPbI_3$ layer following a previously reported method.[2]

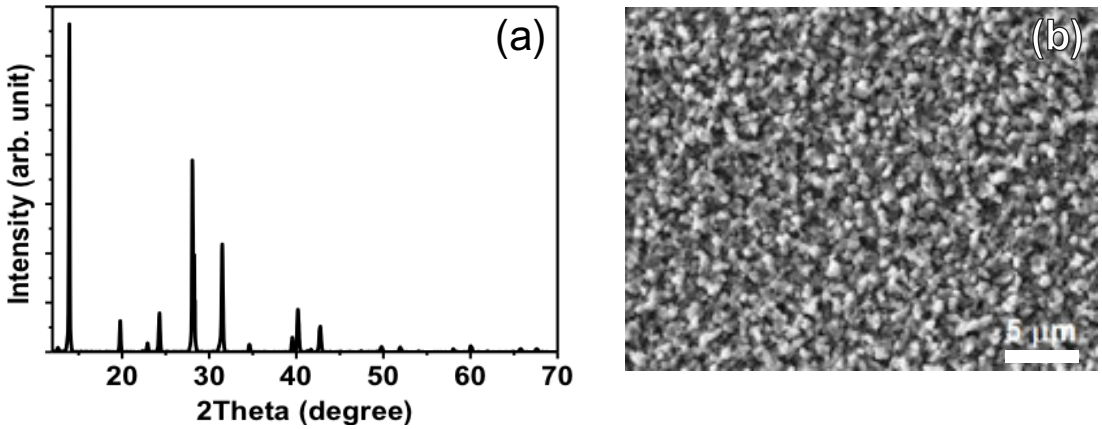

Figure 3.2: (a) X-ray diffraction of $FAPbI_3$ film, with cubic (Pm3m) structure. (b) Scanning electron micrograph image of $FAPbI_3$ film, showing cubic grains of approximately 500 nm diameter.

Powder X-ray diffraction (Bruker D8 Advance, Cu Kα source) measurements confirmed the formation of $FAPbI_3$ in cubic α-phase (Pm3m), also known as the black phase (Figure 3.2 (a)).[3] Within the detection limits of the equipment, no signature of the orthorhombic "yellow" δ-phase was observed. The morphology of the films was probed using scanning electron microscopy (SEM) and revealed the formation of a conformal film comprised from cubic grains of around 500 nm (Figure 3.2 (b)). The thickness of the films was determined to be 500 nm from cross-sectional SEM. All the measurements were carried out within 3 hours of deposition to minimise the possibility of conversion back to the PbI_2 precursor.[4] Linear visible and infrared absorption measurements of the samples (see example in Figure 3.3) before and after ultrafast laser experiments confirmed that no detectable sample degradation occurred.

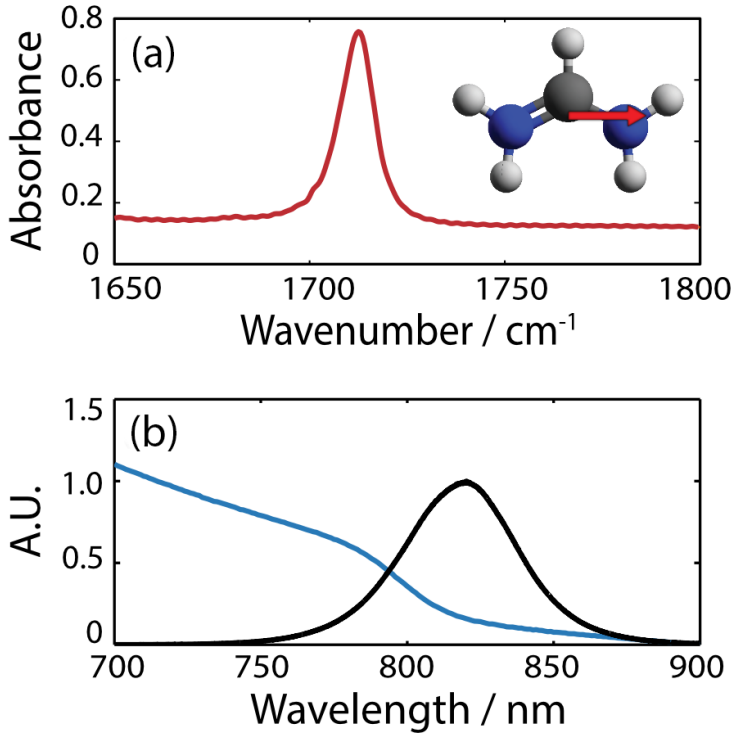

Figure 3.3: (a) Linear infrared absorption spectrum, and inset optimized CCSD/aug-cc-pVTZ structure of the FA^+ cation, with overlaid vibrational transition dipole moment for the C–N antisymmetric stretching vibration. (b) Linear electronic absorption (blue) and fluorescence spectra (black) for the $FAPbI_3$ sample used in this study.

3.2.2. 2DIR measurements

Two-dimensional infrared spectroscopy (2DIR) measurements were performed at the Rutherford Appleton Laboratory ULTRA facility using the LIFEtime laser system. The details of the experimental apparatus have been reported previously.[33,34] Briefly, a 100 kHz repetition rate 15W Yb:KGW laser (Pharos, Light Conversion Ltd.) was used to pump two optical parametric amplifiers (OPAs) and generate broadband mid-infrared pump and probe pulse trains centred at 1720 cm^{-1}. These pulses were used in mixed time-frequency domain 2DIR experiments in the partially collinear geometry. An acousto-optic programmable filter pulse shaper (Phasetech) was used to generate a pair of collinear phase-locked pump pulses, with attosecond precision over the coherence time delay (t_1). The collinear pump pair were focussed into the sample and overlapped with probe pulses. The waiting time delay, t_2, was controlled by a mechanical delay stage. In the partially collinear geometry, the 3rd order non-linear signal is emitted collinearly to the probe pulse. The probe and signal were collimated after the sample, imaged into a spectrograph,

frequency dispersed onto a 128 element HgCdTe mid-IR array detector (Infrared Associates Inc.) and digitised.

For a given waiting time delay, the probe infrared spectral intensity (ω_3), modulated by k_{sig}, was recorded as a function of the t_1 time delay (0 and 6 ps in 24 fs steps). These data were averaged using an 8-step phase cycling scheme, which also serves to remove background pump-probe signals. Each data point was averaged for 10 s (10,000 laser shots). The polarisations of the pump and probe beams were set independently using waveplate polariser pairs. Measurements were made with shaped pump powers of 13.5 and 8 mW (135 nJ and 80 nJ /pulse) at the sample, henceforth referred to as 'high' and 'low' power respectively. The sample was continually rastered through the beam focus to mitigate sample damage. Temporal dispersion of the pump pulses was corrected for using the pulse shaper. Germanium plates were used to correct for 2nd order GVD in the probe pulse. The 2DIR IRF response was characterised via examining the response of water, returning an IRF of 220 fs. All data fitting in this study excludes 2DIR data at $t_2 \leq 250$ fs.

Following collection, all datasets were inverse-Fourier transformed into the time-domain (t_1–t_3 space), where a very gentle 2D Tukey window was applied before zero-padding. The processed time domain data were then Fourier-transformed into the frequency domain, where a Savitzky-Golay filter was applied along the probe dimension to remove any evident artefacts arising from water vapour absorptions. Great care was taken to ensure every step of the data processing did not affect the 2DIR line shapes.

3.2.3. TRIR measurements

Time-resolved infrared (TRIR) measurements were performed using an established ultrafast laser system at the University of Bristol.[35] The ultrafast laser system comprised of an oscillator (Vitara-S, Coherent) which seeded a 5 W, 1 kHz, 35 fs amplifier (Legend Elite HE+, Coherent) which was used to pump two OPAs. One OPA was configured to generate 760 nm pump pulses (~100 fs), the second was used to generate broadband (~300 cm^{-1}) IR probe pulse centred at ~1725 cm^{-1}. The pump beam line was modulated by a mechanical chopper at 500 Hz, and the pump fluence at the sample was attenuated using a polariser waveplate pair. Measurements were acquired using pump energies of 30, 60, 90 and 120 nJ pulse^{-1} in a ~480 μm diameter spot, which correspond to power densities of: 0.66, 1.32, 1.99, 2.65 GW/cm^2. A small portion of the mid-IR light was used as a reference beam to correct for shot-to-shot instabilities. The sample was rastered during experiments to avoid

damage to the sample. Signal and probe beams were focused into two spectrometers (iHR320, HORIBA Scientific) and imaged on a pair of 128-pixel, liquid nitrogen cooled, Mercury Cadmium Telluride linear array detectors (MCT-10−128, Infrared Associates Inc.), affording a spectral resolution of ~2 cm^{-1}.

3.3. Computational modelling and data analysis

3.3.1. Gas phase calculations of the FA^+ cation vibrionic modes

The strong mid-infrared peak centred at 1713 cm^{-1}, in the FAPbI3 FTIR spectrum (see Figure 3.3(a)) was used to probe the inorganic lattice−molecular cation interactions in the 2DIR and TRIR measurements. This peak has previously been attributed to the C=N symmetric stretching vibration of the FA cation,[36,37] however, these studies did not include any justification for this assignment. Therefore, the normal modes and associated frequencies of the formamidinium cation were calculated using high-level coupled cluster gas phase *ab initio* calculations as follows.

Table 3.1 Optimised molecular geometry (in Angstroms) of the formamidinium cation, calculated at the CCSD/aug-cc-pVTZ level.

Atom	x / Å	y / Å	z / Å
C	0.0000001533	-0.4253427043	0.0000000815
N	-0.0000003148	0.1779423415	1.1602828944
N	-0.0000000715	0.1779423482	-1.1602828335
H	0.0000003302	-0.3669166197	-2.0067446623
H	-0.0000006382	1.1821155152	-1.2534287242
H	0.0000007745	-1.5073550079	-0.0000003961
H	0.0000031651	1.1821157460	1.2534265593
H	-0.0000000907	-0.3669154656	2.0067454050

Coupled cluster with single and double excitations (CCSD) theory using Dunning's augmented correlation consistent basis set of triple ζ quality (aug-cc-pVTZ) were used to optimize the FA^+ ground state structure and vibrational frequencies. The Molpro 2015 suite was used for all *ab initio* calculations.[38] The CCSD/aug-cc-pVTZ optimized molecular geometry is given in table 3.1. The calculations return a ground state permeant dipole moment of 0.1723 Debye, which is close to the previously reported value by Frost *et al.*[27] The gas phase harmonic vibrational frequencies are given in Table 3.2. Applying an empirical anharmonic correction multiplicative factor of 0.96,[39] shifts the high oscillator strength vibrational mode, ν_6, associated with C–N anti-symmetric stretching motions to

1723 cm^{-1}, which is in good agreement with the observed infrared peak in the FTIR spectrum centred at 1713 cm^{-1}. Therefore, the 1713 cm^{-1} feature can be assigned to the C–N antisymmetric stretching vibration instead of the C=N symmetric stretching vibration as previously asserted. The vector of the associated vibrational transition dipole moment lies in the plane of the molecule along an axis that lies parallel to the two nitrogen atoms (see Figure 3.3(a) inset).

Table 3.2: Calculated harmonic vibrational frequencies of gas phase FA^+, calculated at the CCSD/aug-cc-pVTZ level, listed in Herzberg notation.[40]

Normal Mode	Wavenumber / cm^{-1}	Infrared Intensity / km mol^{-1}
ν_1	3709	195
ν_2	3708	94
ν_3	3597	46
ν_4	3581	352
ν_5	3240	8
ν_6	1795	482
ν_7	1714	40
ν_8	1634	3
ν_9	1435	8
ν_{10}	1392	78
ν_{11}	1140	2
ν_{12}	1111	18
ν_{13}	1045	0
ν_{14}	728	3
ν_{15}	609	425
ν_{16}	592	0
ν_{17}	539	0
ν_{18}	519	0

3.3.2. Molecular Dynamics Simulations of the $FAPbI_3$ unit cell

For molecular dynamics (MD) simulations, the $FAPbI_3$ unit cell was relaxed and optimized using DFT first principles formalism in the CASTEP 16.0 computational suite.[41] For these calculations the PBESOL functional with norm-conserving on-the-fly pseudo potentials with a 1000 eV energy cut-off were used. Reciprocal space was sampled with a 0.02 $Å^{-1}$

spaced Monkhorst-Pack mesh, and relativistic effects were approximated using the ZORA scheme. The unit cell was relaxed with energy and force tolerances of 1 x 10^{-8} eV and 5 x 10^{-4} eV/ Å, per atom respectively. The optimised unit cell has the following lattice parameters: $a = 6.41609$ Å, $b = 6.36181$ Å, $c = 6.25078$ Å, and $\alpha = \beta = \gamma = 90^{o}$. The phonon density of states, displayed in Figure 3.4, was calculated for a $FAPbI_3$ unit cell based on linear response formalism under DFT PBESOL perturbation theory.

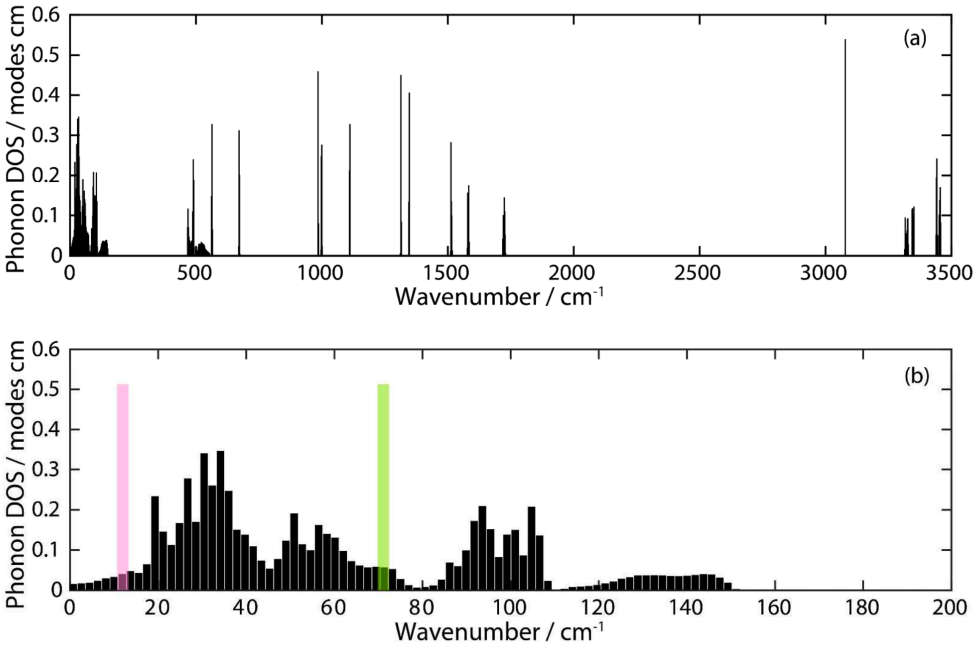

Figure 3.4. (a) Phonon density of states (DOS) returned by DFT/PBESOL calculations and (b) zoom of 0–200 cm^{-1} region, with overlaid bars to highlight frequencies obtained from rotational anisotropy results.

Classical MD simulations were performed on an 8 × 8 × 8 supercell of the optimized structure, comprising 512 FA^+ cations. The system under NVT ensemble was equilibrated in a Nośe-Hoover-Langevin thermostat at 300 K (Q-ratio = 3.0 and decay constant of 25 fs) employing a force-field based on MYP model,[42] accounting for the effect Pb and I ion dynamics as well. For electrostatic interactions Ewald summation with an accuracy of 1 x 10^{-6} $Å^{-1}$, was utilized.

After an equilibration of 1 ns, a production run of 100 ps was recorded with a resolution of 0.1 fs collecting every 200th frame. The average rotational correlation function (RCF) of FA^+ cations about the axis that intersects the two nitrogen atoms was extracted by averaging the individual RCF of 83 cations for the first 10 ps of the MD simulation.

Note that, these MD simulations return different re-orientation times compared to previous Born-Oppenheimer DFT-PBESOL MD simulations.[43] The simulations used in

this work are classical MD simulations, and thus can afford to sample a far larger supercell (8 × 8 × 8) incorporating 512 FA^+ units. The force field used accounts for effects of Pb/I ion dynamics and implements a Nośe-Hoover-Langevin thermostat. Both factors allow for a more realistic distribution of temperature fluctuations as expected for a canonical ensemble.

3.3.3. 2DIR thermal component analysis

The 2DIR response of a $FAPI_3$ film with the pump and probe in parallel polarisation is displayed in Figure 3.5 for four different waiting times as change in optical density. The spectra are dominated by two features; the negative feature centred on the diagonal (black dashed line) at 1713 cm^{-1} is related to overlapping ground state bleach (GSB) and stimulated emission (SE) signals associated with the C–N antisymmetric stretch of the FA^+ cation. The positive feature centred at ω_3 = 1706 cm^{-1} is due to the corresponding excited state absorption (ESA) signal.

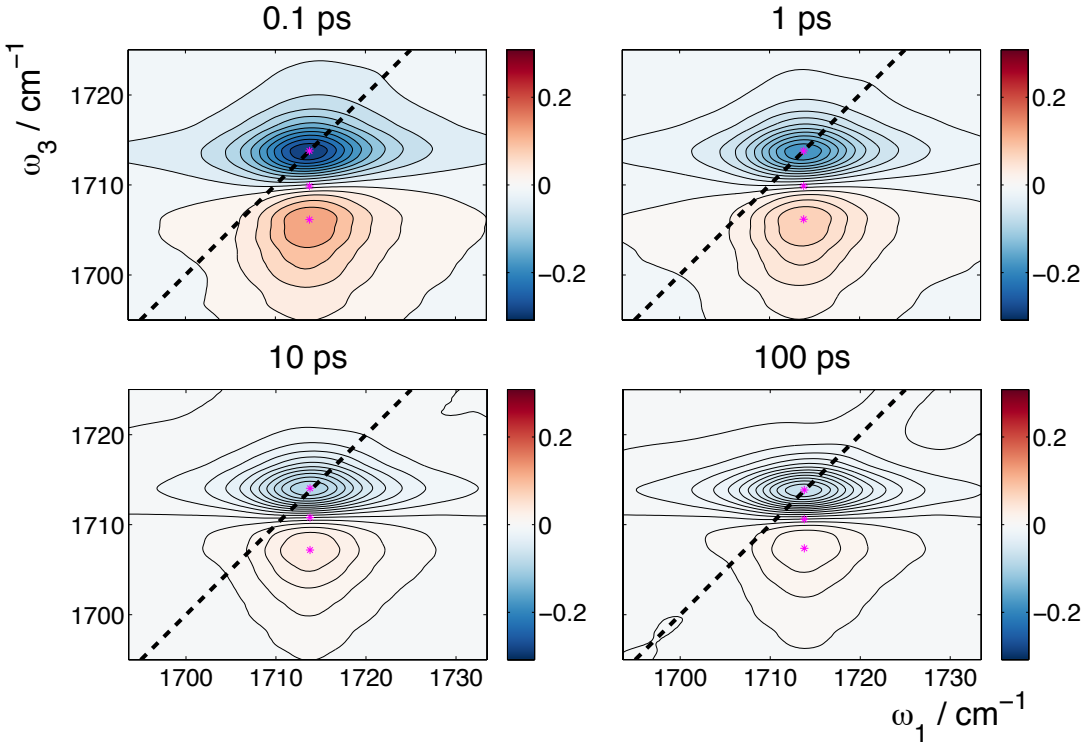

Figure 3.5. Parallel 2DIR data acquired with the lower pump power for the given t_2 time delays before HOSVD processing. Magenta stars denote the peaks of the features and the position of the node between them. Black dashed line indicates the diagonal.

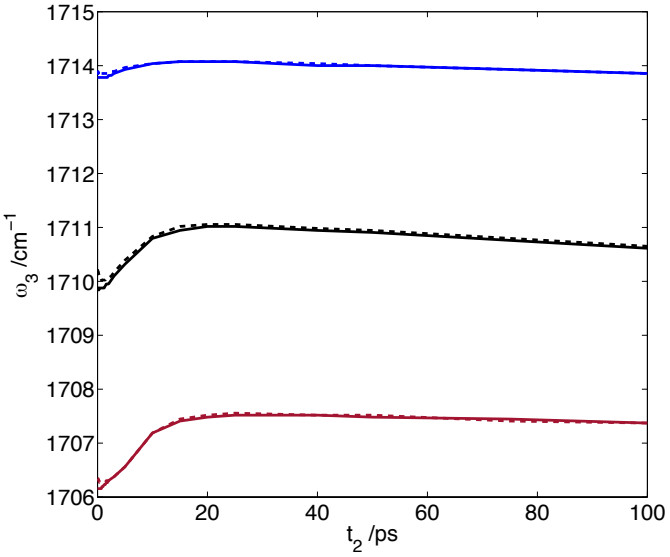

Figure 3.6: Central probe frequency (ω_3) of the GSB/SE (blue), node (black), and ESA (red) as a function of the waiting time. Data taken using the lower pump power on a sample of $FAPI_3$ film, with parallel and perpendicular pump/ probe polarizations denoted by solid and dashed lines respectively.

The negative feature, node and positive features all appear to shift along ω_3 with time (t_2); initially to higher frequency on a < 20 ps timescale, and then back towards the original central frequency. These shifts are displayed in Figure 3.6. The magnitude of the shift is greater for the ESA feature than the GSB/SE signal. Given that the magnitude of the shift decreased for larger ω_3, and the relatively slow rise time, this effect can be attributed to transient thermal heating consistent with that previously observed in $MAPbI_3$ 2DIR measurements.[12,14] The similarity in the shifts when the pump and probe are parallel or perpendicular (solid and dashed lines in Figure 3.6), indicates that the heating effects are, as would be expected, isotropic. The isotropic ($I_{iso}(t_2)$) signal of the sample represents the system's population relaxation dynamics. It can be retrieved from the dataset acquired with the pump and probe in parallel (I_{para}) and perpendicular (I_{perp}) polarization using the relation:

$$I_{iso}(t_2) = \frac{1}{3}\left(I_{para} + 2I_{perp}\right) \tag{3.1}$$

As the heating is isotropic, the effects of transient heating also manifest in the isotropic signal. In a simple three level system, the ground state bleach recovery and stimulated emission (monitored via 0–1 transition) should have the same dynamics as the ESA (monitored via 1–2/1–0 transitions), *e.g.* rate of GSB recovery should be the same as ESA/SE decay. The isotropic signal kinetics for the central ω_1 = 1713 cm^{-1} pump and

various ω_3 probes across the ESA, GSB/SE features are plotted in Figure 3.7. These data show very different vibrational lifetimes as a function of ω_3. For a simple three level system, such a large variation of the relaxation dynamics across different probe frequencies is not expected.

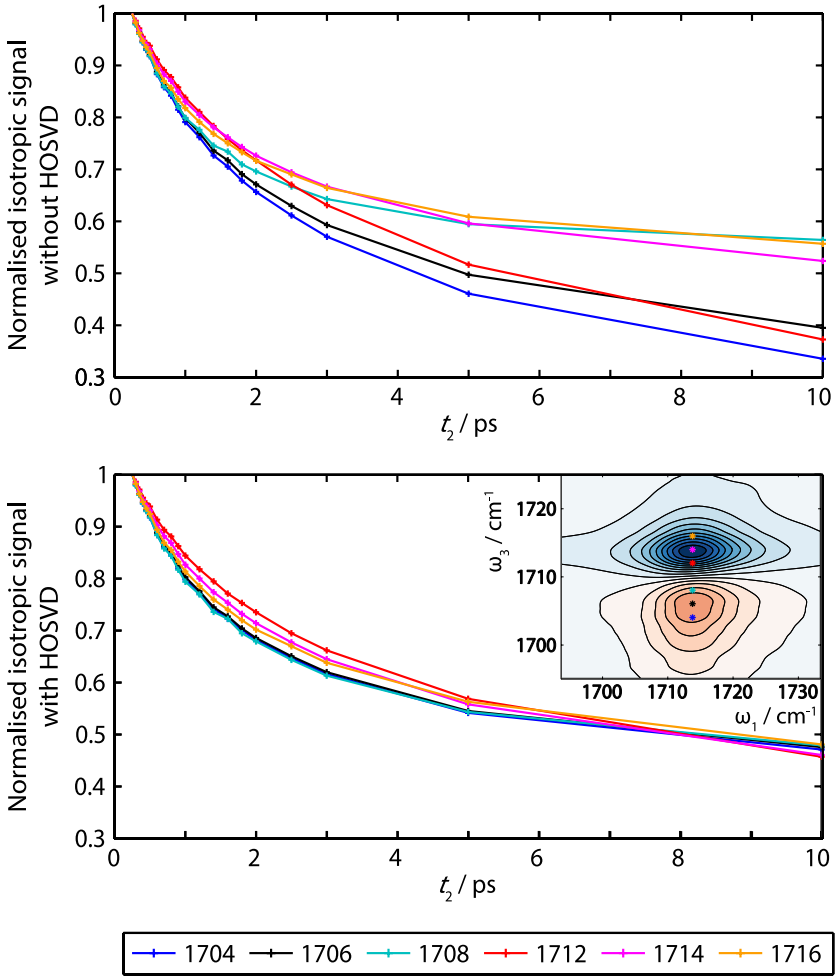

Figure 3.7: Variation in normalised isotropic kinetics for ω = 1713 cm^{-1} as a function of ω (given in legend in cm^{-1}) before (top) and after (bottom) HOSVD removal of heating effects. Data are normalised to t_2 = 250 fs. Inset shows the positions of these points within an example 2DIR spectrum.

In an attempt to remove the thermal heating effects from the 2DIR data and return vibrational lifetimes for the C–N anti-symmetric stretching mode of FA^+, a higher-order singular value decomposition[44] (HOSVD, the 3D equivalent of singular value decomposition, and also known as Multilinear SVD) was employed using a Matlab package, Tensor lab.[45] Considering the total data set $\mathbf{A}(\omega_3, \omega_1, t_2)$ as a third order tensor, which can be decomposed into a core tensor, **S**, (equivalent to the matrix of singular values

in SVD) multiplied by 3 matrices, $\mathbf{U^{(1)}}$, $\mathbf{U^{(2)}}$, and $\mathbf{U^{(3)}}$, corresponding to ω_3, ω_1 and t_2 dimensions respectively:

$$\mathbf{A}(\omega_3, \omega_1, t_2) = \mathrm{S} \bullet \mathbf{U^{(1)}} \bullet \mathbf{U^{(2)}} \bullet \mathbf{U^{(3)}} \tag{3.2}$$

To eliminate approximation errors relating to truncation, the decomposition was calculated with a core tensor with equal rank to the dataset tensor, **A**. Then a tensor of 2D spectral surfaces $\mathbf{W}(\omega_1, \omega_3)$, each with their own time dependence, $\mathbf{U^{(3)}}$, was generated by recombining the relevant tensor components **S**, $\mathbf{U^{(1)}}$, $\mathbf{U^{(2)}}$.

The HOSVD analysis returned multilinear single values of $\mathbf{U^{(3)}}$ which are displayed in Figure 3.8. It is apparent that the 2DIR data, **A**, are dominated by two major **W** and associated $\mathbf{U^{(3)}}$ components. The **W** (spectral component) and corresponding $\mathbf{U^{(3)}}$ (time dependence) are shown in Figure 3.9 for the first two components, $\mathbf{W_1}$ and $\mathbf{W_2}$. $\mathbf{W_1}$ contains ESA, GSB/SE features associated with the normal 2DIR spectra. The $\mathbf{W_2}$ spectrum, however, is dominated by dispersive line shape. The corresponding dynamics show that the dispersive line shape rises as a function of t_2 time-delay, peaking at ~20 ps, coincident with the observed spectral shifts in the original 2DIR data. Together these observations are indicative of a time-dependent change in the refractive index, which arises from thermal heating of the sample.

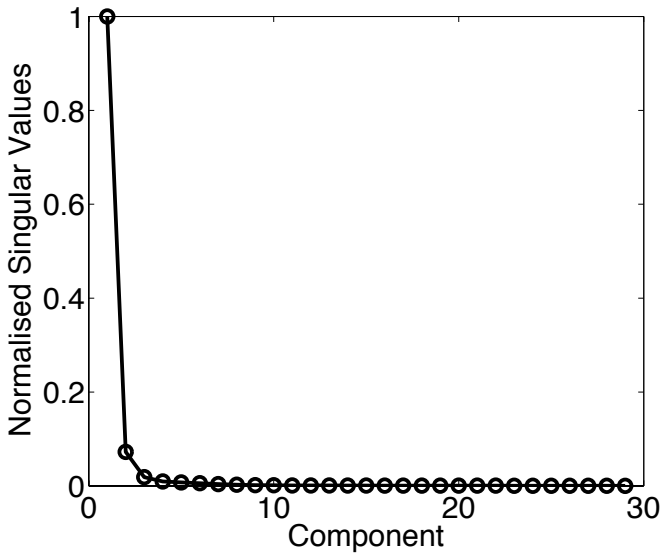

Figure 3.8: The ordered and normalised multilinear singular values of $\mathbf{U^{(3)}}$ (the t_2 dimension).

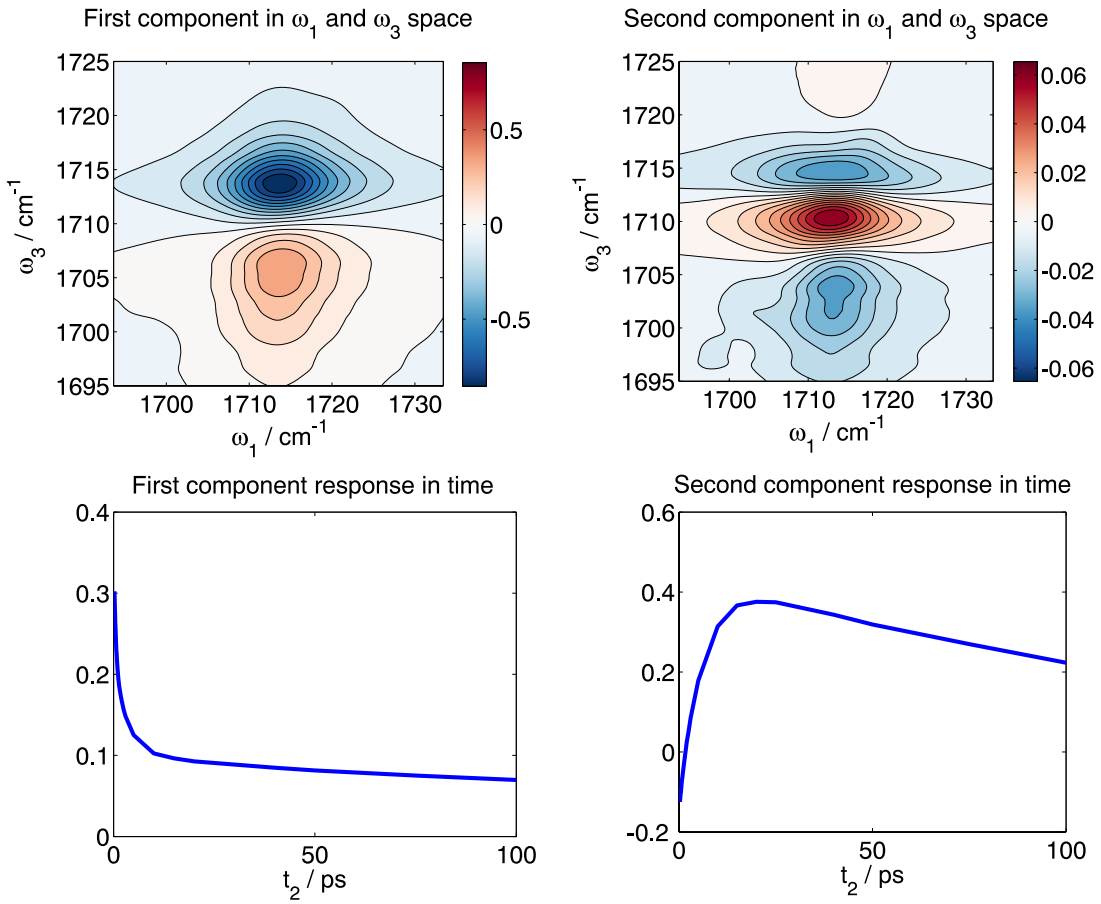

Figure 3.9: The first two components (ordered by decreasing singular value) of the HOSVD of the dataset taken at the lower pump power with pump and probe in parallel polarisations. Top panels show components of **W** (**W**$_1$ and **W**$_2$). Bottom panels display the corresponding time response (components of **U**$^{(3)}$).

To minimise these effects, the 2DIR data was reconstructed by the relation:

$$\mathbf{A} = \mathbf{S} \bullet \mathbf{W} \bullet \mathbf{U}^{(3)} \tag{3.3}$$

but with **W**$_2$ set to 0. This means that any minor spectral shifts, such as changes in nodal or central line slopes that will likely have small amplitude components, are retained in the reported data (Figure 3.10). Note that by nature of the HOSVD, the separated components are restricted such that the features do not shift in ω_1 or ω_3 in time. However, by this method, only intensities in the signal that vary in unison with the heating component would be removed, all other noise or shifting in intensity would be largely contained in the components with lower singular values. Therefore, if the features significantly shift in frequency, as is likely to occur in the dispersive feature at greater pump intensities, this method becomes less reliable. Hence, the low-power data sets are more reliable as they should contain a smaller component of thermal heating effects. The removed heating

component had a maximal intensity of 13% of the original 2DIR signal intensity out of every dataset and every waiting time.

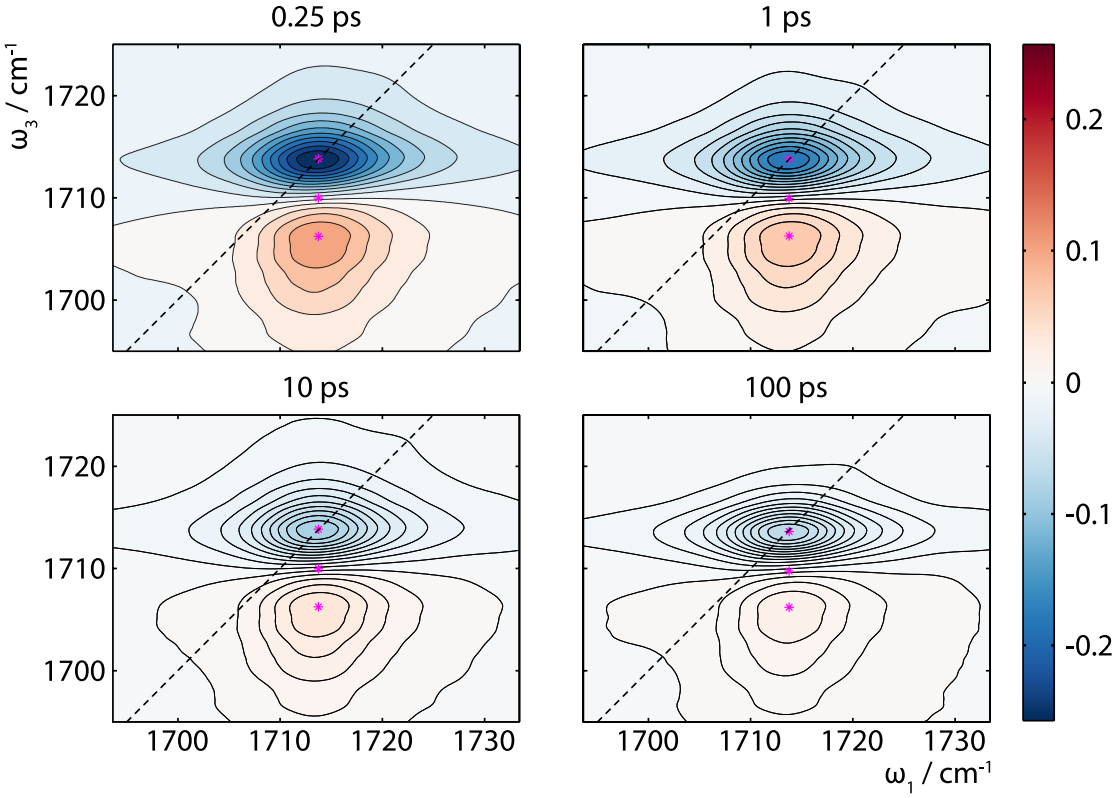

Figure 3.10: The same dataset as shown in figure 3.5, after HOSVD processing. Magenta stars denote the positions of the ESA maxima, GSB/SE minima and the nodes between them. Black dashed lines indicate the diagonal.

As mentioned above, heating effects are isotropic and so would not be expected to affect the anisotropic signal, a key measurement in this work to determine the FA^+ cation reorientation dynamics. The anisotropic response was calculated using the following relation:

$$R(t_2) = \frac{I_{para} - I_{perp}}{I_{para} + 2I_{perp}} \tag{3.4}$$

The time-dependent anisotropic response, $R(t_2)$, for GSB/SE and ESA features using the pre-HOSVD data is displayed in Figure 3.11, revealing almost identical kinetics.

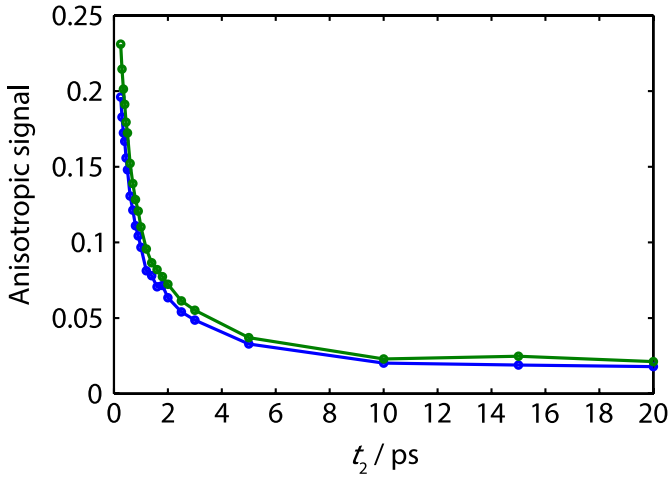

Figure 3.11: Comparison of anisotropy dynamics for GSB/SE (green) and ESA (blue) features using the lower power 2DIR data. Lines are a guide to the eye (not fits).

Since the heating component was found to affect the GSB/SE less than the ESA, in the following discussion the average signal intensity of a region over the bleach features is used as a measure of the signal intensity of the parallel and perpendicular datasets, I_{para} and I_{perp}, respectively. Comparisons of the signals returned pre- and post-HOSVD processing are given in Figure 3.12 for both the isotropic and anisotropic response of the GSB feature. The amplitude of the long-time component ($t_2 > 100$ ps) in the isotropic response is reduced but not entirely removed. The anisotropy dynamics are unaffected by HOSVD processing, returning almost identical $R(t_2)$ decay traces.

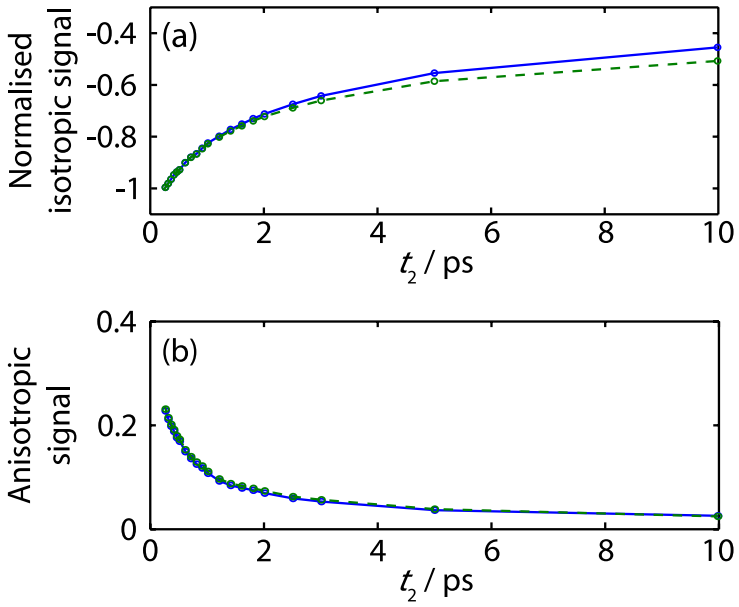

Figure 3.12: Green dotted lines and data points denote the GSB/SE normalised for (a) isotropic response and (b) the anisotropic response calculated using 2DIR data before HOSVD processing. Blue solid lines and data points denote responses calculated from data after HOSVD removal of heating effects. Lines are a guide to the eye only (not fits).

3.4. Results & Discussion

3.4.1. 2DIR results

3.4.1.1. Isotropic response

Figure 3.13 displays isotropic 2DIR spectra at four waiting times for FA^+ in $FAPbI_3$ only sample. The GSB/SE and ESA features are predominantly homogeneously broadened, *i.e.,* the diagonal and antidiagonal line widths are very similar, and they evolve little within the 100 ps measurement window.

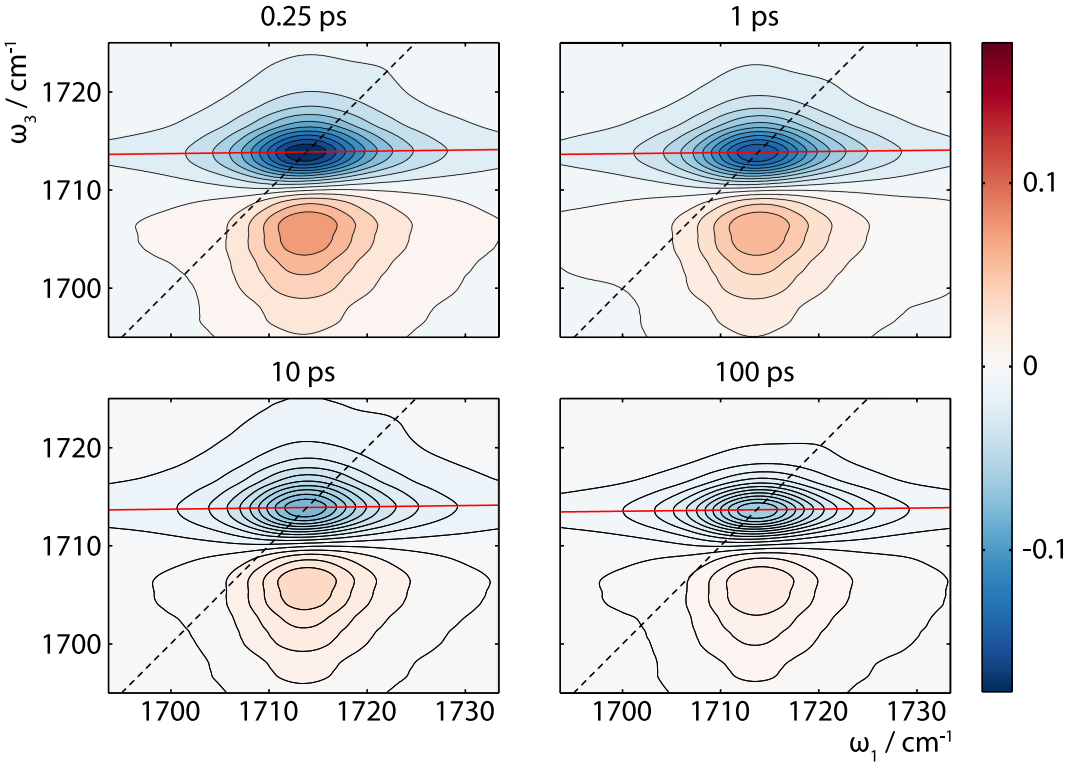

Figure 3.13: Isotropic 2DIR spectra of the C–N anti-symmetric stretching vibration of FA^+ in $FAPbI_3$ thin films, at the four displayed waiting times. Fill colours denote the intensity of the signal in ΔmOD. Fits to the GSB/SE centre line slope are displayed in red and black dashed lines mark the diagonal.

It has been shown that monitoring the gradient of the Centre line slope (CLS) of features in 2DIR spectra provides a reliable measure of the frequency-frequency correlation function[46], and therefore spectral diffusion. CLS analyses were performed on the GSB/SE features of the parallel, perpendicular, and the subsequently calculated isotropic data sets post-HOSVD. In all instances, the gradients of the line slopes were found to be small (<0.1) at early t_2 delay times and no correlation with time was apparent, indicating minimal or no spectral diffusion. An example of the CLS dynamics is given in Figure 3.14. This apparent lack of spectral diffusion will be addressed later in the context of the anisotropy results.

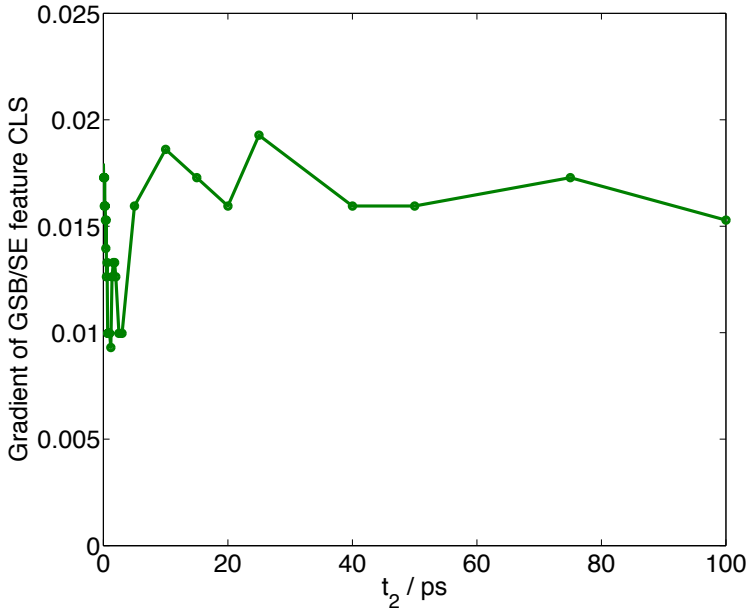

Figure 3.14: The gradient of the centre line slope of the GSB/ SE feature in the dataset shown in figure 3.13.

Figure 3.15(a) displays the population relaxation dynamics (isotropic signal) of the FA^+ C–N antisymmetric stretch GSB/SE feature for the two perovskite films. The kinetics associated with the film coated directly onto the CaF_2 windows and sandwiched between hole and electron transport materials, are essentially identical. These data were fit to a biexponential decay with 2.8 ± 0.2 ps and 500 ± 200 ps time constants. The 2.8 ps vibrational lifetime is similar to the vibrational lifetimes measured for the symmetric N^+H_3 bending mode of MA^+ in $MAPbI_3$ films.[12,14] The source of the long-lived component is unclear. FA^+ cations buried in the bulk and at the surface of the film provide a possible explanation, however, this is unlikely given the long-lived component comprises 45% of the signal amplitude and the small surface-to-bulk ratio of the film. Some studies report the formation of water complexes around organic cations in perovskites,[47] but given the care taken to use samples soon after synthesis this seems unlikely. The presence of any δ-$FAPbI_3$ (yellow phase) in the samples can be ruled out based on absorbance measurements before and after ultrafast spectroscopic measurements, and X-ray diffraction data. Therefore, it is most probable that the single value decomposition analysis is unable to fully remove the isotropic long-lived thermal heating component.

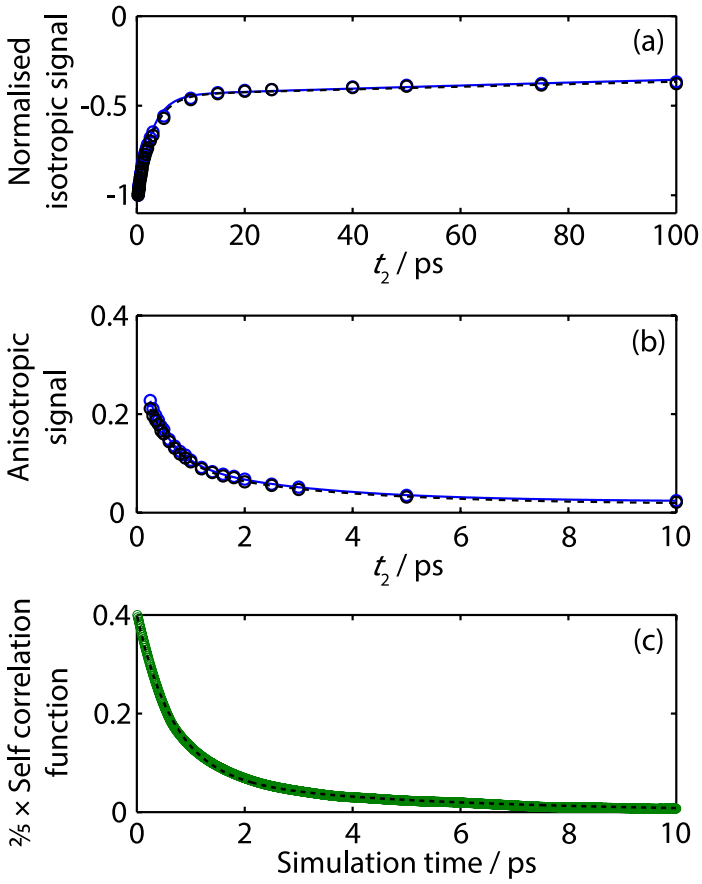

Figure 3.15 (a) Normalised population relaxation associated with the GSB/SE maxima for $FAPbI_3$ (blue circles) and $TiO_2/FAPbI_3$/Spiro-MeOTAD (black circles) with fits. (b) Anisotropy trace for the same feature between $0.25 \leq t_2 \leq 10$ ps. (c) Scaled autocorrelation response function returned by molecular dynamics simulations (green circles) and fit to the data in dashed black line.

3.4.1.2. Anisotropic response

Figure 3.15(b) displays the almost identical anisotropic responses of the GSB/SE antisymmetric C–N stretching vibrational feature of the $FAPbI_3$ film alone and sandwiched between charge transport layers. These data were fit to a biexponential decay with an offset, which returned 470 ± 50 fs and 2.8 ± 0.5 ps time constants, with associated normalised exponential pre-factors of 65% and 29%, and an offset corresponding to 6% of the total amplitude. The long-time non-zero values of $R(t_2)$ must arise from a small sub-ensemble of the cation population that is unable to reorient, such as cations situated at the edges of crystals or at the film-substrate interface. However, this is a very minor (6%) component of the total population.

Snapshots of the 298 K molecular dynamics simulations are given in Figure 3.16. They predict that the FA^+ cation preferentially orients $–NH_2$ groups towards opposing faces of cube formed by the Pb atoms. These observations are in agreement with a previous MD

simulation[48] and time-averaged neutron diffraction studies.[49] Two key motions associated with the formamidinium cation can be observed in these MD simulations: (i) the cation agitates around its mean position, but rotates around the axis formed by the two nitrogen atoms, and (ii) the cation undergoes a 90° jump about the centre of the cube, such that the FA^+ $–NH_2$ groups point towards an adjacent pair of opposing cube faces (compare Figure 3.16(a) to (b)). These simulations also reveal that no part of the FA^+ cation remains fixed at the centre of the cube.

The auto-correlation function around the rotational axes that passes through the two nitrogen atoms was averaged over 83 trajectories, returning the ensemble rotational re-orientation dynamics displayed in Figure 3.15(c). Fits to these data return 680 ± 10 fs and 4.5 ± 0.1 ps time constants, which are in good numerical agreement with the values determined from 2DIR anisotropy experiments. This distinctive two-part motion is reminiscent of the motions attributed to the MA^+ cation[12,14,19] in $MAPbI_3$, which used a coupled "wobbling in a cone/ angular jump model" to fit the anisotropy data.

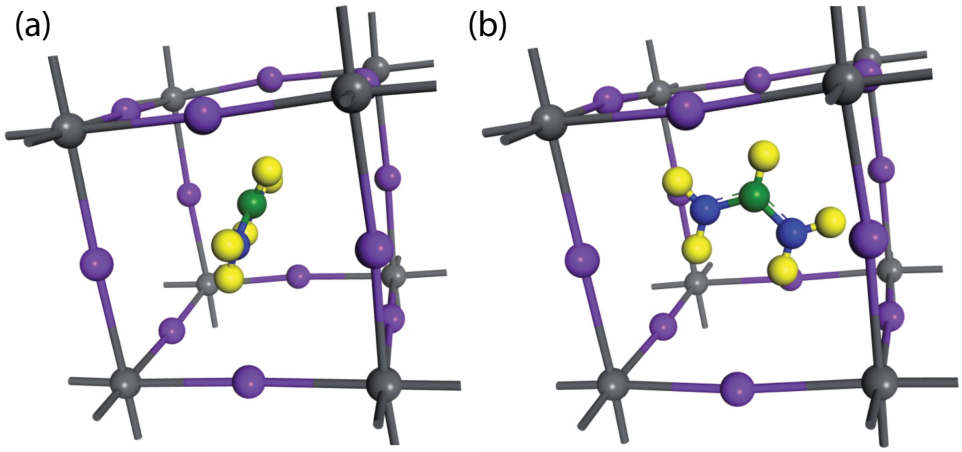

Figure 3.16: Representative snapshots from one cell of MD simulations highlighting the motions associated with a 90° flip between adjacent Pb cube faces.

The wobbling in a cone model approximates the small-range motion of the MA^+ cation to a libration about the centre of the inorganic lattice cube, within a cone (positioned with its base on a face of the cube and vertex at the centre) and semi-cone angle, ϕ_c. These motions are intrinsically linked to a larger 'jump-like' motion, during which the molecule undergoes a 90° rotation such that the cone is positioned on an adjacent cube face.

The wobbling in the cone model is defined[12,14,50] as:

$$r(t_2) = \frac{2}{5}\left(S^2 \exp\left(\frac{-t_2}{\tau_{jump}} \right) + \left(1 - S^2\right) \exp\left(-\left(\frac{1}{\tau_{jump}} + \frac{1}{\tau_{wob}} \right) t_2 \right) \right) \tag{3.5}$$

where t_2 is the delay time between the pump and probe pulses (as defined previously), τ_{jump} and τ_{wob} are the lifetimes of the jump and libration motions respectively, and,

$$S = \frac{\cos\phi_c \,(1 + \cos\phi_c)}{2} \tag{3.6}$$

The model was originally derived for the molecular re-orientation dynamics of fluorescent probes on the surface of spherical macromolecules in solution, and as such relies on some azimuthal symmetry assumptions.[50-52] Using this model to fit the $FAPbI_3$ data yields a semi-cone angle of greater than 45°, and thus a cone that extends beyond the bounds of a singular cube face, which is not plausible in the limit that the cube constrains the molecular cation motion. In part, this can be attributed to the 'V-shape' of the FA^+ cation's equilibrium geometry resulting in a loss in cation azimuthal symmetry. Furthermore, the MD simulations reveal that FA^+ does not remain centred or pivot around the centre of the inorganic cube but involves agitation around a central mean position.

Considering all these factors, the most equitable representation of the two lifetimes, without imposing assumptions about the system, was to fit the data to a biexponential decay. As such, the two resulting biexponential time constants cannot be attributed to specific nuclear motions based on the 2DIR data alone. However, due to the good agreement between time constants obtained from the 2DIR anisotropy measurements and MD simulations, the experimentally derived time constants can be assigned using the explicit motions observed in the MD simulations.

The 2DIR anisotropy measurements and MD simulations indicate that the barrier to rotational re-orientation and sampling various faces of the lead-iodide lattice must be small relative to room temperature to explain the observed decay in $R(t_2)$ towards zero within 10 ps. This means, that the FA^+ moieties are unlikely to form ferroelectric domains with phenomenologically significant lifetimes, contrary to prior experimental and theoretical studies.[1,23,30,53] These observations explain the lack of spectral diffusion observed in the isotropic 2DIR line shapes; the vibrational dipole moment associated with the C–N antisymmetric stretch will switch between adjacent and symmetric faces of a cube defined by the Pb atoms, leading to very similar intermolecular interactions. The transition

between faces requires transit through an edge or corner of the cube, however, this is so rapid that the vibrational potential is unaffected, thus explaining the minimal inhomogeneous broadening.

To the best of my knowledge, this is the first direct experimental measurement of the rotational re-orientation timescale for formamidinium cations in $FAPbI_3$; prior studies have inferred this from temperature dependent ^{15}N NMR, which has the potential to be sampling both α- and γ-$FAPbI_3$ phases,[54] or from MD calculations.[43,48] These studies put the cation re-orientation timescale between 2 and 10 ps.[43,48,54] These results indicate that the small-range motion of $FAPbI_3$ has a longer time constant than those reported for $MAPbI_3$ (300 fs), but the larger "jump-like" motion occurs with the same frequency, within error. The differing lifetimes can be attributed to a complex interplay between the molecular cation physical structure, the bending modes of the FA^+ cation, and both $–NH_2$ groups producing stronger van der Waals interactions with the inorganic lattice (and therefore a larger activation barrier to rotation) than MA^+.

The consistent "jump" lifetimes are somewhat surprising given the differing phase behaviour of $MAPbI_3$ and $FAPbI_3$. It has been proposed that the organic cation rotation in $MAPbI_3$ is mediated by coupling to low-frequency phonon modes in the inorganic lattice, specifically those associated with octahedral tilting and which contribute to $MAPbI_3$ phase transitions. From the phonon modes calculated with a DFT-PBESOL linear response based method, there are many phonon states with similar frequencies on the order of the cation rotational lifetimes (Figure 3.4), which thus supports a model in which coupling to lattice phonon modes will be also important for FA^+ reorientation in $FAPbI_3$. In addition, like MA^+ rotation in $MAPbI_3$,[12,14,55,56] these lifetimes are shorter than would be expected to facilitate the formation of sufficiently long-lived ferroelectric domains. Although, however unlikely it may seem, the possibility of entire domains undergoing concerted interconversion on these timescales cannot be excluded due to the ensemble nature of my measurements.

3.4.2. TRIR results

Time-resolved infrared (TRIR) measurements, specifically near-IR pump and mid-infrared probe, were also performed for $FAPbI_3$ thin films to investigate the role of the formamidinium cations in the conduction band, or evidence for any vibration-intraband coupling. Data from the 760 nm pump, broadband mid-infrared probe (centred at 1725 cm^-

[1]) experiments are displayed in Figure 3.17. Each TRIR spectra is dominated by two positive features; a sharp positive peak feature centred at 1718 cm^{-1}, attributed to a molecular vibration, and a broad diffuse feature that spans all probe frequencies. The latter has previously been assigned to electronic intraband transitions within the conduction band.[57,58]

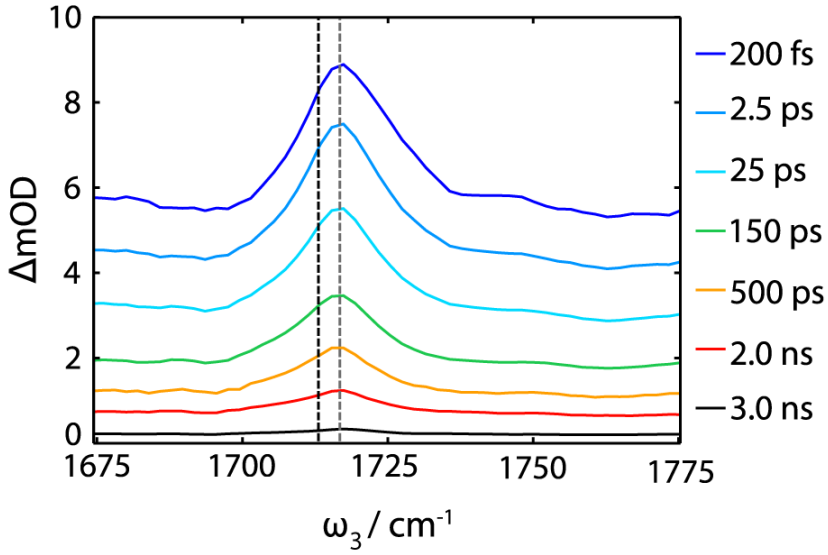

Figure 3.17: Time-resolved infrared studies for $FAPbI_3$ films using 760 nm (60 nJ) excitation and broadband mid-infrared probe for the displayed waiting times. The dashed black line marks ω_3 = 1713 cm^{-1}, the central frequency associated with the ground state FA^+ C–N antisymmetric stretching vibration; the dashed grey line helps highlight the central frequency of the transient vibrational feature (1718 cm^{-1}).

The sharp feature at 1718 cm^{-1} in the TRIR data has a similar line shape to the ground state FTIR spectrum (Figure 3.3(a)) but is blue-shifted by 5 cm^{-1}, (reminiscent of a Stark shift) and notably has one third the intensity of the intraband feature. In addition, negative features at the ground state central frequency associated with the C–N antisymmetric stretching vibration are seemingly absent from the TRIR spectra, counter to typical TRIR line shapes.

Figure 3.18(a) displays the typical line shapes expected from a vibrational Stark effect in TRIR spectroscopy for a specific t_2. The negatively signed vibrational feature (yellow line) corresponds to evolution on the ground electronic state during the waiting time. When an external field, is applied to the sample, this generates the Stark shifted vibrational transient (red line in Figure 3.18(a)), which is typically broadened relative to the unperturbed vibrational absorption spectrum, and in this instance peaks at higher frequency. The transient Stark spectrum (blue line) is the sum of these two different pathways and has the characteristic second derivative line shape.

In my TRIR experiments, 760 nm pump photons generate charge-carriers either in the form of free carriers or localized polarons.[20,26,28,29] This results in an increased internal electric field in the perovskite thin film and changes the electrostatic environment surrounding the FA^+ molecular cation, compared to the valence band ground state. This nascent field perturbs the vibrational potential associated with the C–N antisymmetric stretching FA^+ vibration, and shifts the associated fundamental frequency, *i.e.* inducing a transient vibrational Stark shift. In addition, the vibrational transition dipole moment of the C–N anti-symmetric stretch vibration in the conduction band is enhanced significantly compared to the unperturbed vibration in the valence band. Such enhanced vibrational cross-sections (termed infrared active vibrational IRAV modes) has been observed for thin polymer films, where the oscillator strength associated with vibrational transitions is enhanced by orders of magnitude, making them comparable to those typically associated with electronic transitions.[59-62] Consequentially, the positive transient feature dwarfs the negative feature in TRIR spectra (see Figure 4.18(b)).

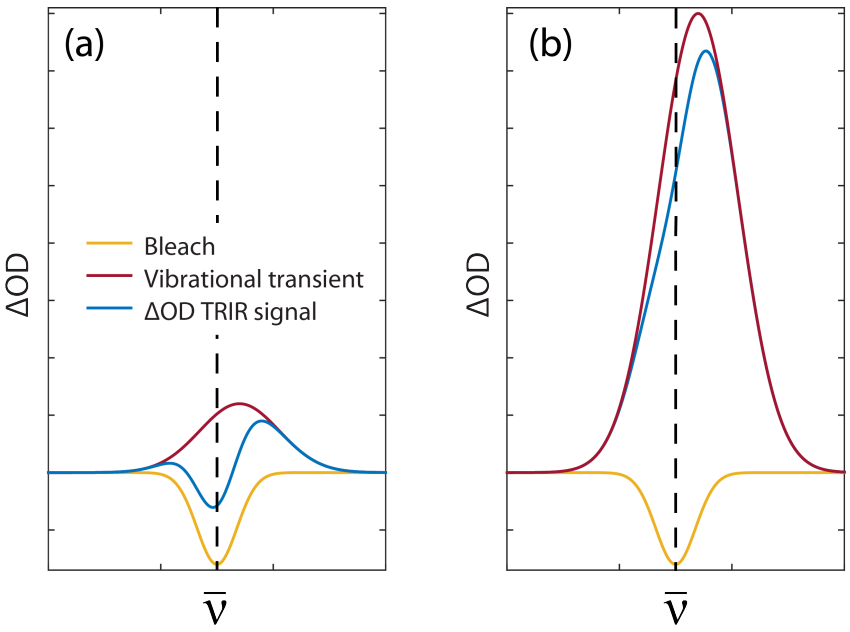

Figure 3.18: (a) Traditional vibrational Stark spectrum after ref.[63] (b) Representative components of TRIR data in the current study of $FAPbI_3$. In both panels, the black dashed line represents the central frequency of the unperturbed ground state vibration.

In prior TRIR studies of $MAPbI_3$ films using nanosecond lasers,[58] the ratios of negative and positive transient signals are comparable, and reminiscent of a second derivative transient vibrational Stark line shape (as in Figure 3.18(a)). However, this may be due to the time-delays examined, *i.e.* > 10 ns, by which time a significant amount of

charge-recombination will have occurred, leading to a reduced density of charge carriers/polarons in the film, and thus a diminished IRAV effect.

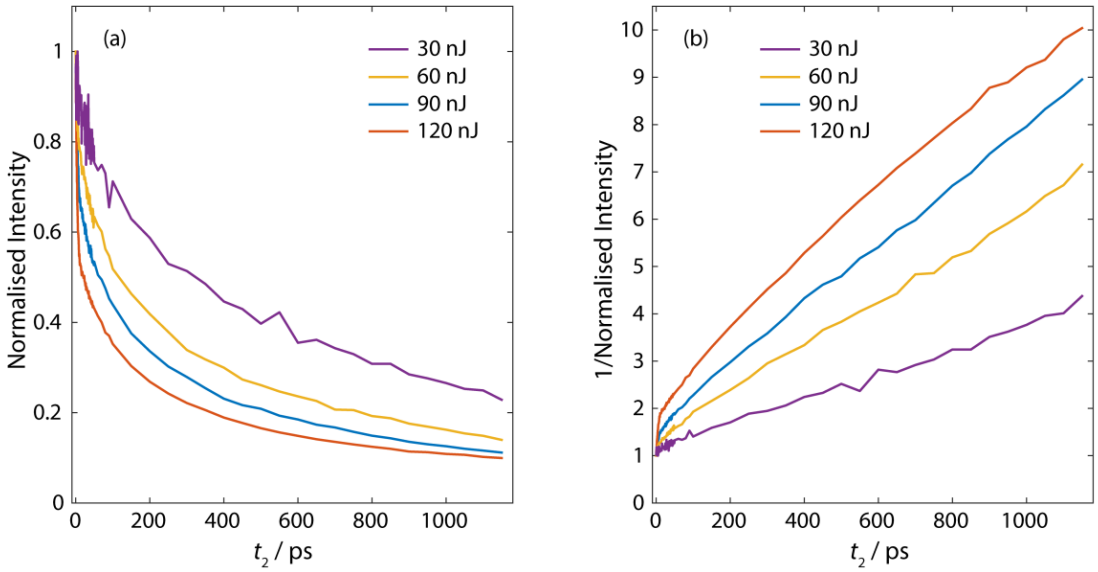

Figure 3.19: TRIR data of the response of a $FAPbI_3$ film measured with various pump powers. Left panel gives the intensity of the sharp feature at 1720 cm^{-1} associated with stark shifted C–N antisymmetric stretch peak against time and the right panel displays the same data plotting inverse intensity against time.

TRIR anisotropy experiments revealed no depolarization dynamics. Theoretical studies have demonstrated that FA^+ moieties do not participate in the Pb 6*p* ← I 5*p*/Pb 6*s* electronic transition,[64,65] and the molecular cation states do not contribute to the top of the valence or bottom of the conduction bands.[66,67] As the 2DIR results show, the FA^+ cations are not aligned in the bulk sample for any meaningful length of time. Consequentially, at t_2 = 0 fs there is no vector correlation between the electronic and vibrational transition dipole moments in question, and it is not possible to form a meaningful correlation function. One possible way to explore organic cation reorientation dynamics in the conduction band would be to perform transient-2DIR experiments.

A power-dependence TRIR study (30 – 120 nJ pump power) revealed the kinetics associated with the intraband were non-linear (Figure 3.19), as per previous investigations.[68-70] As per prior transient studies of perovskite films, the excited state lifetime is inversely proportional to the pump power density.[69] Increasing the pump fluence generates a higher charge-carriers density, which consequentially increases the probability of recombination, and thus leads to a concomitant reduction in conduction band lifetime.

3.5. Conclusions

Two-dimensional infrared spectroscopy was used to determine 470 ± 50 fs and 2.8 ± 0.5 ps time constants for the rotational reorientation timescales associated with the formamidinium cation inside $FAPbI_3$ thin films. Complementary molecular dynamics simulations relate these time constants with two FA^+ molecular motions: (i) an agitation around the centre of the inorganic lattice and (ii) a 90° jump/flip between adjacent faces of the encapsulating lead cube. The picosecond component for FA^+ is remarkably similar to the value determined for methylammonium cations inside $MAPbI_3$ thin films.[14] These results rule out the existence of long-lived (anti-)ferroelectric domains in $FAPbI_3$. Despite these similarities between cation dynamics, it is clear, interactions with the inorganic lattice greatly vary with cation, and thus influence the material's bandgap. Based on these results, the observed power conversion efficiencies, and carrier recombination rates,[1,71] of $FAPbI_3$ cannot be explained by (anti)ferroelectric domain formation, and are most likely explained by large polaron formation[28,72] or Rashba[9,73] splitting.

References

(1) Zhumekenov, A. A.; Saidaminov, M. I.; Haque, M. A.; Alarousu, E.; Sarmah, S. P.; Murali, B.; Dursun, I.; Miao, X.-H.; Abdelhady, A. L.; Wu, T.; et al. Formamidinium Lead Halide Perovskite Crystals with Unprecedented Long Carrier Dynamics and Diffusion Length. *ACS Energy Lett.* **2016**, *1* (1), 32–37.

(2) Eperon, G. E.; Stranks, S. D.; Menelaou, C.; Johnston, M. B.; Herz, L. M.; Snaith, H. J. Formamidinium Lead Trihalide: a Broadly Tunable Perovskite for Efficient Planar Heterojunction Solar Cells. *Energy Environ. Sci.* **2014**, *7* (3), 982–987.

(3) Yin, W.-J.; Shi, T.; Yan, Y. Unique Properties of Halide Perovskites as Possible Origins of the Superior Solar Cell Performance. *Adv. Mater.* **2014**, *26* (27), 4653–4658.

(4) Steirer, K. X.; Schulz, P.; Teeter, G.; Stevanovic, V.; Yang, M.; Zhu, K.; Berry, J. J. Defect Tolerance in Methylammonium Lead Triiodide Perovskite. *ACS Energy Lett.* **2016**, *1* (2), 360–366.

(5) Wehrenfennig, C.; Liu, M.; Snaith, H. J.; Johnston, M. B.; Herz, L. M. Homogeneous Emission Line Broadening in the Organo Lead Halide Perovskite $CH_3NH_3PbI_{3-X}Cl_X$. *J. Phys. Chem. Lett.* **2014**, *5* (8), 1300–1306.

(6) Saidaminov, M. I.; Adinolfi, V.; Comin, R.; Abdelhady, A. L.; Peng, W.; Dursun, I.; Yuan, M.; Hoogland, S.; Sargent, E. H.; Bakr, O. M. Planar-Integrated Single-Crystalline Perovskite Photodetectors. *Nat. Commun.* **2015**, *6*, 1–7.

(7) Stranks, S. D.; Snaith, H. J. Metal-Halide Perovskites for Photovoltaic and Light-Emitting Devices. *Nat. Rev. Mater.* **2015**, *10* (5), 391–402.

(8) Kagan, C. R.; Mitzi, D. B.; Dimitrakopoulos, C. D. Organic-Inorganic Hybrid Materials as Semiconducting Channels in Thin-Film Field-Effect Transistors. *Science* **1999**, 1–4.
(9) Kepenekian, M.; Robles, R.; Katan, C.; Sapori, D.; Pedesseau, L.; Even, J. Rashba and Dresselhaus Effects in Hybrid Organic–Inorganic Perovskites: From Basics to Devices. *ACS Nano* **2015**, *9* (12), 11557–11567.
(10) Brenner, T. M.; Egger, D. A.; Kronik, L.; Hodes, G.; Cahen, D. Hybrid Organic-Inorganic Perovskites: Low- Cost Semiconductors with Intriguing Charge-Transport Properties. *Nat. Rev. Mater.* **2016**, 1–16.
(11) Ponseca, C. S., Jr.; Savenije, T. J.; Abdellah, M.; Zheng, K.; Yartsev, A.; Pascher, T.; Harlang, T.; Chabera, P.; Pullerits, T.; Stepanov, A.; et al. Organometal Halide Perovskite Solar Cell Materials Rationalized: Ultrafast Charge Generation, High and Microsecond-Long Balanced Mobilities, and Slow Recombination. *J. Am. Chem. Soc.* **2014**, *136* (14), 5189–5192.
(12) Selig, O.; Sadhanala, A.; Müller, C.; Lovrincic, R.; Chen, Z.; Rezus, Y. L. A.; Frost, J. M.; Jansen, T. L. C.; Bakulin, A. A. Organic Cation Rotation and Immobilization in Pure and Mixed Methylammonium Lead-Halide Perovskites. *J. Am. Chem. Soc.* **2017**, *139* (11), 4068–4074.
(13) Frost, J. M.; Whalley, L. D.; Walsh, A. Slow Cooling of Hot Polarons in Halide Perovskite Solar Cells. *ACS Energy Lett.* **2017**, 2647–2652.
(14) Bakulin, A. A.; Selig, O.; Bakker, H. J.; Rezus, Y. L. A.; Müller, C.; Glaser, T.; Lovrincic, R.; Sun, Z.; Chen, Z.; Walsh, A.; et al. Real-Time Observation of Organic Cation Reorientation in Methylammonium Lead Iodide Perovskites. *J. Phys. Chem. Lett.* **2015**, *6* (18), 3663–3669.
(15) Leguy, A. M. A.; Goñi, A. R.; Frost, J. M.; Skelton, J.; Brivio, F.; Rodríguez-Martínez, X.; Weber, O. J.; Pallipurath, A.; Alonso, M. I.; Campoy-Quiles, M.; et al. Dynamic Disorder, Phonon Lifetimes, and the Assignment of Modes to the Vibrational Spectra of Methylammonium Lead Halide Perovskites. *Phys. Chem. Chem. Phys.* **2016**, *18* (39), 27051–27066.
(16) Park, M.; Kornienko, N.; Reyes-Lillo, S. E.; Lai, M.; Neaton, J. B.; Yang, P.; Mathies, R. A. Critical Role of Methylammonium Librational Motion in Methylammonium Lead Iodide ($CH_3NH_3PbI_3$) Perovskite Photochemistry. *Nano Lett.* **2017**, *17* (7), 4151–4157.
(17) Beecher, A. N.; Semonin, O. E.; Skelton, J. M.; Frost, J. M.; Terban, M. W.; Zhai, H.; Alatas, A.; Owen, J. S.; Walsh, A.; Billinge, S. J. L. Direct Observation of Dynamic Symmetry Breaking Above Room Temperature in Methylammonium Lead Iodide Perovskite. *ACS Energy Lett.* **2016**, *1* (4), 880–887.
(18) Haruyama, J.; Sodeyama, K.; Han, L.; Tateyama, Y. First-Principles Study of Ion Diffusion in Perovskite Solar Cell Sensitizers. *J. Am. Chem. Soc.* **2015**, *137* (32), 10048–10051.
(19) Leguy, A. M. A.; Frost, J. M.; McMahon, A. P.; Sakai, V. G.; Kochelmann, W.; Law, C.; Li, X.; Foglia, F.; Walsh, A.; Regan, B. C. O. R.; et al. The Dynamics of Methylammonium Ions in Hybrid Organic-Inorganic Perovskite Solar Cells. *Nat. Commun.* **2015**, *6*, 1–10.
(20) Zhu, X. Y.; Podzorov, V. Charge Carriers in Hybrid Organic–Inorganic Lead Halide Perovskites Might Be Protected as Large Polarons. *J. Phys. Chem. Lett.* **2015**, *6* (23), 4758–4761.

(21) Lee, J.-H.; Bristowe, N. C.; Lee, J. H.; Lee, S.-H.; Bristowe, P. D.; Cheetham, A. K.; Jang, H. M. Resolving the Physical Origin of Octahedral Tilting in Halide Perovskites. *Chem. Mater.* **2016**, *28* (12), 4259–4266.

(22) Motta, C.; El-Mellouhi, F.; Kais, S.; Tabet, N.; Alharbi, F.; Sanvito, S. Revealing the Role of Organic Cations in Hybrid Halide Perovskite $CH_3NH_3PbI_3$. *Nat. Commun.* **2015**, *6* (1), 1–7.

(23) Frost, J. M.; Walsh, A. What Is Moving in Hybrid Halide Perovskite Solar Cells? *Acc. Chem. Res.* **2016**, *49* (3), 528–535.

(24) Filip, M. R.; Eperon, G. E.; Snaith, H. J.; Giustino, F. Steric Engineering of Metal-Halide Perovskites with Tunable Optical Band Gaps. *Nat. Commun.* **2014**, *5*, 1–9.

(25) Green, M. A.; Jiang, Y.; Soufiani, A. M.; Ho-Baillie, A. Optical Properties of Photovoltaic Organic–Inorganic Lead Halide Perovskites. *J. Phys. Chem. Lett.* **2015**, *6* (23), 4774–4785.

(26) Amat, A.; Mosconi, E.; Ronca, E.; Quarti, C.; Umari, P.; Nazeeruddin, M. K.; Grätzel, M.; De Angelis, F. Cation-Induced Band-Gap Tuning in Organohalide Perovskites: Interplay of Spin–Orbit Coupling and Octahedra Tilting. *Nano Lett.* **2014**, *14* (6), 3608–3616.

(27) Frost, J. M.; Butler, K. T.; Brivio, F.; Hendon, C. H.; van Schilfgaarde, M.; Walsh, A. Atomistic Origins of High-Performance in Hybrid Halide Perovskite Solar Cells. *Nano Lett.* **2014**, *14* (5), 2584–2590.

(28) Neukirch, A. J.; Nie, W.; Blancon, J.-C.; Appavoo, K.; Tsai, H.; Sfeir, M. Y.; Katan, C.; Pedesseau, L.; Even, J.; Crochet, J. J.; et al. Polaron Stabilization by Cooperative Lattice Distortion and Cation Rotations in Hybrid Perovskite Materials. *Nano Lett.* **2016**, *16* (6), 3809–3816.

(29) Wright, A. D.; Verdi, C.; Milot, R. L.; Eperon, G. E.; rez-Osorio, M. A. P. E.; Snaith, H. J.; Giustino, F.; Johnston, M. B.; Herz, L. M. Electron-Phonon Coupling in Hybrid Lead Halide Perovskites. *Nat. Commun.* **2016**, *7*, 1–9.

(30) Quarti, C.; Mosconi, E.; De Angelis, F. Structural and Electronic Properties of Organo-Halide Hybrid Perovskites From Ab Initio Molecular Dynamics. *Phys. Chem. Chem. Phys.* **2015**, *17*, 9394–9409.

(31) Liu, S.; Zheng, F.; Koocher, N. Z.; Takenaka, H.; Wang, F.; Rappe, A. M. Ferroelectric Domain Wall Induced Band Gap Reduction and Charge Separation in Organometal Halide Perovskites. *J. Phys. Chem. Lett.* **2015**, *6* (4), 693–699.

(32) Galkowski, K.; Mitioglu, A.; Miyata, A.; Plochocka, P.; Portugall, O.; Eperon, G. E.; Wang, J. T.-W.; Stergiopoulos, T.; Stranks, S. D.; Snaith, H. J.; et al. Determination of the Exciton Binding Energy and Effective Masses for Methylammonium and Formamidinium Lead Tri-Halide Perovskite Semiconductors. *Energy Environ. Sci.* **2016**, *9*, 962–970.

(33) Greetham, G. M.; Donaldson, P. M.; Nation, C.; Sazanovich, I. V.; Clark, I. P.; Shaw, D. J.; Parker, A. W.; Towrie, M. A 100 kHz Time-Resolved Multiple-Probe Femtosecond to Second Infrared Absorption Spectrometer. *Applied Spectroscopy* **2016**, *70* (4), 645–653.

(34) Donaldson, P. M.; Towrie, M.; Parker, A. W.; Greetham, G. M.; Shaw, D. J. A 100 kHz Pulse Shaping 2D-IR Spectrometer Based on Dual Yb:KGW Amplifiers. *J. Phys. Chem.* **2017**, 122 (3), 780-787

(35) Röttger, K.; Marroux, H. J. B.; Chemin, A. F. M.; Elsdon, E.; Oliver, T. A. A.; Street, S. T. G.; Henderson, A. S.; Galan, M. C.; Orr-Ewing, A. J.; Roberts, G. M. Is UV-Induced Electron-Driven Proton Transfer Active in a Chemically Modified a·T DNA Base Pair? *J. Phys. Chem. B* **2017**, *121* (17), 4448–4455.

(36) Zhou, Z.; Pang, S.; Ji, F.; Zhang, B.; Cui, G. The Fabrication of Formamidinium Lead Iodide Perovskite Thin Films via Organic Cation Exchange. *Chem. Commun.* **2016**, *52*, 3828–3831.
(37) Hills-Kimball, K.; Nagaoka, Y.; Cao, C.; Chaykovsky, E.; Chen, O. Synthesis of Formamidinium Lead Halide Perovskite Nanocrystals Through Solid–Liquid–Solid Cation Exchange. *J. Mater. Chem. C,* **2017**, *5* (23), 5680–5684.
(38) Werner, H. J.; Knowles, P. J.; Knizia, G.; Manby, F. R.; Schütz, M.; Celani, P.; Györffy, W.; Kats, D.; Korona, T.; Lindh, R.; et al. MOLPRO - a Package of *Ab Initio* Programs. *WIREs Comput. Mol. Sci.*, **2012**, 2, 242-253
(39) Alecu, I. M.; Zheng, J.; Zhao, Y.; Truhlar, D. G. Computational Thermochemistry: Scale Factor Databases and Scale Factors for Vibrational Frequencies Obtained From Electronic Model Chemistries. *J. Chem. Theory Comput.* **2010**, *6* (9), 2872–2887.
(40) Herzberg, G. *Molecular Spectra and Molecular Structure. Vol. 2: Infrared and Raman Spectra of Polyatomic Molecules*; New York : Van Nostrand , Reinhold; Vol. 2., 1939
(41) Clark, S. J.; Segall, M. D.; Pickard, C. J.; Hasnip, P. J.; Probert, M. I. J.; Refson, K.; Payne, M. C. First Principles Methods Using CASTEP. *Zeitschrift für Kristallographie - Crystalline Materials* **2005**, *220* (5/6), 191.
(42) Mattoni, A.; Filippetti, A.; Saba, M. I.; Delugas, P. Methylammonium Rotational Dynamics in Lead Halide Perovskite by Classical Molecular Dynamics: the Role of Temperature. *J. Phys. Chem. C* **2015**, *119* (30), 17421–17428.
(43) Weller, M. T.; Weber, O. J.; Frost, J. M.; Walsh, A. Cubic Perovskite Structure of Black Formamidinium Lead Iodide, α-$[HC(NH_2)_2]PbI_3$, At 298 K. *J. Phys. Chem. Lett.* **2015**, *6* (16), 3209–3212.
(44) De Lathauwer, L.; De Moor, B.; Vandewalle, J. A Multilinear Singular Value Decomposition. *SIAM J. Matrix Anal. Appl.* **2000**, *21* (4), 1253–1278.
(45) Vervliet, N.; Debals, O.; Sorber, L.; Van Barel, M.; De Lathauwer, L. Tensorlab 3.0. Available online, March 2016, URL: https://www.tensorlab.net/.
(46) Guo, Q.; Pagano, P.; Li, Y.-L.; Kohen, A.; Cheatum, C. M. Line Shape Analysis of Two-Dimensional Infrared Spectra. *J. Phys. Chem.* **2015**, *142* (21), 212427–14.
(47) Christians, J. A.; Miranda Herrera, P. A.; Kamat, P. V. Transformation of the Excited State and Photovoltaic Efficiency of $CH_3NH_3PbI_3$ Perovskite Upon Controlled Exposure to Humidified Air. *J. Am. Chem. Soc.* **2015**, *137* (4), 1530–1538.
(48) Carignano, M. A.; Saeed, Y.; Aravindh, S. A.; Roqan, I. S.; Even, J.; Katan, C. A Close Examination of the Structure and Dynamics of $HC(NH_2)_2PbI_3$ By MD Simulations and Group Theory. *Phys. Chem. Chem. Phys.* **2016**, *18*, 27109–27118.
(49) Weller, M. T.; Weber, O. J.; Henry, P. F.; Di Pumpo, A. M.; Hansen, T. C. Complete Structure and Cation Orientation in the Perovskite Photovoltaic Methylammonium Lead Iodide Between 100 and 352 K. *Chem. Commun.* **2015**, *51*, 4180–4183.
(50) Lipari, G.; Szabo, A. Effect of Librational Motion on Fluorescence Depolarization and Nuclear Magnetic Resonance Relaxation in Macromolecules and Membranes. *Biophys. J.* **1980**, *30* (3), 489–506.
(51) Ji, M.; Gaffney, K. J. Orientational Relaxation Dynamics in Aqueous Ionic Solution: Polarization-Selective Two-Dimensional Infrared Study of Angular

Jump-Exchange Dynamics in Aqueous 6M NaClO 4. *J. Phys. Chem.* **2011**, *134* (4), 044516–14.

(52) Kwak, K.; Park, S.; Finkelstein, I. J.; Fayer, M. D. Frequency-Frequency Correlation Functions and Apodization in Two-Dimensional Infrared Vibrational Echo Spectroscopy: a New Approach. *J. Phys. Chem.* **2007**, *127* (12), 124503–124518.

(53) Walsh, A. Principles of Chemical Bonding and Band Gap Engineering in Hybrid Organic–Inorganic Halide Perovskites. *J. Phys. Chem. C* **2015**, *119* (11), 5755–5760.

(54) Kubicki, D. J.; Prochowicz, D.; Hofstetter, A.; Zakeeruddin, S. M.; Grätzel, M.; Emsley, L. Phase Segregation in Cs-, Rb- and K-Doped Mixed-Cation (MA) X(FA) 1– xPbI 3Hybrid Perovskites From Solid-State NMR. *J. Am. Chem. Soc.* **2017**, *139* (40), 14173–14180.

(55) Zhu, H.; Miyata, K.; Fu, Y.; Wang, J.; Joshi, P. P.; Niesner, D.; Williams, K. W.; Jin, S.; Zhu, X. Y. Screening in Crystalline Liquids Protects Energetic Carriers in Hybrid Perovskites. *Science* **2016**, *353* (6306), 1409–1413.

(56) Gélvez-Rueda, M. C.; Cao, D. H.; Patwardhan, S.; Renaud, N.; Stoumpos, C. C.; Schatz, G. C.; Hupp, J. T.; Farha, O. K.; Savenije, T. J.; Kanatzidis, M. G.; et al. Effect of Cation Rotation on Charge Dynamics in Hybrid Lead Halide Perovskites. *J. Phys. Chem. C* **2016**, *120* (30), 16577–16585.

(57) Sauvage, S.; Boucaud, P.; Julien, F. H.; Gérard, J. M.; Marzin, J. Y. Infrared Spectroscopy of Intraband Transitions in Self-Organized InAs/GaAs Quantum Dots. *J. Appl. Phys.* **1997**, *82* (7), 3396–3401.

(58) Narra, S.; Chung, C.-C.; Diau, E. W.-G.; Shigeto, S. Simultaneous Observation of an Intraband Transition and Distinct Transient Species in the Infrared Region for Perovskite Solar Cells. *J. Phys. Chem. Lett.* **2016**, *7* (13), 2450–2455.

(59) Heeger, A. J.; Kivelson, S.; Schrieffer, J. R.; Su, W. P. Solitons in Conducting Polymers. *Rev. Mod. Phys.* **1988**, *60* (3), 781–850.

(60) Miranda, P. B.; Moses, D.; Heeger, A. J. Ultrafast Photogeneration of Charged Polarons in Conjugated Polymers. *Phys. Rev. B* **2001**, *64* (8), 1182–1184.

(61) Sakamoto, A.; Nakamura, O.; Tasumi, M. Picosecond Time-Resolved Polarized Infrared Spectroscopic Study of Photoexcited States and Their Dynamics in Oriented Poly(P-Phenylenevinylene). *J. Phys. Chem. B* **2008**, *112* (51), 16437–16444.

(62) Chin, X. Y.; Yin, J.; Wang, Z.; Caironi, M.; Soci, C. Mapping Polarons in Polymer FETs by Charge Modulation Microscopy in the Mid-Infrared. *Sci. Rep.* **2014**, *4*, 839–6.

(63) Boxer, S. G. Stark Realities. *J. Phys. Chem. B* **2009**, *113* (10), 2972–2983.

(64) Kim, J.; Lee, S.-C.; Lee, S.-H.; Hong, K.-H. Importance of Orbital Interactions in Determining Electronic Band Structures of Organo-Lead Iodide. *J. Phys. Chem. C* **2015**, *119* (9), 4627–4634.

(65) Ma, J.; Wang, L.-W. Nanoscale Charge Localization Induced by Random Orientations of Organic Molecules in Hybrid Perovskite $CH_3NH_3PbI_3$. *Nano Lett.* **2015**, *15* (1), 248–253.

(66) Borriello, I.; Cantele, G.; Ninno, D. Ab Initioinvestigation of Hybrid Organic-Inorganic Perovskites Based on Tin Halides. *Phys. Rev. B* **2008**, *77* (23), 29–29.

(67) Brivio, F.; Walker, A. B.; Walsh, A. Structural and Electronic Properties of Hybrid Perovskites for High-Efficiency Thin-Film Photovoltaics From First-Principles. *APL Materials* **2013**, *1* (4), 042111–042116.

(68) Piatkowski, P.; Cohen, B.; Kazim, S.; Ahmad, S.; Douhal, A. How Photon Pump Fluence Changes the Charge Carrier Relaxation Mechanism in an Organic-Inorganic Hybrid Lead Triiodide Perovskite. *Phys. Chem. Chem. Phys.* **2016**, *18*, 27090–27101.

(69) Manser, J. S.; Kamat, P. V. Band Filling with Free Charge Carriers in Organonietal Halide Perovskites. *Nat. Photonics* **2014**, *8* (9), 737–743.

(70) Kudriashova, L. G.; Kiermasch, D.; Rieder, P.; Campbell, M.; Tvingstedt, K.; Baumann, A.; Astakhov, G. V.; Dyakonov, V. Impact of Interfaces and Laser Repetition Rate on Photocarrier Dynamics in Lead Halide Perovskites. *J. Phys. Chem. Lett.* **2017**, *8* (19), 4698–4703.

(71) Han, Q.; Bae, S.-H.; Sun, P.; Hsieh, Y.-T.; Yang, Y. M.; Rim, Y. S.; Zhao, H.; Chen, Q.; Shi, W.; Li, G.; et al. Single Crystal Formamidinium Lead Iodide (FAPbI 3): Insight Into the Structural, Optical, and Electrical Properties. *Adv. Mater.* **2016**, *28* (11), 2253–2258.

(72) Sendner, M.; Nayak, P. K.; Egger, D. A.; Beck, S.; ller, C. M. X.; Epding, B.; Kowalsky, W.; Kronik, L.; Snaith, H. J.; Pucci, A.; et al. Optical Phonons in Methylammonium Lead Halide Perovskites and Implications for Charge Transport. *Mater. Horizons* **2016**, *3*, 613–620.

(73) Etienne, T.; Mosconi, E.; De Angelis, F. Dynamical Origin of the Rashba Effect in Organohalide Lead Perovskites: a Key to Suppressed Carrier Recombination in Perovskite Solar Cells? *J. Phys. Chem. Lett.* **2016**, *7* (9), 1638–1645.

Chapter 4. Ultrafast Transient Absorption Microscopy

4.1. Introduction

All of the results discussed thus far in my thesis have been bulk measurements, meaning the signal is collected from a macroscopic (~100s μm) region of the sample, as determined by the pump-probe focal volume. Therefore, any variation in the species' responses from within this volume are averaged in such measurements. In solid state samples, the non-linear responses from within this probed volume can vary drastically due to static nanometre- or micron- scale structure within the sample. Therefore, due to the spatial-averaging nature of bulk transient absorption measurements, information about the sub-ensemble is obscured, and in some instances entirely masked. Transient absorption microscopy (TAM), also referred to as pump-probe microscopy, enables correlation between the non-linear signal and a spatial position within the sample by performing the spectroscopic measurement through a microscope.

If the source of a non-linear response is unknown, the ability to correlate the signal with a morphological feature or structure provides an obvious advantage. However, the potential value of TAM measurements extends far beyond this simple case. Examples where spatially resolving the origin of non-linear signals can provide further insight into the dynamic of the sample include:

1. To isolate the signal from an individual structure or chromophore, such as a single nanoparticle
2. To track the trajectory of charges through a sample or structure
3. To investigate how nanometre-to-micron morphology affects the electronic structure (and even function) of microscopic parts of material.

The first case is particularly relevant to nanomaterials because unlike molecular species the size and shape of nanomaterials can determine their spectral response, for example the hollow gold nanoshells discussed in the chapter 2 of my thesis. Rather than requiring a sample of purely monodisperse nanoparticles (which is extremely challenging to synthesise) it is far simpler to measure the response of individual nanostructures and characterise the properties of the specific nanostructure. This approach has been used to characterise the individual responses of a variety of nanomaterials[1-3] including solid gold

nanoparticles,[4] hollow gold nanoparticles, silver nanowires[5], Bismuth vanadate crystallites,[6] or cadmium telluride nanowires,[7] to name but a few.

The spatial resolution of TAM is limited by the diffraction limit of the wavelengths used in the measurement (see section 4.2). In the TAM experiments discussed in this chapter, the spatial resolution was on the order of hundreds of nanometres, and so my measurements were unable to resolve nanoscale detail smaller than this. Because of the diffraction limit, higher resolution techniques such as atomic force microscopy or electron microscopy are often used to complement TAM measurements and acquire higher resolution images of the structures prior to time-resolved measurements. For example, Gao *et al.* used patterned substrates to ensure the same metallic single-walled carbon nanotube could be located using atomic force microscopy and TAM.[8]

The second example of how TAM can be used to track the flow of energy or charge through a sample is typically achieved by exciting a small region of the sample with the pump pulse, and monitoring the response over a larger region with the probe. Such a technique can monitor the flow of energy through the material emanating from a well-defined volume. This could be the transfer/migration of photogenerated excitons, free charge carriers, or polaritons. For example, this method has been used to monitor the charge recombination dynamics in a single zinc oxide nanoscale rod[9], the exciton population dynamics in a thin film of pentacene[10], phonon propagation in germanium nanowires,[11] the long-range transport of cavity polaritons in organic films[12] and to watch the ballistic propagation of charge carriers through methylammonium perovskite thin films, [13] and their long-range transport. [14]

The third case listed above is perhaps the most subtle. In this case it is not the individual nanostructures themselves that are paramount, rather their proximity to and effect upon each other. For example, Simpson *et al.* used TAM combined with spatially resolved photoluminescence to investigate the locations of trap states within perovskite thin films and found distinct regions with high and low densities of trapped charges. [15,16] Additionally, TAM studies of P3HT:PCBM bulk heterojunctions have revealed greatly varying dynamics according to proximity to domain boundaries. [17,18] One last example is the study of morphology dependent carrier cooling in perovskite crystals. [19]

In this chapter efforts to build a TAM experimental apparatus and investigate charge carrier generation and dynamics in a bulk heterojunction (BHJ) film are detailed. Since there has been little discussion of microscopy techniques thus far in my thesis, in the

following section I will outline some of the key microscopy aspects of TAM as a non-linear microscopy technique.

4.2. Microscopy

Diffractive optics are inherently limited in their ability to focus light to a point and, conversely, to locate a point source of light. When focusing light from a point source with a diffraction limited lens, the resulting image forms 'Airy disk' patterns which consist of a bright central spot surrounded by concentric bright and dark rings as illustrated in Figure 4.1. [20] A corollary of the diffraction limit is a limit to the resolution of linear microscopy based on diffractive optics. Resolution describes the ability to distinguish between two separate objects (or point sources) in an image. There are several ways in which resolution can be defined. For a sample in the *x*-*y* plane that is illuminated by light travelling perpendicular to this 2D plane, the *z*-direction, (as defined in Figure 4.1), the Abbe resolution for linear microscopy is given by:

$$Abbe\ Resolution_{xy} = \frac{\lambda}{2NA} \tag{4.1}$$

$$Abbe\ Resolution_{z} = \frac{2\lambda}{NA^2} \tag{4.2}$$

Where λ is the wavelength of the light and *NA* is the numerical aperture of the objective lens. The numerical aperture is used as a measure of the resolving ability of a microscope objective lens and is defined as:

$$NA = n \sin\theta \tag{4.3}$$

Where θ is the semi-cone angle at which the lens can collect light and n is the refractive index of the medium between the lens and sample. Oil or water immersion lenses increase the *NA* of a lens by using liquids with higher refractive index than air and can therefore render an improved diffraction limited resolution (equations 4.1 and 4.2).

The diffraction limit is an imperative part of optical microscopy; however, many microscopy techniques have been developed to achieve sub-diffraction limit spatial resolution. One such example is non-linear microscopy. Non-linear microscopy is a well-established and expansive field that encompasses many different techniques. The defining feature of non-linear microscopy is that it uses non-linear optical process to afford

improved resolution or contrast in microscopy measurements. [21] TAM is a non-linear microscopy technique since it is only sensitive to third order non-linear signals. Subsequently, under the right conditions, TAM measurements have the capability to achieve sub-diffraction limit resolution.

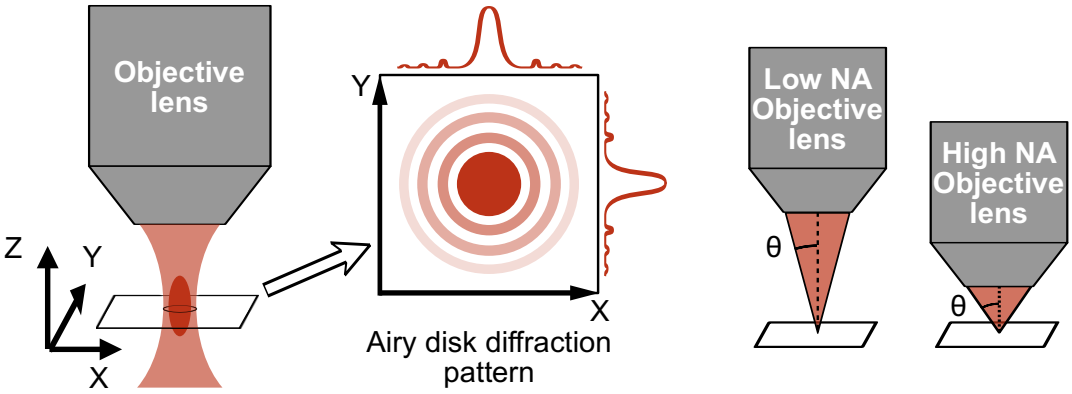

Figure 4.1: Airy disk diffraction pattern and semi-cone angle of high and low NA objective lenses.

In non-linear microscopy techniques, signals can only be generated in volumes with sufficiently strong electric field strengths. In the case of TAM, this is the product of the fields from the pump and probe pulses, which leads to an additional advantage; if the pump and probe are at different wavelengths the resolution is determined by whichever pulse has the shortest wavelength. As per equations 4.1 and 4.2 it is apparent that the diffraction limit is smaller for shorter wavelengths of light, however, the disadvantage is that shorter wavelengths will likely be more strongly scattered, and thus reducing the signal-to-noise ratio. Therefore, having the resolution determined by a shorter pump wavelength but the signal produced at a longer probe wavelength is an ideal situation and allows removal of residual pump light using dichroic filters. Indeed, it has even been suggested that TAM could be useful for studying biological samples, since the time-resolved response of the sample could provide a way to improve specificity in microscopy without use of exogenous dyes.[16,17]

Resolution in the *z*-plane (equation 4.2) is unavoidably worse than the lateral resolution (see equation 4.1) in linear microscopy. 2-photon fluorescence microscopy has the long-known advantage of non-linear absorption to improve the *z*-resolution of images. [22] As shown in Figure 4.1, the density of photons increases as light reaches the focal plane. At the focal plane, the density of light is so high that two-photon absorption can occur, but critically, two-photon absorption is negligible outside of the focal plane which therefore

generates no fluorescence. The same principle is true for TAM in the z-plane, as the pump-probe signal is proportional to the third-order non-linear polarisation. [21]

In regions above or below the focal spot, out of focus light will scatter off the sample which, for thick samples, can add additional unwanted noise to signals. This issue led to the development of confocal microscopy, where a pair of pinholes (often the apertures of microscope objective lenses used to focus and collect light from the sample) minimise the amount of light scattered outside the focal plane reaching the detector. Despite this potential for TAM to surpass the diffraction limit, in most spectroscopy-based studies the resolution of images is generally described as close to or at the diffraction limit.

In the following sections two types of microscopy will be discussed; widefield and point scanning microscopy. In widefield microscopy a large region of the sample is illuminated at once and the entire image is acquired. In contrast in point scanning techniques (for example confocal) light is only collected from a small region of the sample at a time in the form of individual points or pixels, which are acquired in rapid succession until the entire image is constructed. Under the right conditions point scanning techniques such as confocal can generate higher resolution images than widefield imaging. Most of the experiments discussed herein use point scanning imaging.

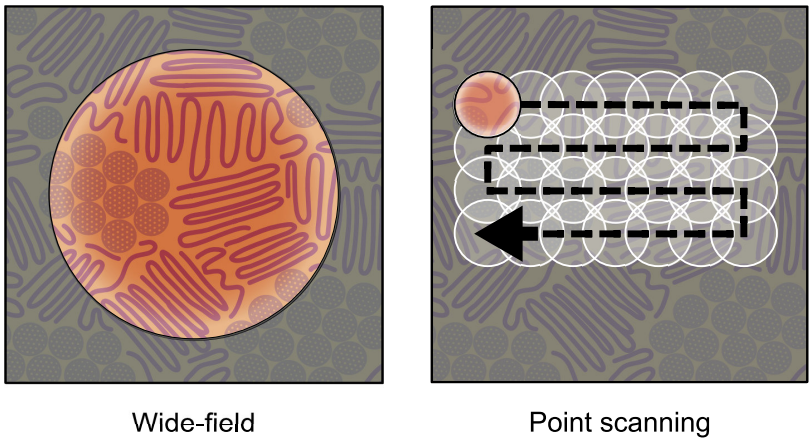

Figure 4.2: Schematic illustration of two methods of image acquisition: wide-field and point-scanning.

To achieve point scanning imaging either the sample must be moved through the focus or the focus has to be moved over the sample. Generally piezo-electric stages facilitate the former option, and galvanometric scanning mirrors are used for the latter. Both approaches can achieve diffraction limit precision and each offer different

advantages. Scanning mirrors reduce the possibility of drift in the position of the sample and the overall microscope, since the only moving parts are two mirrors which are actively positioned. Further, they can be used to move the pump and probe beams independently, opening up the important ability to monitor sample kinetics with respect to the distance from the localised pump beam (as discussed later). Unfortunately, the scanning range of these mirrors is limited to a few microns.

In point scanning techniques the acquisition time for each pixel is referred to as the pixel dwell time. The total time required to acquire an image depends on the pixel dwell time, the time required to move between pixels, and total number of pixels. The resolution of images can be improved by acquiring a higher density of pixels per unit area of the sample, but obviously the spatial resolution cannot surpass the fundamental diffraction limit.

4.3. TAM Design Considerations

There have been several reviews of TAM[1,21,23-29] showcasing a significant number of studies, despite only a relatively small number of groups possessing such experimental capabilities. However, there has been a recent surge of groups moving towards transient microscopy measurements. Some recent examples include the demonstration and utilisation of two-dimensional optical spectroscopy combined with confocal microscopy (2DIR[30,31] and 2D electronic spectroscopy[32,33]), and pump-probe super-resolution microscopy techniques such as stimulated emission depletion (STED)[34,35] and near-field scanning optical microscopy (NSOM).[36,37] The following discussion will be limited to experiments using pump-probe or TA (narrowband pump with broadband or narrowband probe) spectroscopic techniques integrated with near- and far-field microscopy imaging. I will refer to these measurements as TAM experiments to distinguish from other nonlinear time-resolved microscopy techniques.

Table 4.1 details some of the key aspects associated with existing TAM experiments by groups around the world. One of the most important distinctions between reported set-ups is the repetition rate of the laser used, as this can have repercussions in several other aspects of the experimental design. The majority of set-ups use MHz frequency repetition-rates (typically 80 MHz Ti:Sapphire lasers) that generate narrowband pump and probe pulses of different frequencies, so called two colour pump-probe experiments. These pulses are both focussed into the sample and collected by microscope

objective lenses. After the sample residual pump light is removed with dichroic mirrors or high-contrast filters. In the pump-probe geometry, the signal is 'self-heterodyned' by the collinear probe pulse and both are detected on a single-element avalanche photodiode or photomultiplier tube detector. The signal is extracted with a lock-in amplifier. Lock-in amplifiers can detect periodic changes in signal with high sensitivity up to 100s of MHz rates. By 'locking-into' the frequency the pump is modulated at, they can be used to detect the change in absorption of the sample due to excitation by the pump (ΔA). In MHz TAM experiments, the pump beam is typically modulated by an acousto-optic modulator (AOM).

Alternatively, some groups have used kHz repetition rate lasers (see Table 4.1) including broadband white light supercontinuum (WL) probes. White light supercontinuum probes are clearly advantageous over narrowband probes, and they revolutionised pump-probe spectroscopy by facilitating great insights into the broadband spectral response of samples.[38] Use of white light continuum probes typically limit experiments to kHz acquisition rates for two reasons: generation of a white light continuum with MHz repetition rates, and correspondingly low peak power pulses, is technically challenging and is typically achieved inside fibres. The resulting pulses are temporally very long and difficult to compress. Secondly, the electronics and digitisation of linear array detectors are typically limited to kHz repetition rates. The use of a broadband probe also has important implications on the optics inside the microscope. Chromatic aberration poses a challenge associated with the wavelength dependence on the focal plane, which can lead to preferential selection of signal from certain frequencies. Although achromatic lenses have coatings to reduce such effects, these coatings are effective over a limited wavelength range, and achromatic microscope objectives are significantly more expensive. For these reasons, Schnerdermann *et al.* used a curved silver mirror to focus the pump and probe into the sample.[39] The use of curved mirrors provides a chromatic aberration free method of focusing light and applies no temporal chirp to the pulse. Unfortunately, focusing mirrors are unable to achieve the diffraction-limited focal-spot sizes attained with high NA objectives. So, in order to maintain high spatial resolution Schnerdermann *et al.* used an achromatic microscope collection objective. As this was after the sample the achromatic effects were less significant and temporal chirp is not an issue.

Table 4.1: Experimental details from a selection of TAM studies

Group	Reference	Laser repetition rate	Focusing optics	Pump modulation	Imaging system	Wavelengths and Detection	Pump and probe powers	Sample
Gregory Hartland[40]	Devkota, T., *et al.* (2019). *J. Appl. Phys.*, ***125**, 163102*	80 MHz	Reflection measurement: variety of microscope objectives with 0.1 – 1.3 NA	AOM at 400 kHz,	Not stated	2 colour pump/probe APD & lock-in amplifier	120 μW pump and 80 μW probe	Acoustic waves in gold nanostripes
Libai Huang[18]	Wong, C. T. O., et al. (2012). *J. Phys. Chem. Lett.*, *3*(7), 879–884.	80 MHz pulse picked down to 5 MHz	40x magnification Focused with a 0.65 NA objective. Collected by 0.6 NA lens	AOM at 500 kHz	Raster scanning piezo sample stage	2 colour pump/probe APD & lock-in amplifier	6 μJ cm^{-2} pump. Probe power not stated	P3HT:PCBM BHJ
Warren S. Warren[41]	Fu, D., *et al.* (2007). *J. Biomed. Optics*, *12*(5), 054004–8.	80 MHz pulse picked down to 5 MHz	50x magnification Focused into sample with a 0.55 NA objective lens	AOM modulating at 10 MHz	Scanning mirror	2 colour pump/probe Photodiode & lock-in amplifier	2 mW pump at 775 nm and 1 mW probe at 650 nm	B16 mouse melanoma cells
John M. Papanikolas[11]	Van Goethem, E. M., *et al.* (2019). *ACS Photonics*, 1–10.	80 MHz reduced to 1.6 MHz with two pulse picking AOMs	100x magnification Focused with a 0.8 NA microscope objective and collected with a high NA objective lens	16 kHz, (presumably by one of the pulse picking AOMs)	Scanning mirrors and XY piezo scanning stage	2 colour pump/probe Balanced photodiode and lock-in amplifier	10 pJ/pulse pump and 4 pJ/pulse probe,	Phonon Propagation in Germanium Nanowires

Ying-Zhong Ma[42]	Simpson, M. J., *et al.* (2015). *J. Phys. Chem. Lett.*, *6*(15), 3041–3047.	250 kHz	focused using a 40x, 0.72 NA objective and collected using a 2x, 0.06 NA objective	Chopper driven at 688 Hz	Scanning a motor-driven XY sample stage	2 colour pump/probe Balanced photodiode & lock-in amplifier	10 mJ cm^{-2} pump and 2.1 mJ cm^{-2} probe	$MAPbI_3$ perovskite and $MAPbI_3$/ PCBM
Philipp Kukura[39]	Schnedermann, C., *et al.* (2016). *J. Phys. Chem. Lett.*, *7*, 4854–4859.	200 kHz	Focused with a curved silver mirror Collected with a 1.42 NA objective lens	Chopper driven at 50 Hz	Widefield	White light-derived pump and probe pulses fast CMOS camera	16 μJ cm^{-2} pump and and 120 μJ cm^{-2} probe pulse	mixed iodide–chloride methylammonium lead perovskite and TIPS pentacene films
Akshay Rao[13]	Sung, J., *et al.* (2020) *Nature Phys.*, 16, 171–176	200 kHz	Pump focused into sample with an ×100 oil immersion 1.1 NA objective, Counter propagating pump and probe	Chopper driven at 30 Hz	Widefield	White light pump and probe Electron multiplying CCD camera	0.15-1.2 pJ pump fluence. Probe powers not stated	$MAPbI_3$ perovskite thin films
Naomi S. Ginsberg[43]	Wong, C. Y., *et al.* (2013). *J. Phys. Chem. C*, *117*(42), 22111–22122.	5 kHz	Focus: 0.4 NA 10X objective collected using an identical objective	Chopper driven at 500 Hz	Raster scanning a piezo XY sample stage	1 colour pump/probe PMT and two lockins to find ΔT and T	400 μJ cm^{-2} pump 100 μJ cm^{-2} probe	TIPS pentacene films
Giulio Cerullo and Guglielmo Lanzani[17]	Grancini, G., *et al.* (2011). *J. Phys. Chem. Lett.*, *2*(9), 1099–1105.	1 kHz	high NA air objectives (focusing and collection) with an optical fibre, used as a confocal pinhole	Mechanical chopper	Raster scanning a piezo sample stage	WL probe probe is focused into an optical fibre & detected with a photomultiplier tube or spectrometer	300 nJ cm^{-2} pump	P3HT:PCBM Photovoltaic BHJ

In the work by Schnerdermann *et al.* a fast (50Hz) CMOS camera was used to facilitate widefield image acquisition. This is unusual within TAM literature, as most reported set-ups use point scanning microscopy techniques to build up an image. Due to the length of time required to scan the sample stage or scanning mirrors to acquire a full image, when it comes to data collection most research groups take full images at a few key time delays and only collect full kinetic data (with many time delays) for specific points of interest on the sample by probing at a fixed position and varying the delay between the pulses. Practically this is far easier than collecting entire images at every time delay because it is considerably faster and therefore minimises the possibility of drift in the sample. As mentioned in section 4.1, although data can be collected using a spatially overlapped pump and probe (SOPP imaging), as is usually the case with bulk TA measurements, independent motion of the pump and probe beams can provide alternative insights into the response of the sample. Scanning mirrors facilitate this type of data collection as the pump can be left in a fixed position on the sample while the probe is scanned over it to form an image.

Returning to the comparison of MHz and kHz laser repetition rates, common sources of noise in laser systems tend to have frequencies <1MHz. Therefore it is beneficial to detect the signal at a reference frequency greater than this *i.e.* modulate the pump at a frequency >1 MHz.[21] Assuming equivalent power densities and pixel dwell time Fischer *et al.* calculate that use of an 80 MHz laser compared to a 1 kHz laser improves the signal to noise ratio (SNR) by a factor of ~280. [21] However, it is worthy of note that in this calculation it appears Fischer *et al.* do not take the effects of peak power into consideration. Since kHz lasers tend to have higher peak power than MHz ones (a similar amount of power can be delivered in fewer pulses) the drop in SNR of a kHz system compared to a MHz one may be compensated for somewhat by an increase in signal strength. This issue of laser repetition rate and peak power is also an important consideration in terms of photodamage to the sample. Although the peak power of a MHz laser is lower, the time between adjacent pulses is far less than for kHz, therefore, there heat dissipation becomes an important concern. Since sample photodamage depends on the heat dissipation properties of the sample and substrate (and any nanostructures therein [44]), the sample damage threshold, the peak power of the laser, and the laser repetition rate, it is difficult to predict the optimum conditions to maximise signal without causing sample damage. [45-47]

The variety of samples that can be studied by a MHz system is also limited by the population lifetime of the systems. For example, samples with excited state lifetimes that

exceed tens of nanoseconds risk being re-excited by adjacent pulses (for 80 MHz the inter-pulse delay is 12.5 ns) before returning to the ground state in MHz systems, which can lead to misleading kinetics. This issue can be alleviated with the use of pulse picking. Pulse picking selects individual pulses to reduce the repetition-rate of the laser, and as indicated in Table 4.1 is common practice not only due to sample lifetimes but also to aid in lock-in detection since high repetition rate (10s MHz) lock-ins are considerably more expensive than their lower-rate counterparts. It is important to note the distinction between pulse picking, which can select individual pulses and so change the entire repetition rate, and modulation, in which case bunches of pulses may be removed at a time.

Each TAM setup is suited to different kinds of samples, with key factors such as the sample lifetime, microscopic feature dimensions, and damage threshold impacting on the optimum TAM design. Some aspects of TAM set-ups can generally be changed based on the requirements of the sample, such as the power density and choosing pump and probe wavelengths appropriate to the sample. Others are determined by the experimental design and would require rebuilding sections of the experiment to change, such as the repetition rate of the laser, the imaging and detection methods.

The TAM experiment described in this chapter was built with the intention of taking measurements of bulk heterojunction films (see section 4.4). My set-up used an 80 MHz Ti:Sapphire oscillator. The peak powers of the laser pulses were found to be insufficient for super continuum generation in a sapphire plate, limiting the potential of this experiment to narrow-band two-colour pump probe. Early attempts to pulse pick using an AOM (see Section 4.3.1) proved unsuccessful and pump modulation was instead used. Therefore, a population lifetime limit of 12.5 ns was placed on any sample under study to avoid re-excitation. Counter to the typical use of objective lenses to focus and collect light from the sample, to avoid the issues of chromatic aberration and additional chirp, an off-axis parabolic silver mirror was used to focus pump and probe beams into the samples, and an achromatic objective was used for collection, similar to the arrangement used by Schnedermann *et al.*. [39] A piezo-electric stage was used to move the sample for SOPP imaging and an APD and lock-in amplifier were used for detection. This makes my set-up most similar to those reported by the groups of Hartland, [1,8] Huang, [18,48] and Papanikolas, [49] with the key exception of the focal optics and lack of scanning mirrors (see Table 4.1).

4.4. Motivation - Bulk Heterojunction Thin Films

BHJs are a notable example of materials in which micron or nanoscale morphology strongly influences the material properties, and thus TAM studies are essential to provide greater mechanistic insights. BHJs are photovoltaic materials made up of irregular, intercalating, domains of electron acceptor and electron donor materials. Usually the donor molecule is a conjugated polymer and the acceptor is a fullerene, although other small molecules have shown increasing potential as non-fullerene acceptor materials. [50] BHJs are typically synthesised by mixing solutions of the donor and acceptor molecules and spin coating or drop-casting them onto a surface such that they phase separate into acceptor-rich or donor-rich domains. Sometimes additives[51] or annealing steps[52] are also used to affect the size or crystallinity of the resulting domains. I chose to investigate a BHJ blend of PTB7 donor (Poly[[4,8-bis[(2-ethylhexyl)oxy]benzo[1,2-b:4,5-b']dithiophene-2,6-diyl][3-fluoro-2-[(2-ethylhexyl)carbonyl]thieno[3,4-b]thiophenediyl]]) and $PC_{70}BM$ ([6,6]-Phenyl-C71-butyric acid methyl ester) fullerene acceptor. The chemical structures of the donor and acceptor are given in Figure 4.3.

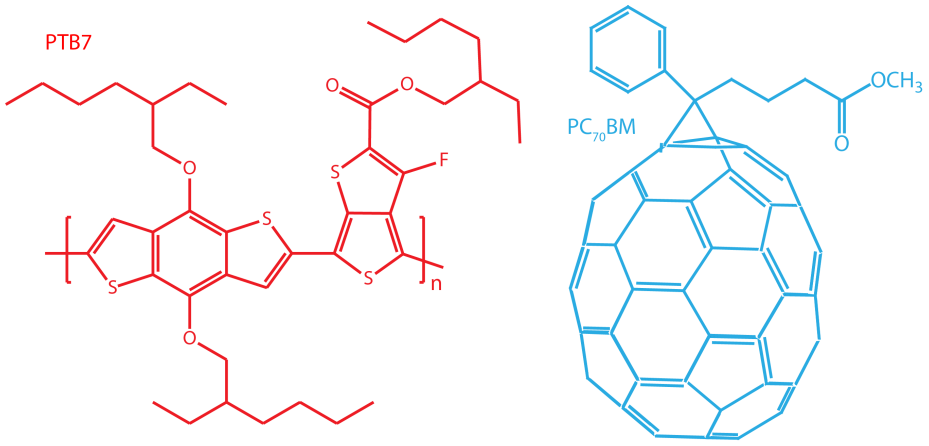

Figure 4.3: Chemical structures of polymer donor PTB7 and electron acceptor $PC_{70}BM$.

The morphology of the domains (including size, purity, and crystallinity) are imperative in determing the properties and power conversion efficiencies of these materials.[53-55] Figure 4.4 is a schematic that illustrates the generally accepted mechanisms involved in PV current generation for BHJs: (1) light is absorbed by the polymer donor domain and forms a Frenkel exciton; (2) the exciton then diffuses to a domain boundary where it comes into contact with acceptor fullerene molecules and dissociates; (3) the electron (or negative charge carrier, widely accepted to be a polaron) diffuses through the acceptor domain to

the anode, the hole (or positive polaron/charge carrier) migrates through the donor domain to the cathode, thereby generating a current. [56] [57]

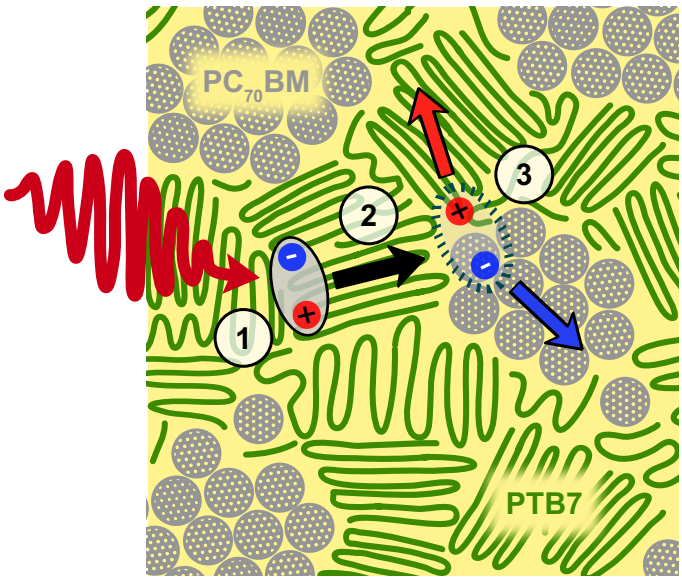

Figure 4.4: Diagram of BHJ charge generation in a polymer blend of PTB7/$PC_{70}BM$: (1) photon absorbed and exciton created (2) Exciton diffuses to domain interface (3) exciton dissociates and charges travel through respective domains.

It is important to note, however, that some studies dispute that this is the primary mechanism for charge extraction. For example findings have indicated that exciton dissociation regularly occurs far (nanometres) from domain interfaces, leaving weakly bound charges that can then easily separate, [58] and recently it has been reported that vibrionic coherence may contribute to exciton dissociation mechanism. [59]

The size, shape, crystallinity and interface properties of the domains all affect the efficiencies of these charge generation and extraction processes. Small domain sizes reduce the distance the excitons have to diffuse in step (2) and therefore, due to the finite lifetime of the polymer excitons, increase the probability of encountering a fullerene domain. [55] Similarly, the size and interconnectivity of the domains is vital in determining how far the free charge carriers have to travel to reach an electrode, and hence the probability of non-geminate recombination occurring in step (3). However, purely crystalline domains are found to have better charge diffusion rates but diminish the probability of generating the carriers in step (2). Therefore, it may seem that an ideal system would minimise domain size while maintaining a discontinuous intercalated network of domains to prevent the formation of isolated islands that would trap the charge carriers. However, the issue is further complicated by many more subtle factors such as the crystallinity of the domains affecting the local transport properties of the materials, [60] or the intermixing of acceptor

and donor molecules at the interface boundary region. [61-63] Due to these dependencies the PCE of BHJs has been improved over the last few decades from a few percent to >10% PCE largely by modifying the domain sizes and composition of these materials. [54]

There are many parameters that determine the morphology of the domains including the choice of acceptor and donor molecules, ratio of donor to acceptor molecules, solvents used, the used of additives, the rate of solvent evaporation, temperature, annealing steps, and concentration of the initial solutions, to name a few. Determining the optimum device morphology for a given blend is extremely complex because of the interplay of the many factors discussed above and because synthesis techniques used to change one of these factors are likely to change others. [61,64] Therefore, huge research effort has gone into understanding the various processes that occur in these materials and how they are affected by the materials' morphology.

TAM studies of BHJ materials could help elucidate the dynamics occurring in these materials and, crucially, how they vary throughout the domains. There have been many bulk transient absorption spectroscopy studies of BHJs, and several have employed TAM techniques[15,17,18,43 25 65] but most of the spectroscopic studies have looked at the archetypal BHJ blend of P3HT donor with $PC_{60}BM$ acceptors, which is by no-means the most efficient donor polymer anymore. The TAM set-up detailed in this chapter was intended to be used to study a BHJ blend of PTB7 donor and $PC_{70}BM$ fullerene acceptor. This blend was chosen as a promising sample on which to perform TAM measurements based on its high performance, novelty, and typical domain size (to ensure they could be resolved by the TAM). PTB7/$PC_{70}BM$ BHJs have been studied with bulk ultrafast transient absorption spectroscopy previously,[66-68] but as far as I am aware, this promising blend has not yet been studied with TAM.

4.5. Experimental Methods and Design

In this section the design and implementation of my TAM set-up are expounded. In addition, preparatory bulk ultrafast TA measurements of the BHJ samples are briefly detailed.

4.5.1. BHJ film samples

Dr Tracey Clarke's group (UCL) synthesised samples of PTB7/$PC_{70}BCM$ BHJ thin films on coverslip slides using spin-coating, as well as control samples of pristine donor or

acceptor films. All samples were vacuum packed for transit and their linear absorption spectra were recorded prior to use.

4.5.2. Bulk kHz TA of BHJ films

Bulk transient absorption measurements were performed to ensure consistency with published literature, to identify spectral features using advantageous broad-band probing, and finally, to monitor the lifetime of the sample and ensure it was less than the 12.5 ns between laser shots to preclude the possibility of re-excitation. The measurements were performed on a separate laser system to that used for TAM. Instead these measurements used the same 1 kHz system as described in chapter 2. Briefly, a 40 μW, 625 nm pump with a ~100 μm focal spot size and ~150 fs pulse duration was used to excite samples. The broadband white light supercontinuum probe was either generated using YAG to create a near-IR continuum, or sapphire for the visible to NIR region of the spectrum and was detected on a CCD detector (Stresing). 300 shots were acquired for each time delay in a cycle and the data was averaged over 10-15 acquisition cycles. All measurements were performed at the magic angle.

4.5.3. TAM Experiment

Figure 4.5 shows a schematic of the TAM experimental apparatus. A 4 W, 80 MHz, oscillator (Coherent Chameleon) tuneable between 680–1080 nm, pumped an optical parametric oscillator (OPO, Coherent Chameleon Vision II). A 80:20 beam splitter within the OPO divides the input beam from the Ti:Sapphire oscillator; 80% pumps the OPO and the 20% beam is bypassed through the OPO and was used as the probe for TAM measurements. The output wavelength of the OPO was tuneable over the range of 1000–1600 nm but dependent on the driving frequency from the oscillator. The OPO generated signal was used to form the pump laser line for TAM experiments.

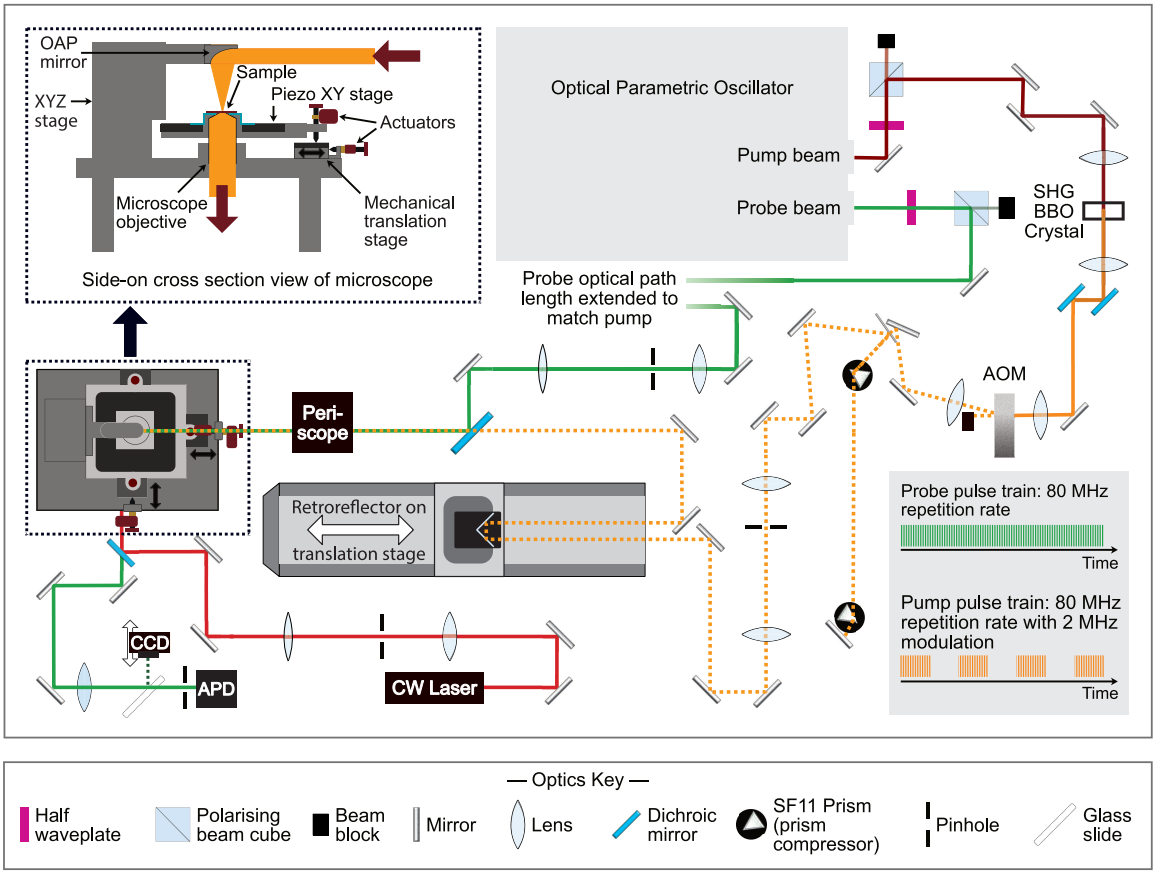

Figure 4.5: (a) Diagram of TAM set-up. Inset, top left shows side-view of microscope body. Inset bottom right compares pump and probe pulse trains

The OPO output (pump beam) was attenuated using a half waveplate and polarising beam cube, before being focused into a SHG BBO crystal (Eksma, θ=23.4°, Φ=90° 2 mm thick) to produce visible (typically 600 nm) light via second harmonic generation, after which two dichroic mirrors were used to remove the fundamental near-IR. The pump beam was modulated by a tellurium dioxide acoustic optical modulator (Isomet, 1250C-848 with a 535C-2 driver, see section 4.2.1 for further details), which typically applied a 2 MHz modulation to the pump pulse train (see inset in Figure 4.5). The TeO_2 AOM crystal added considerable GDD to the ultrafast pulse (at 600 nm the TeO_2 crystal was calculated to apply at total GVD of ~9965 fs^2), so the diffracted beam was collimated and compressed using a folded prism compressor (see section 4.6.1 for more information about pulse characterisation). The laser beam's spatial mode was then improved by focusing through a 25 μm pinhole in a 1:2 telescope to produce a Gaussian beam mode with a larger beam

diameter (for microscopy considerations), before being routed along a retroreflector on a motorised delay stage (Physik Instrumente, M-521.DD1).*

The probe beam (the aforementioned, unused portion of the Ti:Saph output) had a comparatively simple beam line. The beam was also attenuated using a half waveplate and polarising beam-cube and then followed a long path such that it matches the distance traversed by the pump beam both inside the OPO (1.66 m) and thereafter, before being focused through a 25 μm pinhole in a 3:8 telescope. The collimating lenses following the pinholes for both pump and probe beams where chosen with consideration of the spot sizes at the sample. The beams were combined and overlapped on a dichroic mirror (Thorlabs, DMSP750B) and made collinear (by checking alignment in the far field) before entering a periscope into the microscope.

The microscope (see inset of Figure 4.5) consisted of a raised baseplate into which the collection microscope objective lens was mounted. The sample (a coated coverslip) was positioned above the objective on a piezo *x*-*y* stage (Physik Instrumente, P-541.2DD XY translation stage and an E-727.3CD controller) which was mounted on a coarse three point scanning stage to facilitate a larger range of motion than the piezo stage can achieve (see section 4.5.3.5 for further details). An off axis parabolic (OAP) mirror (Edmund Optics 87407, 25.4mm diameter and 50.8 mm effective focal length) was positioned over the collection objective on a XYZ translation stage (Newport M-562-XYZ), such that the incoming beams were focused by the OAP into the sample and collected and collimated by the objective (Niko Apo LWD 40×, water immersion, 1.15 NA objective). After the microscope the residual pump is removed using a long pass dichroic (Thorlabs, DMLP650) and a long pass filter (Thorlabs, FELH0650). The probe and modulated heterodyne signal were focused (f = 200 mm) through a removable 25 μm pinhole and onto the avalanche photodiode detector (Menlo systems APD210).

The signal from the APD was fed into a lock-in amplifier (4 MHz Stanford Research Systems SRS865) and the lock-in was referenced at the rate of the modulation applied to the AOM/pump pulse (typically, 2 MHz). This reference signal was triggered directly from the output of a photodiode in the Chameleon laser. The photodiode output was used to trigger a picosecond delayer (PSD, MicroPhoton devices) to generate a TTL-

*Note, although it may seem more intuitive to improve the pump beam mode as the final step before the sample (*i.e* after the delay stage), the beam was unavoidably poorly collimated after being generated in a thick BBO crystal and then being diffracted from within a thick AOM. So, changing the optical path length of the beam (on the delay stage) prior to the pinhole changed the focusing conditions into the pinhole and therefore altered the pump power at the sample.

like pulse, which was used as a reference frequency for the AOM Radio Frequency driver and the lock-in. The set-up was coordinated and controlled by LabView software, using a combination of plug-ins provided by equipment manufacturers and custom ones I wrote.

4.5.3.1. Acoustic Optical Modulator

AOMs use acoustic waves travelling through a crystal to diffract incident light (Figure 4.6). The diffraction occurs because the acoustic waves in the crystal travelling perpendicular to the light periodically displace the crystal lattice causing it to display periodic regions of higher and lower density, which act as a transient diffraction grating. Since diffraction only occurs while the acoustic wave is coincident with the laser in the crystal, the speed at which the diffraction can be switched on or off is primarily determined by the speed of the acoustic wave. Therefore, the diffraction, and hence modulation, can be controlled at MHz rates, making AOMs ideally suited for high repetition rate (>100s kHz) modulation of optical pulse trains.

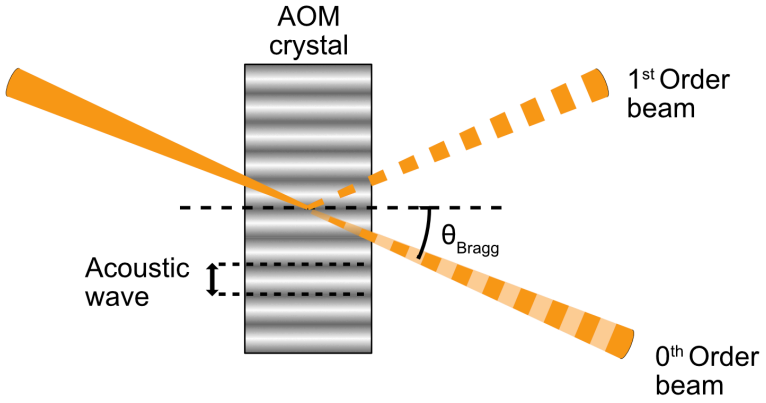

Figure 4.6: Schematic illustration of AOM operation.

In this experiment the AOM is used to apply a modulation to the probe beam such that bunches of pulses (with an 80 MHz repetition rate) are diffracted at a frequency less than 4 MHz (typically 2 MHz, since 4MHz is the maximum reference rate the lock-in can operate at). The first order diffracted beam is used as the probe in the experiment and the 0^{th} order diffracted beam is dumped. This is because the diffraction process is never 100% efficient, and so the 0^{th} order beam can never truly be 'turned off', low power pulses would remain in the pulse train and may also excite the sample.

The AOM in the apparatus used 200 MHz acoustic waves (driven by a radio-frequency generator) travelling through a TeO_2 crystal. Initially the AOM was tested to see if it could effectively pulse pick single laser pulses so that samples with an excited state

lifetime of greater than 12.5 ns (the time between laser pulses at 80 MHz) could be measured without re-exciting the sample. However, the rate at which the AOM can operate is limited by the acoustic speed within the crystal, the acoustic wave pulse duration, and the volume of the crystal illuminated by an incident laser pulse. Even using the shortest pulse of 200 MHz acoustic waves the AOM can produce (about 1 ns), at an 80 MHz laser repetition rate the AOM diffracted multiple pulses of light. Focusing the laser into the AOM reduces the spatial region over which the acoustic wave is coincident with the light pulse train, resulting in fewer laser pulses being diffracted. Therefore, a variety of focal conditions were tested, including expanding the beam before focusing it to reduce the focal spot size. However, short acoustic pulses and tight focusing conditions both decrease the diffraction efficiency, and a minimum of three laser pulses were still diffracted, one with a relatively high efficiently and two temporally adjacent pulses with a lower efficiency. Despite the low power of the unwanted pulses they could lead to unreliable measurements as the lock-in may still pick up signal from these pulses. Therefore, without purchasing a different AOM with a thinner crystal (to reduce the interaction volume) and a higher RF frequency driver (to facilitate shorter duration acoustic waves), diffraction of individual pulses of light was not possible. Hence the AOM was optimised to diffract bunches of pulses (as indicated in Figure 4.5 inset) with high throughput efficiency, thereby limiting this experiment to samples that have lifetimes less than 12.5 ns.

4.5.3.2. Electrical Signalling and Triggering

All of the electrical MHz signals were triggered from the output of a photodiode built into the laser oscillator laser, to ensure all components of the experiment remained synchronised despite any variation in the cavity rep rate (variation is typically >1%). However, depending on the laser output wavelength and the length of time the laser had been operating for, this signal could be fairly noisy, and was far from the clean TTL-like pulse that was needed to trigger the AOM and provide a reference frequency for the lock-in amplifier. It was found that a commercial picosecond delayer (PSD manufactured by MPD) could reliably detect the laser repetition rate directly from the photodiode output and could produce a clean TTL-like pulse train with frequencies at factors of the 80 MHz rate.

As standard, the PSD threshold trigger level was set to 100 mV and a factor of 40 was used to divide the pulse train to generate a 2 MHz rep rate. The output pulse duration had to be set to pre-designated discreet values, typically 241 ns was used as this was the

closest option that provided a 50% duty cycle (2 MHz corresponds to a 500 ns period) which the lock-in reliably detected as being a 2 MHz reference signal. Note that this means the output is not a 'true' TTL pulse since in electronic engineering a TTL pulse has a 50 % duty cycle and a maximal 'on' voltage of 3.3V. The output of the PSD was split between triggering the AOM radio frequency driver and providing a reference frequency for the lock-in amplifier.

4.5.3.3. Lock-in Detection

Lock-in amplifiers enable detection of periodic signals with very high sensitivity, even in the presence of predominant noise or undesired background. This is achieved by comparing a reference frequency with the input in a method called phase sensitive detection. Signals that are at the same frequency as the reference and that maintain a constant phase are selected, and the signal output is given by:

$$V_{signal} \cos\theta \tag{4.4}$$

Where θ is the phase difference between the signal and reference. All signals that occur with a different phase or frequency are rejected as noise. The lock-in amplifier used in this work is a dual-phase lock in, meaning the two outputs, X and Y are recorded with a 90° phase difference between them. Therefore, the phase dependency of the signal can be removed and the signal magnitude is given by:

$$R = \sqrt[2]{X^2 + Y^2} = V_{signal} \tag{4.5}$$

The lock-in settings (most notably integration time and noise filter) were set manually on the device. Typically, a 300 ms integration time and 6 dB noise filter were used for non-linear signal detection. The lock-in streamed the data to the computer via an ethernet connection. The device did this in UDP packets (User datagram protocol packets- a method of encoding packets of data for transfer), made up of 32-bit floats of R data. UDP packets have the advantage of including headers in the packets with integrity checking so that if an error occur, (for example part of a packet is lost because the computer cannot process the incoming data fast enough) the whole packet is discarded. The time required to acquire a packet's worth of data depends on the integration time (manually set on the instrument), as the averaging over this time is done internally within the lock-in. Initially

the packet size was set to be as large as possible (1024 bytes) to maximise the data content of each packet and therefore minimise the processing time per unit of data. However, following the discovery of latency issues as discussed in section 4.6.5 the packet size was set to be as small as possible (128 bytes) to minimise this problem.

4.5.3.4. Software

The control software for automated data acquisition was written in LabVIEW and used some virtual instrument files (VIs) provided by manufacturers, including ones for control of the Stanford instruments lock-in and for the Physik Instumente delay stage and microscope stage. The programme starts by initialising the delay stages and the lock-in amplifier streaming connection. Once initialised the delay stage was moved independently to allow the user to find the position of the delay stage corresponding to time zero. For data acquisition the programme has two operating modes; image or kinetic acquisition. The imaging mode leaves the delay-stage in its initial position and only moves the microscope piezoelectric *x*-*y* stage. The piezo stage scans the sample in a raster pattern determined by the input settings for image dimension and pixel size. In the kinetic acquisition mode, the *x*-*y* microscope stage remains fixed and the motorised delay stage (controlling the pump-probe time delay) is translated to acquire the time-dependent response from a single point (or pixel) of the sample.

The total acquisition time for a single pixel depends on both the integration time set on the lock-in and the number of averages of the resulting data the computer makes. This design was used so the standard deviation could be calculated for each pixel/datapoint in case noise filters were desired in future experiments to monitor effects that would result in large deviations from the mean, such as burning during acquisition.

4.5.3.5. Microscope Design

As mentioned previously, the microscope used an OAP mirror to focus the pump and probe beams and a high NA objective lens to collect light from a small spot within the illuminated area. All fine motion and scanning of the sample for imaging purposes was achieved using the piezoelectric *x*-*y* stage. The *z*-positioning of the sample in the focus was achieved by suspending the piezo stage in a custom-made tray supported by three screws, henceforth referred to as spindles, in a tripod-style arrangement. The spindles were positioned on three sides of the rectangular tray excluding the side adjacent to the *x*-*y* translation stage

supporting the OAP. The tray was designed such that the spindle opposite the OAP mount was furthest from the focal position of the microscope so that incrementing the height of this spindle made the smallest change in the height of the sample above the focus compared to the other two spindles. This spindle was fitted with an actuator (Newport, 8301NF: Picomotor Actuator and 8742 Picomotor Controller) such that the height of the sample could be remotely adjusted with the control computer during microscope operation.

In addition to the *z*-positioning, motion of the stage tray also facilitated coarse *x*-*y* motion beyond the range achievable with the piezo stage alone (the *x*-*z* piezoelectric stage was motion limited to 45 x 45 μm). This was achieved by positioning the ends of two of the spindles in a V-grove and a cone/divot carbide pads on translation stages (Newport 9065M-X) fitted with two more actuators, the third spindle rested on a flat carbide pad (Newport CPP-V, CPP-C, CPP-F). This arrangement allowed the coarse and *z*-position of the sample to be controlled through computer software (provided by Newport) moving the three actuators.

4.5.3.6. Microscope Alignment

For the microscope section of the experiment to be correctly aligned several criteria must be fulfilled (1) the incoming colinear pump and probe beams need to be horizontal, and (2) reflected by the OAP so they focus directly below it at the sample; (3) the microscope objective needs to be 0.19 mm (the working distance) from the OAP focal position, to maximise the amount of light it collects and so the outgoing beam is collimated; (4) finally, the sample needed to be positioned in the focal plane of the beams.

In order to achieve this arrangement a diode laser (Odic Force Lasers, OFL434 continuous wave 650 nm, 50 mW) was used back align the optics. Since the collimation and mode of the alignment laser was poor, first it was focused through a pinhole and collimated to give a beam with >7 mm diameter so that it would overfill the back of the microscope objective. It was then directed into the microscope using the dichroic that removes the residual pump after the sample in normal measurement operation. Note, the cut-off wavelength of the dichroic is 650 nm, meaning approximately 50% of the beam was reflected off this dichroic and the remainder was transmitted. The procedure developed for aligning the microscope is outlined in the following steps:

1. The microscope was dismantled (the OAP, *xyz* stage, the piezoelectric *x*-*y* stage and the objective were all removed) and the alignment laser was made to pass vertically

through the baseplate using a lens tube (and approx. 0.3 m), and a frosted pin hole as a target. Note that because some of the alignment laser was transmitted through the 650 nm dichroic, there were unavoidably two spots at this point, displaced by a distance related to the thickness of the dichroic, therefore it was important to note which beam arises from reflection off the front face of the dichroic and to use it for alignment.

2. Once the beam passed through the frosted pinholes at one and two lengths of tubing from the baseplate, the lens tubing was removed, and replaced with a short piece of lens tube containing a mirror to reflect the alignment beam back on itself. At the dichroic a portion of the reflected beam was transmitted and followed the path the probe beam took in normal operation. This beam was then used to align the optics associated with detection; an achromatic lens focused the beam into a pinhole directly before the APD detector and a portion of the beam was deflected using a removable glass slide onto a CCD. The CCD was translated until it is at the focal position, which was found by minimising the size of the imaged spot.
3. Once the optics for detection were aligned, the microscope was reassembled by replacing the objective (screwed into the baseplate), the *x*-*y* stage (both the coarse positioning tray and piezo stage), and the OAP on a three-dimensional translation stage. The alignment laser then focussed after passing through the objective; the OAP had to be positioned above the objective using the 3D stage it was mounted on, such that the outgoing alignment laser beam was collimated. This was checked by adding a mirror after the OAP so the alignment beam was deflected before the periscope leading to the rest of the set-up, such that the collimation could be checked several meters in the far-field.
4. Next, the sample stage was replaced. To ensure the sample was at the correct height, in place of a sample a mirror was positioned over the microscope objective (with immersion oil) and the height of the entire coarse stage was altered (by moving the three spindles) until the size of the spot imaged on the CCD was minimised and the stage was level, indicating the mirror was at the focus of the objective.
5. Finally, the pump and probe beams were made collinear to the counter propagating alignment laser beam using the mirrors on the periscope leading to the microscope. This alignment was assumed to be sufficient when the alignment laser beam passed through the pinhole used to spatially filter the pump beam and *vice versa*.

4.5.3.7. Operating Procedure

Typically, the microscope would have to be realigned every fortnight to correct for minor drift in the optics. In daily operation, the laser would be left on for at least an hour to equilibrate before operation of the set-up. To take a measurement of a sample deposited on a coverslip, immersion fluid was applied to the back face of the sample and it was placed on the sample holder such that the immersion fluid was between the sample and objective, before the sample was secured using clips. Then the alignment laser was used to check the sample was at the microscope focus: the back reflection of the alignment laser from the front face of the coverslip was imaged onto the CCD and the spot size was minimised by adjusting the height of the sample with the actuator spindle. The alignment laser was then blocked, and pump and probe beams were unblocked before measurements could commence.

4.5.3.8. Functionality Tests

In order to ensure the TAM set-up was functional, the ultrafast spectroscopy and microscopy components were tested separately by performing bulk pump-probe measurements and linear microscopy measurements.

To facilitate bulk pump-probe measurements the TAM set-up was altered by removing the periscope that normally leads to the microscope and replacing it with a focusing mirror (f = 25cm) in a 'V' configuration with a flat pick-off mirror that directed the focusing beams into the sample. After the sample the signal and probe were separated from the residual pump light using a dichroic filter (Thorlabs, DMSP750B), before being focused into a photodiode connected to the lock-in amplifier. The samples were positioned in the focus by manually moving a small translation stage into which a lens mount containing the sample was secured.

To test the functionality of the microscopy components of the set-up, test images were taken with the pump beam blocked and using a mechanical chopper wheel (operating at 3 kHz) to modulate the probe beam directly with the chopper output frequency used as the reference for the lock-in. In this configuration the measurement is purely of transmission of the probe through the sample and therefore is a linear optical microscopy image; *i.e.* the only cause of a decrease in transmission was due to linear effects such as absorption or scatter.

4.6. Results and Discussion

4.6.1. Sample Characterisation

The linear absorption spectra of the BHJ film samples were acquired as displayed in Figure 4.7(a). Figure 4.7(b) also displays the linear absorption spectra of cadmium telluride (CdTe) quantum dots (PlasmaChem, PL-QDN-750) dispersed in water and panel (c) shows the absorption of LDS 798 dye in methanol at various concentrations, both of which were used to test the functionality of the TAM apparatus.

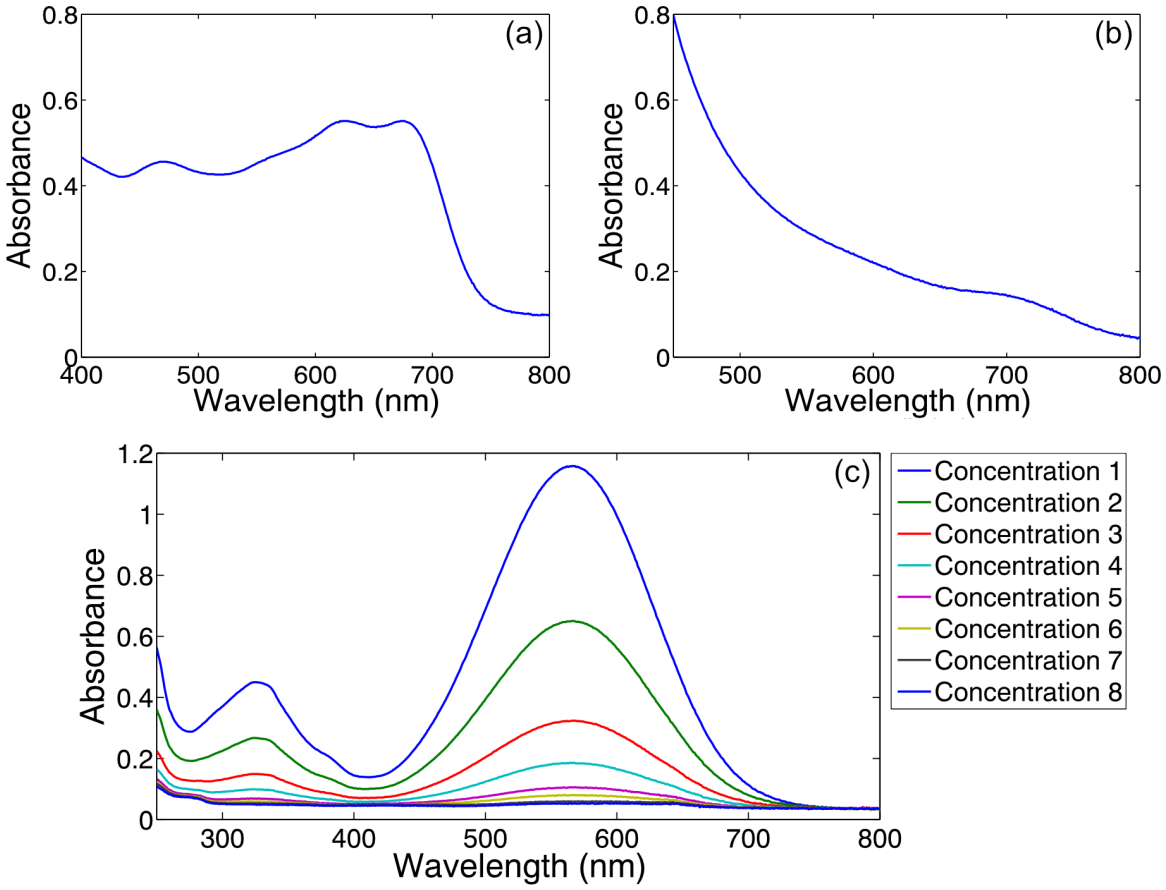

Figure 4.7: Linear absorption spectra of (a) PTB7/$PC_{70}BM$ bulk heterojunction thin film, (b) CdTe quantum dots dispersed in water, (c) solutions of LDS798 dye in methanol at various concentrations which decrease through numbers 1-8.

4.6.2. kHz Bulk Measurements

TA data of a pristine PTB7/$PC_{70}BM$ BHJ and pristine PTB7 films are shown in Figures 4.8 and 4.9, respectively. The TA data are consistent with previous studies[66,69] and clearly demonstrate that the vast majority of molecules have returned back to their original state within 1 ns, and therefore will not persist up to the 12.5 ns limit between laser pulses in the 80 MHz experiments.

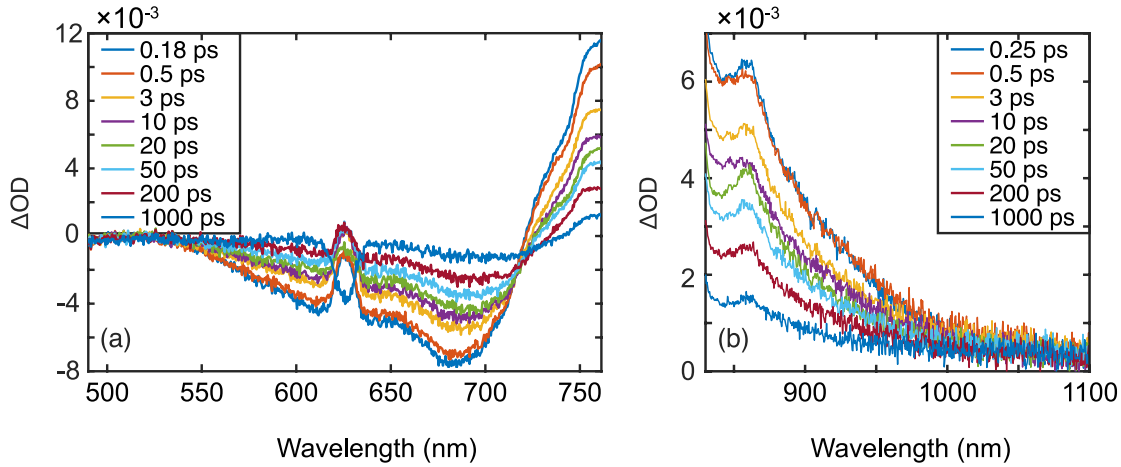

Figure 4.8: Bulk kHz TA data of a PTB7/$PC_{70}BM$ BHJ film, using (a) sapphire and (b) YAG generated broadband continuum probes.

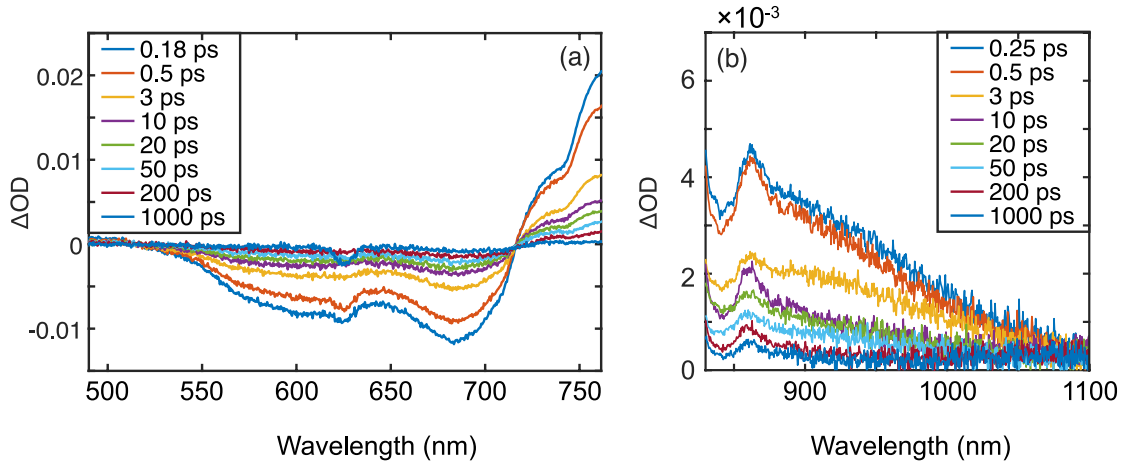

Figure 4.9: Bulk kHz TA data of a pristine PTB7 film, using (a) sapphire and (b) YAG generated broadband continuum probes.

4.6.3. MHz Pulse Characterisation and Compression

The 800 nm probe pulse was characterised using a commercial SHG-frequency resolved optical grating spectrometer (Swamp Optics GRENOULLIE) and was found to have a pulse duration of 125 ± 10 fs, which is better than a transform limited Gaussian pulse (158 fs, calculated using parameters: 6.0 ± 0.3 nm bandwidth and a central wavelength of 801.7 ± 0.3 nm), but worse than the transform limit of a $sech^2$ pulse (113 fs). Hence no pulse compression was required in the probe line.

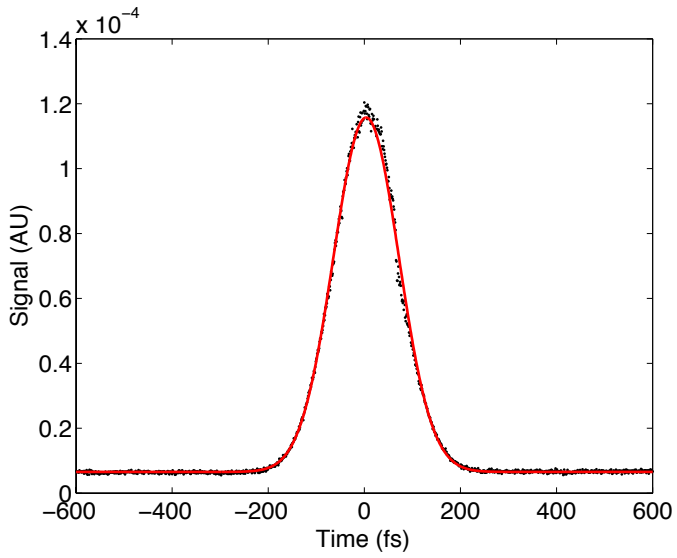

Figure 4.10: SHG autocorrelation trace of pump pulses (black circles), with overlaid fit to Gaussian response function (red line).

In contrast, the near-IR output of the OPO which was used to generate the TAM pump, was significantly chirped. Further, after the OPO these pulses passed through several transmissive optics in the TAM set up, including the SHG BBO crystal and most notably the TeO_2 AOM crystal. The pulse duration before compression could not be measured because the peak power of the chirped pulses was insufficient to generate a measurable amount of SHG light in a homebuilt SHG autocorrelator. The pump was compressed using a folded prism compressor, with two SF11 equilateral prisms approximately 35 cm apart. The pulse compression was iteratively optimised using the autocorrelator and led to the generation of ~111 ± 4 fs pulses (Calculated from fitting to a Gaussian function as shown in Figure 4.10). This demonstrates the pulse was well compressed given transform limited pulse durations of 124.4 fs and 88.9 fs for Gaussian and $sech^2$ pulses respectively, based on a spectral bandwidth of 4.3 ± 0.3 nm at the central wavelength of 603.3 ± 0.3 nm, as shown in Figure 4.11.

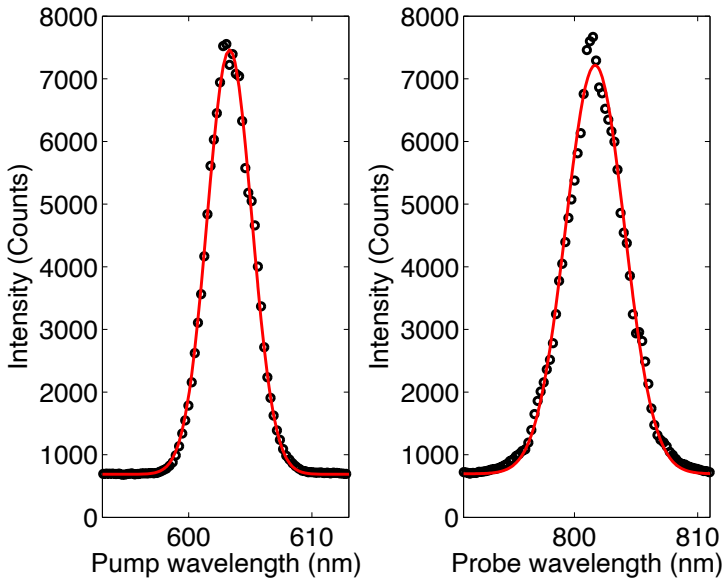

Figure 4.11: Laser spectra of pump and probe pulses as measured with an Ocean Optics spectrometer. Red line overlays are fits to Gaussian functions.

4.6.4. MHz Bulk Measurements

Bulk pump-probe measurements were performed on LDS 798 (Styrl-11) dye in methanol solution in a 1 mm path length static cuvette, for a number of different dye concentrations (Figure 4.12(a)) and at different laser powers (Figure 4.12(b)). The lowest concentration dye solution studied had a maximum absorbance of ~0.02 illustrating the high sensitivity of the detection system. Measurements taken at a variety of pump-probe powers (maintaining a pump-probe power ratio of 2:1) revealed that the non-linear response could be clearly detected with powers as low as 125 μW pump and a 63 μW probe, which gave signal on the order of 10^{-7}, which is consistent with the sensitivity of MHz TAM experiments reported in literature.[11,18]

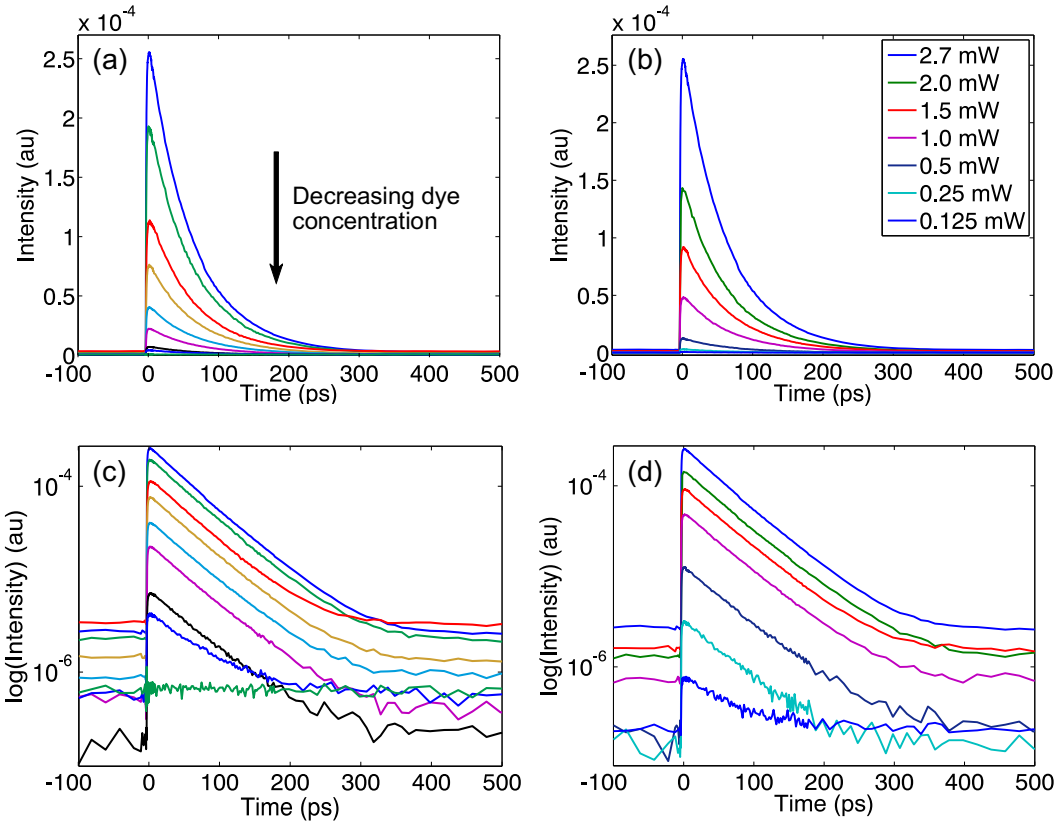

Figure 4.12: Bulk MHz measurements of LDS 798 solutions (a) for various (a) concentrations (plot line colours correspond to concentrations shown in figure 4.7(c)) (b) laser powers. (c) and (d) display the same data as (a) and (b) respectively but on a log scale to reveal the lowest intensity signals

Measurements of the solid samples deposited on coverslips (CdTe quantum dots and a PTB7 polymer film) revealed that at high powers the signal intensity dropped with time, which can be attributed to thermal damage to the sample. Therefore, a series of measurements at different powers were made on the quantum dot sample to find the highest pump power that could be used without causing this effect (again keeping the pump and probe powers in a 2:1 ratio). This limited the maximum powers to 0.6 mW pump and 0.3 mW probe to prevent sample damage. From this it was estimated that the equivalent maximal power that could be used for this sample in the microscope without increasing the peak power density (due to tighter focus) was 25 µW pump and 12 µW probe. This was calculated by assuming an inverse square relation between power density and focal length. Note, this assumes that in both configurations the beams are focused perfectly, the sample is positioned perfectly in the focus, and the spot size is greater than the diffraction-limited spot size and so not limited by it.

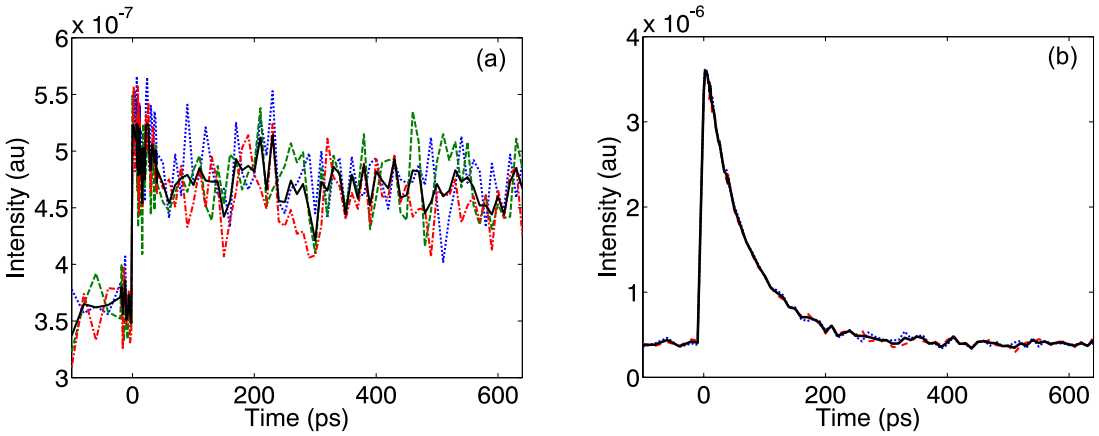

Figure 4.13: Bulk MHz measurements of (a) drop cast CdTe quantum dots acquired with 0.6 mW pump and 0.3 mW probe powers and (b) PTB7 polymer film, acquired with 0.5 mW pump and 0.25 mW probe. Dotted colour lines show repeat acquisitions, black solid line indicates average.

A similar laser damage threshold was observed for measurements of a thin film of PTB7 polymer (fig 4.13(b)). The apparent lower levels of noise in the PTB7 data compared to the quantum dots can be explained by better positioning of the sample at the focus of the laser beams and potentially less scatter from the sample.

4.6.5. Linear Microscopy

Figure 4.14 shows several linear microscopy images of a coverslip patterned with gold which was used as a test sample. Figure 4.14(a) was acquired with a 25 µm pinhole positioned before the detector. As expected, and as for conventional confocal microscopy, this dramatically improved the spatial resolution of the images compared to when it was removed (see Figure 4.14(b)). This is because the pin hole removes light that was scattered out of the focal plane of the microscope. However, due to issues finding a stable non-linear signal in samples, for all of the measurements discussed in the following sections the pinhole was removed to maximise the amount of probe and signal reaching the detector.

In early test images issues with a latency between data collection and processing were observed. This led to streaks in the images, which were noticeable in areas of high contrast (*e.g* the edge of a gold patterned structure) and depended on the travel direction of the stage, as shown in the bottom half of Figure 4.14(c). To reduce this effect the packet size of data streamed from the lock-in was minimised and the image collection parameters (pixel averaging, lock-in time constant, and pixel size) were also varied. As shown the effect was removed when the integration time on the lock-in amplifier was sufficiently short (so the lock-in was more responsive to changes in the signal) or the number of

averages the computer made at a pixel was sufficiently high (so the pixel dwell time was longer which gave the lock-in time to respond and the latency effects were averaged out).

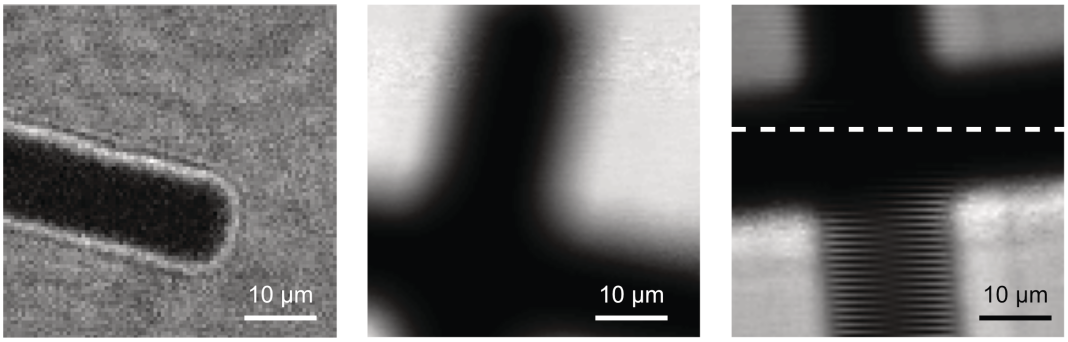

Figure 4.14: Linear microscopy images of gold patterned coverslip with (a) pinhole in place before detector, (b) image taken without pinhole, (c) Image demonstrating streaking caused by latency issues. In the bottom of this image streaks are apparent because the lock-in integration time is too long relative to the speed at which the stage moved between pixels. In the top section of the image (indicated by the dashed line) the effect is reduced by decreasing the lock-in integration time.

4.6.6. TAM Measurements

Using the aforementioned sample of CdTe quantum dots deposited on a coverslip, a non-linear signal was detected (Figure 4.15) inside the microscope, however the sample was clearly significantly damaged in the measurement process as is apparent from the drop in signal intensity between repeat measurements. These data were acquired using pump and probe powers of 15 µW and 7 µW respectively, considerably less than the 25 µW and 12 µW limits estimated from bulk measurements. This discrepancy could be due to an overestimation of the focal spot size or, more likely, it may be due to better positioning of the sample in the focal plane of the microscope than was achieved for the bulk measurements and hence a higher energy density in the sample. Unfortunately, on repeated occasions when the laser powers were reduced this signal was lost. No stable signal was found for the PTB7 polymer film sample despite numerous attempts. Given the success of other similar TAM experiments the reasons for this are currently unclear.

These non-linear signal issues precluded the possibility of acquiring a non-linear microscope image. The effect of thermal damage was far too rapid to acquire such an image, as the sample bleached before sufficient dwell time could be completed. The resulting images were dominated by a gradient of light to dark (high signal to low signal) from top to bottom, following the scan direction.

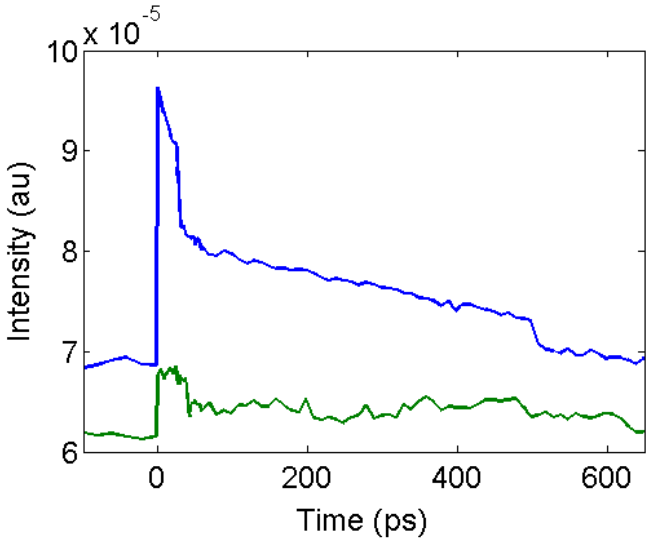

Figure 4.15: Non-linear signal from CdTe quantum dots from two successive measurements. Blue line – first measurement, green line – second measurement.

To ensure the poor signal strength was not due to improper alignment of the microscope, the alignment was repeatedly checked. I ensured that the pump and probe beams focused to the same spot in the sample *x*-*y* plane. This process was performed using the gold patterned coverslip sample, the position of the pump and probe beams in the sample were compared by imaging the probe beam on the CCD (usually used to monitor the sample height), and inspecting the residual pump beam after the microscope on a piece of card at high powers. Since the gold coated areas of the sample are opaque to the pump and probe wavelengths, these regions were visible in both the beams and so the position of the beams in the samples could be compared. This test repeatedly indicated that the focal spots were overlapped, however it is possible that the process of changing the powers of the beams (by rotating the half-waveplates at the start of beam lines) altered the beam pointing. Therefore, to further test this in future work a beam profiling camera could be positioned in the microscope focal plane to image the focal spots. This would also provide a precise measure of the focal spot sizes.

Alternatively, given the success of many similar MHz TAM experimental set-ups, it seems probable that the discrepancies between the experiment constructed and detailed in this chapter and those in literature could be the cause of these issues. Two key differences are the use of an OAP mirror to focus light into the sample and potentially the lack of pulse picking commonly used to reduce repetition rate of the laser, although some experiments do not specify this. The use of the OAP mirror results in a significantly larger area of the sample being excited than the collection objective can collect from. This may increase the level of noise in the data due to scattered light from the peripheral regions. In addition,

because a larger area is illuminated, higher average powers are needed to achieve consistent peak energy densities per pulse in the sample. Although the energy density per pulse used in these experiments is comparable with literature (see Table 4.1) values, the (average) power density may be greater. This issue could be compounded by the lack of pulse picking leading to less time between pulses for heat to dissipate. It is still somewhat surprising that the power could not simply be reduced to alleviate this problem. However, it is possible that at lower powers the peak power in the sample was insufficient to generate a non-linear signal or the reduced signal intensity was obscured by significant scatter/noise. The effect of the OAP could be tested relatively simply by replacing the OAP with an objective lens, although the compression of the pulses would likely need to be adjusted to account for the significant amount of additional GVD. The effect of the repetition rate would be considerably more difficult to test as a pulse picker would need to be added between the laser oscillator and the OPO, or two pulse pickers would be needed after the OPO.

4.7. Conclusions and Future Work

Attempts to build a transient absorption microscope have been, thus far, largely unsuccessful. As expected, the use of a secondary (confocal) pinhole in linear microscopy was shown to improve resolution. However, samples burned during non-linear microscopy measurements even at low pump fluences, and this precluded the acquisition of non-linear microscopy images and time-resolved data. The reasons for such poor signal to noise is currently unclear. However, bulk MHz measurements showed high sensitivity and low noise levels and linear microscopy images indicate that the microscope was well aligned and operational. Bulk measurements with the same apparatus also demonstrated the acquisition software and integration of multiple electronic devices, including the lock-in amplifier, were operational. Therefore, based on the success of similar experiments in literature and successful acquisition of data in bulk measurements, the issues are most probably due to an insufficiently tight focus into the sample because an OAP mirror was used rather than an objective lens.

If the current issues with this experiment were resolved a further improvement worthy of consideration is the use of a secondary AOM in the probe line to allow dual modulation at MHz frequencies. Alternatively, use of a pulse picker immediately after the commercial oscillator to down-grade the repetition rate of both the pump and probe lines would be advantageous as it would allow measurement of longer-lived species, albeit with

longer acquisition times. In conjunction with this, use of a lock-in amplifier which can lock-in to reference frequencies at 10s of MHz would likely see a reduction in noise.

Despite the shortcomings of this experiment the potential of TAM is clear. Recent publications detailing combinations of advance spectroscopic and microscopic techniques, such as 2DIR[31] or 2DES[32,33] confocal microscopy and transient absorption NSOM[36,37] or STED, [34,35,70] demonstrate exciting developments in this field and the rich variety of potential samples hold the promise of interesting discoveries.

References

(1) Hartland, G. V. Ultrafast Studies of Single Semiconductor and Metal Nanostructures Through Transient Absorption Microscopy. *Chem. Sci.* **2010**, *1* (3), 303–307.

(2) Crut, A.; Maioli, P.; Vallée, F.; Del Fatti, N. Linear and Ultrafast Nonlinear Plasmonics of Single Nano-Objects. *J. Phys.: Condens. Matter* **2017**, *29* (12), 123002–123023.

(3) Huang, L.; Cheng, J.-X. Nonlinear Optical Microscopy of Single Nanostructures. *Annu. Rev. Mater. Res.* **2013**, *43* (1), 213–236.

(4) van Dijk, M. A.; Lippitz, M.; Orrit, M. Detection of Acoustic Oscillations of Single Gold Nanospheres by Time-Resolved Interferometry. *Phys. Rev. Lett.* **2005**, *95* (26), 267406–4.

(5) Staleva, H.; Skrabalak, S. E.; Carey, C. R.; Kosel, T.; Xia, Y.; Hartland, G. V. Coupling to Light, and Transport and Dissipation of Energy in Silver Nanowires. *Phys. Chem. Chem. Phys.* **2009**, *11* (28), 5889–5889.

(6) Yabuta, M.; Takeda, A.; Sugimoto, T.; Watanabe, K.; Kudo, A.; Matsumoto, Y. Particle Size Dependence of Carrier Dynamics and Reactivity of Photocatalyst BiVO4 Probed with Single-Particle Transient Absorption Microscopy. *J. Phys. Chem. C* **2017**, *121* (40), 22060–22066.

(7) Lo, S. S.; Major, T. A.; Petchsang, N.; Huang, L.; Kuno, M. K.; Hartland, G. V. Charge Carrier Trapping and Acoustic Phonon Modes in Single CdTe Nanowires. *ACS Nano* **2012**, *6* (6), 5274–5282.

(8) Gao, B.; Hartland, G. V.; Huang, L. Transient Absorption Spectroscopy of Excitons in an Individual Suspended Metallic Carbon Nanotube. *J. Phys. Chem. Lett.* **2013**, *4* (18), 3050–3055.

(9) Mehl, B. P.; Kirschbrown, J. R.; Gabriel, M. M.; House, R. L.; Papanikolas, J. M. Pump–Probe Microscopy: Spatially Resolved Carrier Dynamics in ZnO Rods and the Influence of Optical Cavity Resonator Modes. *J. Phys. Chem. B* **2013**, *117* (16), 4390–4398.

(10) Schnedermann, C.; Sung, J.; Pandya, R.; Verma, S. D.; Chen, R. Y. S.; Gauriot, N.; Bretscher, H. M.; Kukura, P.; Rao, A. Ultrafast Tracking of Exciton and Charge Carrier Transport in Optoelectronic Materials on the Nanometer Scale. *J. Phys. Chem. Lett.* **2019**, *10* (21), 6727–6733.

(11) Van Goethem, E. M.; Pinion, C. W.; Cating, E. E. M.; Cahoon, J. F.; Papanikolas, J. M. Observation of Phonon Propagation in Germanium Nanowires Using Femtosecond Pump–Probe Microscopy. *ACS Photonics* **2019**, 1–10.

(12) Rozenman, G. G.; Akulov, K.; Golombek, A.; Schwartz, T. Long-Range Transport of Organic Exciton-Polaritons Revealed by Ultrafast Microscopy. *ACS Photonics* **2017**, *5* (1), 105–110.
(13) Sung, J.; Schnedermann, C.; Ni, L.; Sadhanala, A.; Chen, R. Y. S.; Cho, C.; Priest, L.; Lim, J. M.; Kim, H.-K.; Monserrat, B.; et al. Long-Range Ballistic Propagation of Carriers in Methylammonium Lead Iodide Perovskite Thin Films. *Nature Phys* **2020**, *16*, 171–176.
(14) Guo, Z.; Wan, Y.; Yang, M.; Snaider, J.; Zhu, K.; Huang, L. Long-Range Hot-Carrier Transport in Hybrid Perovskites Visualized by Ultrafast Microscopy. *Rev. Sci. Instrum.* **2017**, *356* (6333), 59.
(15) Simpson, M. J.; Doughty, B.; Yang, B.; Xiao, K.; Ma, Y.-Z. Imaging Electronic Trap States in Perovskite Thin Films with Combined Fluorescence and Femtosecond Transient Absorption Microscopy. *J. Phys. Chem. Lett.* **2016**, *7* (9), 1725–1731.
(16) Guo, Z.; Manser, J. S.; Wan, Y.; Kamat, P. V.; Huang, L. Spatial and Temporal Imaging of Long-Range Charge Transport in Perovskite Thin Films by Ultrafast Microscopy. *Nat. Commun.* **2015**, *6* (1), 1–8.
(17) Grancini, G.; Polli, D.; Fazzi, D.; Cabanillas-Gonzalez, J.; Cerullo, G.; Lanzani, G. Transient Absorption Imaging of P3HT:PCBM Photovoltaic Blend: Evidence for Interfacial Charge Transfer State. *J. Phys. Chem. Lett.* **2011**, *2* (9), 1099–1105.
(18) Wong, C. T. O.; Lo, S. S.; Huang, L. Ultrafast Spatial Imaging of Charge Dynamics in Heterogeneous Polymer Blends. *J. Phys. Chem. Lett.* **2012**, *3* (7), 879–884.
(19) Nah, S.; Spokoyny, B. M.; Soe, C. M. M.; Stoumpos, C. C.; Kanatzidis, M. G.; Harel, E. Ultrafast Imaging of Carrier Cooling in Metal Halide Perovskite Thin Films. *Nano Lett.* **2018**, *18* (2), 1044–1048.
(20) Hecht, E. *Optics*, 4 ed.; Pearson Education: Addison-Wesley, 2002.
(21) Fischer, M. C.; Wilson, J. W.; Robles, F. E.; Warren, W. S. Invited Review Article: Pump-Probe Microscopy. *Rev. Sci. Instrum.* **2016**, *87* (3), 031101.
(22) Benninger, R. K. P.; Piston, D. W. Two-Photon Excitation Microscopy for the Study of Living Cells and Tissues. *Current Protocols in Cell Biology* **2013**, *59* (1), 4.11.1–4.11.24.
(23) Davydova, D.; Cadena, A.; Akimov, D. Transient Absorption Microscopy: Advances in Chemical Imaging of Photoinduced Dynamics. *Laser Photonics Rev.* **2016**.
(24) Grumstrup, E. M.; Gabriel, M. M.; Cating, E. E. M.; Van Goethem, E. M.; Papanikolas, J. M. Pump-Probe Microscopy: Visualization and Spectroscopy of Ultrafast Dynamics at the Nanoscale. *CHEMICAL PHYSICS* **2015**, *458* (C), 30–40.
(25) Virgili, T.; Grancini, G.; Molotokaite, E.; Suarez-Lopez, I.; Rajendran, S. K.; Liscio, A.; Palermo, V.; Lanzani, G.; Polli, D.; Cerullo, G. Confocal Ultrafast Pump–Probe Spectroscopy: a New Technique to Explore Nanoscale Composites. *Nanoscale* **2012**, *4* (7), 2219–8.
(26) Devadas, M. S.; Devkota, T.; Johns, P.; Li, Z.; Lo, S. S.; Yu, K.; Huang, L.; Hartland, G. V. Imaging Nano-Objects by Linear and Nonlinear Optical Absorption Microscopies. *Nanotechnology* **2015**, *26* (35), 354001–354016.
(27) Dong, P.-T.; Cheng, J.-X. Pump–Probe Microscopy: Theory, Instrumentation, and Applications. *Spectroscopy* **2017**.

(28) Knowles, K. E.; Koch, M. D.; Shelton, J. L. Three Applications of Ultrafast Transient Absorption Spectroscopy of Semiconductor Thin Films: Spectroelectrochemistry, Microscopy, and Identification of Thermal Contributions. *J. Mater. Chem. C,* **2018**, *6* (44), 11853–11867.
(29) Zhu, T.; Snaider, J. M.; Yuan, L.; Huang, L. Ultrafast Dynamic Microscopy of Carrier and Exciton Transport. *Annu. Rev. Phys. Chem.* **2019**, *70* (1), 219–244.
(30) Ostrander, J. S.; Serrano, A. L.; Ghosh, A.; Zanni, M. T. Spatially Resolved Two-Dimensional Infrared Spectroscopy via Wide-Field Microscopy. *ACS Photonics* **2016**, *3* (7), 1315–1323.
(31) Baiz, C. R.; Schach, D.; Tokmakoff, A. Ultrafast 2D IR Microscopy. *Opt. Express* **2014**, *22* (15), 18724–18735.
(32) Jones, A. C.; Kearns, N. M.; Ho, J.-J.; Flach, J. T.; Zanni, M. T. Impact of Non-Equilibrium Molecular Packings on Singlet Fission in Microcrystals Observed Using 2D White-Light Microscopy. *Nature Chemistry* **2019**, 1–8.
(33) Tiwari, V.; Matutes, Y. A.; Gardiner, A. T.; Jansen, T. L. C.; Cogdell, R. J.; Ogilvie, J. P. Spatially-Resolved Fluorescence-Detected Two-Dimensional Electronic Spectroscopy Probes Varying Excitonic Structure in Photosynthetic Bacteria. *Nat. Commun.* **2018**, *9* (1), 4219–4226.
(34) Piatkowski, L.; Accanto, N.; Calbris, G.; Christodoulou, S.; Moreels, I.; van Hulst, N. F. Ultrafast Stimulated Emission Microscopy of Single Nanocrystals. *Science* **2019**, *366* (6470), 1240–1243.
(35) Penwell, S. B.; Ginsberg, L. D. S.; Noriega, R.; Ginsberg, N. S. Resolving Ultrafast Exciton Migration in Organic Solids at the Nanoscale. *Nature Materials* **2017**, *16* (11), 1136–1141.
(36) Imura, K.; Nagahara, T.; Okamoto, H. Imaging of Surface Plasmon and Ultrafast Dynamics in Gold Nanorods by Near-Field Microscopy. *J. Phys. Chem. B* **2004**, *108* (42), 16344–16347.
(37) Eisele, M.; Cocker, T. L.; Huber, M. A.; Plankl, M.; Viti, L.; Ercolani, D.; Sorba, L.; Vitiello, M. S.; Huber, R. Ultrafast Multi-Terahertz Nano-Spectroscopy with Sub-Cycle Temporal Resolution. *Nat. Photonics* **2014**, *8* (11), 841–845.
(38) Berera, R.; van Grondelle, R.; Kennis, J. T. M. Ultrafast Transient Absorption Spectroscopy: Principles and Application to Photosynthetic Systems. *Photosynth Res* **2009**, *101* (2), 105–118.
(39) Schnedermann, C.; Lim, J. M.; Wende, T.; Duarte, A. S.; Ni, L.; Gu, Q.; Sadhanala, A.; Rao, A.; Kukura, P. Sub-10 Fs Time-Resolved Vibronic Optical Microscopy. *J. Phys. Chem. Lett.* **2016**, *7*, 4854–4859.
(40) Devkota, T.; Beane, G.; Yu, K.; Hartland, G. V. Attenuation of Acoustic Waves in Ultrafast Microscopy Experiments. *J. Appl. Phys.* **2019**, *125* (16), 163102–163107.
(41) Fu, D.; Matthews, T. E.; Ye, T.; Piletic, I. R.; Warren, W. S. Label-Free in Vivo Optical Imaging of Microvasculature and Oxygenation Level. *J. Biomed. Opt.* **2008**, *13* (4), 040503–040503.
(42) Simpson, M. J.; Doughty, B.; Yang, B.; Xiao, K.; Ma, Y.-Z. Spatial Localization of Excitons and Charge Carriers in Hybrid Perovskite Thin Films. *J. Phys. Chem. Lett.* **2015**, *6* (15), 3041–3047.
(43) Wong, C. Y.; Penwell, S. B.; Cotts, B. L.; Noriega, R.; Wu, H.; Ginsberg, N. S. Revealing Exciton Dynamics in a Small-Molecule Organic Semiconducting Film with Subdomain Transient Absorption Microscopy. *J. Phys. Chem. C* **2013**, *117* (42), 22111–22122.

(44) Papernov, S.; Schmid, A. W. Correlations Between Embedded Single Gold Nanoparticles in SiO2 Thin Film and Nanoscale Crater Formation Induced by Pulsed-Laser Radiation. *J. Appl. Phys.* **2002**, *92* (10), 5720–5728.
(45) Masters, B. R.; So, P. T. C.; Buehler, C.; Barry, N. P.; Sutin, J. D. B.; Mantulin, W. W.; Gratton, E. Mitigating Thermal Mechanical Damage Potential During Two-Photon Dermal Imaging. *J. Biomed. Opt.* **2004**, *9* (6), 1265–1270.
(46) Gallais, L.; Douti, D. B.; Commandré, M.; Batavičiūtė, G.; Pupka, E.; Ščiuka, M.; Smalakys, L.; Sirutkaitis, V.; Melninkaitis, A. Wavelength Dependence of Femtosecond Laser-Induced Damage Threshold of Optical Materials. *J. Appl. Phys.* **2015**, *117* (22), 223103–223115.
(47) Chen, J. K.; Tzou, D. Y.; Beraun, J. E. Numerical Investigation of Ultrashort Laser Damage in Semiconductors. *International Journal of Heat and Mass Transfer* **2005**, *48* (3-4), 501–509.
(48) Shi, H.; Yan, R.; Bertolazzi, S.; Brivio, J.; Gao, B.; Kis, A.; Jena, D.; Xing, H. G.; Huang, L. Exciton Dynamics in Suspended Monolayer and Few-Layer MoS 22D Crystals. *ACS Nano* **2013**, *7* (2), 1072–1080.
(49) Gabriel, M. M.; Kirschbrown, J. R.; Christesen, J. D.; Pinion, C. W.; Zigler, D. F.; Grumstrup, E. M.; Mehl, B. P.; Cating, E. E. M.; Cahoon, J. F.; Papanikolas, J. M. Direct Imaging of Free Carrier and Trap Carrier Motion in Silicon Nanowires by Spatially-Separated Femtosecond Pump–Probe Microscopy. *Nano Lett.* **2013**, *13* (3), 1336–1340.
(50) Zhang, G.; Zhao, J.; Chow, P. C. Y.; Jiang, K.; Zhang, J.; Zhu, Z.; Zhang, J.; Huang, F.; Yan, H. Nonfullerene Acceptor Molecules for Bulk Heterojunction Organic Solar Cells. *Chem. Rev.* **2018**, *118* (7), 3447–3507.
(51) Kaake, L. G.; Welch, G. C.; Moses, D.; Bazan, G. C.; Heeger, A. J. Influence of Processing Additives on Charge-Transfer Time Scales and Sound Velocity in Organic Bulk Heterojunction Films. *J. Phys. Chem. Lett.* **2012**, *3* (10), 1253–1257.
(52) Jo, J.; Kim, S.-S.; Na, S.-I.; Yu, B.-K.; Kim, D.-Y. Time-Dependent Morphology Evolution by Annealing Processes on Polymer:Fullerene Blend Solar Cells. *Adv. Funct. Mater.* **2009**, *19* (6), 866–874.
(53) Huang, Y.; Kramer, E. J.; Heeger, A. J.; Bazan, G. C. Bulk Heterojunction Solar Cells: Morphology and Performance Relationships. *Chem. Rev.* **2014**, *114* (14), 7006–7043.
(54) Hoppe, H.; Niggemann, M.; Winder, C.; Kraut, J.; Hiesgen, R.; Hinsch, A.; Meissner, D.; Sariciftci, N. S. Nanoscale Morphology of Conjugated Polymer/Fullerene-Based Bulk- Heterojunction Solar Cells. *Adv. Funct. Mater.* **2004**, *14* (10), 1005–1011.
(55) Serbenta, A.; Kozlov, O. V.; Portale, G.; van Loosdrecht, P. H. M.; Pshenichnikov, M. S. Bulk Heterojunction Morphology of Polymer:Fullerene Blends Revealed by Ultrafast Spectroscopy. *Sci. Rep.* **2016**, *6* (1), 1–11.
(56) Clarke, T. M.; Durrant, J. R. Charge Photogeneration in Organic Solar Cells. *Chem. Rev.* **2010**, *110* (11), 6736–6767.
(57) Köhler, A.; Bässler, H. *Electronic Processes in Organic Semiconductors: an Introduction*; Wiley-VCH, 2015.
(58) Caruso, D.; Troisi, A. Long-Range Exciton Dissociation in Organic Solar Cells. *Proc Natl Acad Sci USA* **2012**, *109* (34), 13498–5.
(59) Bian, Q.; Ma, F.; Chen, S.; Wei, Q.; Su, X.; Buyanova, I. A.; Chen, W. M.; Ponseca, C. S.; Linares, M.; Karki, K. J.; et al. Vibronic Coherence Contributes

to Photocurrent Generation in Organic Semiconductor Heterojunction Diodes. *Nat. Commun.* **2020**, 1–9.

(60) Drummy, L. F.; Davis, R. J.; Moore, D. L.; Durstock, M.; Vaia, R. A.; Hsu, J. W. P. Molecular-Scale and Nanoscale Morphology of P3HT:PCBM Bulk Heterojunctions: Energy-Filtered TEM and Low-Dose HREM. *Chem. Mater.* **2011**, *23* (3), 907–912.

(61) Huang, W.; Gann, E.; Chandrasekaran, N.; Thomsen, L.; Prasad, S. K. K.; Hodgkiss, J. M.; Kabra, D.; Cheng, Y.-B.; McNeill, C. R. Isolating and Quantifying the Impact of Domain Purity on the Performance of Bulk Heterojunction Solar Cells. *Energy Environ. Sci.* **2017**, *10* (8), 1843–1853.

(62) Lou, S. J.; Zhou, N.; Guo, X.; Chang, R. P. H.; Marks, T. J.; Chen, L. X. Effects of 1,8-Diiodooctane on Domain Nanostructure and Charge Separation Dynamics in PC 71BM-Based Bulk Heterojunction Solar Cells. *J. Mater. Chem. A* **2018**, *6* (46), 23805–23818.

(63) Bartelt, J. A.; Beiley, Z. M.; Hoke, E. T.; Mateker, W. R.; Douglas, J. D.; Collins, B. A.; Tumbleston, J. R.; Graham, K. R.; Amassian, A.; Ade, H.; et al. The Importance of Fullerene Percolation in the Mixed Regions of Polymer-Fullerene Bulk Heterojunction Solar Cells. *Adv. Energy Mater.* **2012**, *3* (3), 364–374.

(64) Hedley, G. J.; Ward, A. J.; Alekseev, A.; Howells, C. T.; Martins, E. R.; Serrano, L. A.; Cooke, G.; Ruseckas, A.; Samuel, I. D. W. Determining the Optimum Morphology in High-Performance Polymer-Fullerene Organic Photovoltaic Cells. **2019**, 1–10.

(65) Polli, D.; Grancini, G.; Clark, J.; Celebrano, M.; Virgili, T.; Cerullo, G.; Lanzani, G. Nanoscale Imaging of the Interface Dynamics in Polymer Blends by Femtosecond Pump-Probe Confocal Microscopy. *Adv. Mater.* **2010**, *22* (28), 3048–3051.

(66) Zarrabi, N.; Burn, P. L.; Meredith, P.; Shaw, P. E. Acceptor and Excitation Density Dependence of the Ultrafast Polaron Absorption Signal in Donor–Acceptor Organic Solar Cell Blends. *J. Phys. Chem. Lett.* **2016**, *7* (14), 2640–2646.

(67) Stolterfoht, M.; Armin, A.; Shoaee, S.; Kassal, I.; Burn, P.; Meredith, P. Slower Carriers Limit Charge Generation in Organic Semiconductor Light-Harvesting Systems. *Nat. Commun.* **2016**, *7*, 1–7.

(68) Moritomo, Y.; Yonezawa, K.; Yasuda, T. Carrier Density Effect on Recombination in PTB7-Based Solar Cell. *Sci. Rep.* **2015**, 1–8.

(69) Yonezawa, K.; Kamioka, H.; Yasuda, T.; Han, L.; Moritomo, Y. Exciton-to-Carrier Conversion Processes in a Low-Band-Gap Organic Photovoltaic. *Jpn. J. Appl. Phys.* **2013**, *52* (6R), 062405–062409.

(70) Penwell, S. B.; Ginsberg, L. D. S.; Ginsberg, N. S. Bringing Far-Field Subdiffraction Optical Imaging to Electronically Coupled Optoelectronic Molecular Materials Using Their Endogenous Chromophores. *J. Phys. Chem. Lett.* **2015**, *6* (14), 2767–2772.

Chapter 5. Conclusions

The work presented in this thesis demonstrates the value of femtosecond spectroscopy to elucidate the ultrafast processes that occur in photoactive nanomaterials and give rise to their functional properties. Further, I detailed my development and design of a transient absorption microscope and multiple characterisation tests performed on the system.

In chapter 2, ultrafast transient absorption was used to investigate the dynamics of localised surface plasmon polaritons on hollow gold nanoshells (HGNs) coupled with excitons in J-aggregates. I investigated HGNs samples with J-aggregates on the outer surface, on the inside of the nanoparticle, and both inside and outside. As far as I am aware, this study is the first to investigate the transient response of HGNs with J-aggregates inside hollow gold nanoparticles. For the sample with J-aggregates on the outer surface and on both the inner and outer surfaces, the effect of coupling was apparent in the line shapes of the transient data at all delay times. The splitting of the LSPR observed by addition of J-aggregates to only the inner surface of the HGN was generally weaker in both linear and non-linear measurements, which may be due to the optically active HGN LSPR mode being more strongly associated with the outer surface of the HGN.

By comparing the responses of coupled and uncoupled HGNs I was able to determine that in all the samples the plasmon dephases very quickly (prior studies indicate ~10 fs) and creates a hot electron population that thermalises within the first ~0.5 ps. The decay in the kinetics after this time were caused by the cooling of the hot electron population and were largely consistent between all the coupled and uncoupled systems investigated, with differences in the phonon-phonon coupling rate potentially attributable to the J-aggregates coating the surface of the HGN acting as an insulating layer. Further studies on more strongly coupled HGNs with J-aggregates only on the inside may help explore this possibility.

Future work could include computational modelling and 2DES measurements to aid in disentangling the various overlapping and shifting spectral features, as well as repeating the TA measurements of samples of HGN with J-aggregates only contained within the hollow cavity, to further investigate the effects of positioning the J-aggregates inside, rather than on the surface of the HGNs. Finally, performing similar measurements to these on a range of HGN samples with a variety of sizes and shell thicknesses would

allow the effects of detuning the LSPR resonance and, potentially, a variety of coupling strengths to be systematically investigated and provide fundamental insights.

Chapter 3 detailed my TRIR and 2DIR investigations of formamidinium lead iodide perovskite thin films. Theoretical studies have suggested that for this, and other, hybrid lead iodide perovskites, the rotation of the organic cation within the lead iodide lattice could play a pivotal role in explaining the anomalously high power conversion efficiencies of the photoactive material. This mechanism occurs via the formation of ferroelectric domains which aids in channelling charge carriers to electrodes, thereby reducing loses due to charge recombination. However, my analysis of the 2DIR data found the rotational re-orientation of the formamidinium cations was very fast, and therefore unable to support the theorised stable ferroelectric domains. The cation was found to reorient on two timescales, with associated 470 ± 50 fs and 2.8 ± 0.5 ps time constants.

Comparison of the data with molecular dynamics simulations revealed dynamical motions associated with the two different time constants: motions associated with the hundreds of femtosecond time component include: FA^+ agitation about an equilibrium position, with the NH_2 functional groups oriented towards opposite faces of the inorganic lattice cube. Whereas the picosecond component is associated with the cation undergoing 90° flips between adjacent cube faces. These 2DIR results provided the first direct measurement of FA^+ rotation inside thin perovskite films and preclude the possibility of the theorised long-lived (anti)ferroelectric domains.

TRIR measurements of the formamidinium perovskite showed a prominent vibrational transient feature, with an oscillator strength commensurate to electronic intra-band transitions. Photogenerated charge carriers increase the internal electric field of perovskite thin films, perturbing the FA^+ antisymmetric stretching vibrational potential so dramatically that the associated oscillator strength increased by orders of magnitude. This observation is indicative of large polaron formation and may be the reason for the anomalously high PCE of formamidinium lead iodide perovskite thin films.

In future work transient 2DIR measurements could help to elucidate whether large polaron formation plays a significant role in charge carrier extraction. Such measurements could monitor the effect of electrons in the conduction band on the re-orientation dynamics of FA^+ cations in the inorganic lattice and therefore interrogate whether the large polaron is formed. However, practically these experiments would be extremely challenging due to heating effects.

In chapter 4, the third and final experimental chapter of this thesis, efforts to build a transient absorption microscope were detailed. It was planned that the set-up would be used to measure the response of a PTB7:$PC_{70}BM$ bulk heterojunction film. Bulk heterojunction films contain intermixed micro- or nano-scale domains of acceptor and donor materials. The morphology of these domains has been shown to be vital to the efficiency of these films as photovoltaic materials. Therefore, ultrafast TAM provides an ideal experimental tool to investigate the charge carrier dynamics occurring in the morphology of these materials.

The TAM design detailed in this thesis is similar to other reported MHz TAM experiments, with the significant exception that a curved silver mirror was used to focus the pump and probe beams into the sample, which has only been reported for widefield kHz TAM set-ups previously. Therefore, this design relied on the aperture of the collection objective lens (and an optional second pinhole) to remove scattered and out of focus light. The sensitivity of the experiment was found to be sufficient for bulk measurements but ultimately it was found that the experiment required high powers to give detectable signal for non-linear microscopy measurements. The high power density at the sample resulted in thermal damage to all the samples tested. I concluded that the set-up is unusable in its current configuration. Therefore, the best approach for future work would be to incorporate a microscope objective to focus the incoming light into the sample, making the experimental design consistent with published literature. This would yield a smaller focal spot size and so reduce the total power needed to achieve the same power density at the sample. With less total power applied to the sample, thermal damage is expected to be reduced. Moreover, there would be less scattered signal emanating from locations outside the collection volume, thereby reducing the noise in measurements.

To summarise, in my thesis I have demonstrated the application of ultrafast time-resolved spectroscopy techniques to photoactive nanomaterials. Ultrafast time-resolved spectroscopies are a diverse and adaptable range of techniques and, as such, it is no surprise that they prove a useful tool to investigate nanomaterials. With the growing range of photoactive nanomaterials being developed and the advancement of ultrafast spectroscopy techniques, there is no doubt that such experiments will continue to provide key insights into the function of these promising materials.